DEPARTMENT OF PHYSICS

NOVA SCHOOL OF SCIENCE & TECHNOLOGY

MARIA INÊS DA GRAÇA JORGE DA SILVA RIBEIRO

Bachelor in Biomedical Engineering

COMPARISON OF TWO ^{90}Y-CHARGED GLASS MICROSPHERES LIVER RADIOEMBOLIZATION DOSIMETRY METHODS: S-VALUES AND MONTE CARLO - GATE

MASTER IN BIOMEDICAL ENGINEERING

NOVA University Lisbon
November, 2021

NOVA SCHOOL OF SCIENCE & TECHNOLOGY

DEPARTMENT OF PHYSICS

COMPARISON OF TWO ^{90}Y-CHARGED GLASS MICROSPHERES LIVER RADIOEMBOLIZATION DOSIMETRY METHODS: S-VALUES AND MONTE CARLO - GATE

MARIA INÊS DA GRAÇA JORGE DA SILVA RIBEIRO

Bachelor in Biomedical Engineering

Advisers: Doctor Paulo Ferreira
Medical Physics Expert and Researcher, Nuclear Medicine - Radiopharmacology Department - Champalimaud Centre for the Unknown - Champalimaud Foundation
Doctor João Cruz
Associate Professor, NOVA School of Science and Technology

Examination Committee:

Chair: Doctor Carla Maria Quintão Pereira
Assistant Professor, NOVA School of Science and Technology

Rapporteur: Doctor Luís Filipe dos Santos Garcia Peralta
Associate Professor, Faculty of Sciences of the University of Lisbon

Adviser: Doctor Paulo Miguel dos Santos Ferreira
Medical Physics Expert and Researcher, Nuclear Medicine - Radiopharmacology Department - Champalimaud Centre for the Unknown - Champalimaud Foundation

MASTER IN BIOMEDICAL ENGINEERING

NOVA University Lisbon
November, 2021

Comparison of Two ^{90}Y-charged Glass Microspheres Liver Radioembolization Dosimetry Methods: S-values and Monte Carlo - GATE

To House RiverRun

Acknowledgements

I would like to express my gratitude to my supervisors, Professor Paulo Ferreira and Professor João Cruz, for their invaluable guidance. Their immense knowledge has sparked my curiosity daily throughout this work.

My gratitude extends to Professor Durval Costa, who gave me the opportunity to do this research at Champalimaud Center for the Unknow - Champalimaud Foundation and encouraged me to learn more about Nuclear Medicine. To Professor Francisco Oliveira, who gave me great insights on how to improve this work. To the staff at the Nuclear Medicine - Radiopharmacology Department who welcomed me during my tours and helped me in acquiring the phantom images. To the GATE open-source community who replied to my many questions on their forum.

I am deeply grateful to my family for their encouragement and support through my studies. To my mom and dad, Florbela and Eduardo, for tolerating my high demand for a low decibel household during the lockdown. To my brother, Eduardo, for motivating me to increase my VO2max before finishing my master degree.

Lastly, I am extremely grateful to my boyfriend, João Santos, for riding along with this roller coaster.

Abstract

Radioembolization with ^{90}Y glass microspheres internally irradiates and treats unresectable liver tumors. Personalized dosimetry is legally required to prescribe the optimum activity of ^{90}Y and ensure treatment quality. However, current clinical practice does not consider patient-specific variables, possibly limiting patients' overall survival.

Voxel S-values dosimetry can achieve clinical dosimetry but does not consider tissue heterogeneity. GATE performs Monte Carlo dosimetry based on medical images, addressing tissue heterogeneity. This work aims to assess the accuracy of voxel S-values dosimetry and evaluate the relevance and feasibility of Monte Carlo dosimetry to increase patients' overall survival. Absorbed dose distributions were computed using both dosimetry methods for treatment planning and verification of six retrospective treatments. Then, distributions were compared on the voxelwise and global levels of the volumes of interest, including the tumor and normal liver tissues and at the liver interface.

Monte Carlo dosimetry took 9 to 47 hours, while voxel S-values dosimetry took only a few seconds. Within the homogeneous tumor and normal liver volumes, excellent agreement between the two methods was reached for all dosimetry measures, and planning quality was equivalent. At the heterogeneous outer liver interface, a relative difference of -16% was found for the mean absorbed dose because voxel S-values dosimetry assumes that the lung tissue is equivalent to the liver tissue.

Results showed that voxel S-values dosimetry is accurate within the liver tissues but underestimates absorbed dose at the liver interface. Monte Carlo dosimetry is feasible in clinical practice and is relevant to understanding toxicity in lungs and other organs-at-risk. Therefore, it should be considered to optimize radioembolization in clinical practice and increase patients' overall survival.

Keywords: Radioembolization, Dosimetry, Voxel S-values, Monte Carlo, GATE.

Resumo

A radioembolização com microesferas de vidro carregadas com ^{90}Y irradia internamente e trata tumores hepáticos irressecáveis. A dosimetria personalizada é obrigatória por lei para prescrever a atividade ideal de ^{90}Y e garantir a qualidade do tratamento. No entanto, a prática clínica atual não considera as variáveis específicas de cada paciente, possivelmente limitando a sobrevida global.

A dosimetria por valores-S pode ser útil na prática clínica, mas não considera a heterogeneidade dos tecidos. O GATE realiza dosimetria por Monte Carlo baseada em imagens médicas, considerando a heterogeneidade dos tecidos. Esta dissertação visa avaliar a precisão da dosimetria por valores-S e a relevância e viabilidade da dosimetria por Monte Carlo para aumentar a sobrevida global. Foram calculadas distribuições de dose absorvida pelos dois métodos para o planeamento e verificação de seis tratamentos retrospetivos. Depois, as distribuições foram comparadas aos níveis global e do voxel nos volumes de interesse, incluindo os tecidos hepáticos tumoral e normal e a interface do fígado.

A dosimetria por Monte Carlo demorou entre 9 e 47 horas e por valores-S demorou apenas alguns segundos. Nos tecidos homogéneos hepáticos tumoral e normal, a concordância entre os dois métodos foi excelente para todas as medidas de dosimetria e a qualidade do planeamento foi equivalente. Na interface externa heterogénea do fígado, foi encontrada uma diferença relativa de -16% na dose absorvida média porque a dosimetria por valores-S assume que o tecido pulmonar é equivalente ao tecido hepático.

Os resultados mostram que a dosimetria por valores-S é precisa nos tecidos hepáticos, mas subestima a dose absorvida na interface fígado. A dosimetria por Monte Carlo é viável na prática clínica e é relevante para investigar a toxicidade nos pulmões e noutros órgãos em risco. Por isso, deve ser considerada para otimizar a radioembolização na prática clínica e potenciar a sobrevida global.

Palavras-chave: Radioembolização, Dosimetria, Valores S, Monte Carlo, GATE

Contents

List of Figures

List of Tables

Acronyms

ADD	Absorbed dose distribution
BAP	Bland-Altman plot
BED	Biological effective dose
CCA	Cholangiocarcinoma
CCU-CF	Champalimaud Centre for the Unknown - Champalimaud Foundation
cDVH	Cumulative dose-volume histogram
CS	Compton scattering
CT	Computed tomography
dDVH	Differential dose-volume histogram
DUH	Dose uncertainty histogram
DVH	Dose-volume histogram
EANM	European Association of Nuclear Medicine
EASL	European association for the study of the liver
EBRT	External beam radiation therapy
ED	Energy distribution
EGS	Electron gamma shower
EUBED	Equivalent uniform biological effective dose
EURATOM	European Atomic Energy Community
FBP	Filtered backpropagation
FLUKA	Fluktuierende kaskade
FM	Fiducial marker
FOV	Field-of-view
FWHM	Full width at half maximum
GAMOS	Geant4-based architecture for medicine-oriented simulations
GATE	Geant4 application for tomographic emission
GPS	General particle source

HCC	Hepatocellular carcinoma
HU	Hounsfield unit
IAEA	International atomic energy agency
ICC	Interclass correlation coefficient
ICRP	International commission on radiological protection
LDPE	Low-density polyethylene
LET	Linear energy transfer
LOR	Lines of response
LQ	Linear quadratic
MAA	Macroagreggated albumin
MC	Monte Carlo
MCNP	Monte carlo n-particle
MIRD	Medical internal radiation dose
MLEM	Maximum likelihood expection maximization
MS	Microsphere
NLV	Normal liver volume
NM	Nuclear Medicine
NTCP	Normal tissue complications probability
OSEM	Ordered-subsets expectation-maximization
PCC	Pearson correlation coefficient
PDF	Probability distribution function
PEE	Photoelectric effect
PENELOPE	Penetration and energy loss of positrons and electrons
PET	Positron emission tomography
PM	Pancreatic metastases
PMP	Polymethylpentene
PP	Pair production
PTV	Planning tumor volume
RE	Radioembolization
RP	Radiopharmaceutical
RPT	Radiopharmaceutical therapy
RS	Rayleigh scattering

RT	Representative tissue
RWLV	Reference whole liver volume
SPECT	Single photon emission computed tomography
TACE	Transarterial chemoembolization
TCP	Tumor control probability
TLV	Target liver volume
TOF	Time-of-flight
TOPAS	Tool for particle simulation
TS	Tissue substitute
UVH	Uncertainty volume histogram
VOI	Volume of interest
VSV	Voxel S-values
WLV	Whole liver volume

Symbols

A	Activity
AA	Administrated activity
A_{i}	Atomic weight of a chemical element i in a medium
α	Radiosensitivity to single hit events
$\overline{RD}$	Absolute relative difference
β^-	Beta-minus
β	Radiosensitivity to multiple hit events
Bq	Becquerel
σ_{T}	Total cross-section
D	Absorbed dose
$\Delta D(v,p)$	Absorbed dose difference between voxels v and p in verification and planning absorbed dose distributions
D_{k}	Absorbed dose in voxel k
$d_{\mathrm{k,i}}$	Absorbed dose in voxel k by an primary particle i
$\overline{D}_{\mathrm{lungs}}$	Mean absorbed dose within the lungs
$\overline{D}$	Mean absorbed dose
$\overline{D}_{\mathrm{NLV}}$	Mean absorbed dose within the normal liver volume
$\overline{D}_{\mathrm{PTV}}$	Mean absorbed dose within the planning tumor volume
$\overline{D}_{\mathrm{TLV}}$	Mean absorbed dose within the target liver volume
E	Energy
E_{k}	Deposited energy in voxel k
$e_{\mathrm{k,i}}$	Deposited energy in voxel k by an primary particle i
$\overline{E}$	Mean energy imparted to tissues by ionizing radiation
FU_{NLV}	Fractional uptake of activity in the normal liver tissues
FU_{PTV}	Fractional uptake of activity in the planning tumor volume
$\gamma(v)$	Selected gamma-index for voxel v

$\Gamma(v,p)$	Map of gamma-index candidates for voxel v
γ	Gamma
I	Beam intensity
I_0	Initial beam intensity
k_1	Parameter for a CT scanner response to tissue parameters
k_2	Parameter for a CT scanner response to tissue parameters
κ	Linear attenuation coefficient of pair production
λ	Decay constant
λ_t	Time integral factor for yttrium-90 activity calibration
m	Mass
m_{TLV}	Mass of target liver volume
μ	Total linear attenuation coefficient
μ/ρ	Total mass attenuation coefficient
$\overline{\mu}$	Linear attenuation coefficient of the local tissue
N	Number of atoms per unit volume
N_0	Initial amount of parent nuclide
N_A	Avogadro's constant
NaI(Tl)	Sodium iodine doped with thallium
N_f	Number of fractions in EBRT
N_V	Number of voxels in a volume of interest
R	Radioactive residual waste
$\Delta r(v,p)$	Euclidean distance between voxels v and p in verification and planning absorbed dose distributions
R^2	Coefficient of determination
RD	Relative difference
ρ	Mass density
S	Stopping-power
S/ρ	Mass stopping-power
S_{col}	Collision stopping-power
SF	Survival fraction
σ	Linear attenuation coefficient of compton scatter
σ_i^T	Total cross-section of a chemical element i in a medium
S_{rad}	Radiation stopping-power

SU	Relative statistic uncertainty
$\overline{SU}$	Mean relative statistic uncertainty
t	Time
$t_{1/2}$	Half-life
τ	Linear attenuation coefficient of photoelectric effect
^{99}Tc	Technetium-99
^{99m}Tc	Technetium-99 metastable
T_{phys}	Half-life for yttrium-90 decay
T_{rep}	Half-life for cell repair
w_{i}	Weight of a chemical element i in a medium
x	Medium thickness
^{90}Y	Yttrium-90
Z	Atomic number
^{90}Zr	Zirconium-90

Chapter 1

Introduction

1.1 Context and Motivation

Primary liver cancer was the sixth most commonly diagnosed cancer and the third leading cause of cancer death worldwide in 2020 [1]. Liver cancer yields a high mortality rate because only around 10 to 20% of diagnosed patients are eligible for curative surgeries [2]. For unresectable liver tumors, radioembolization (RE) is emerging as an innovative, effective, and safe therapy in Nuclear Medicine (NM) scope. The need for personalized dosimetry to optimize RE delivery - and ultimately improve patients' overall survival - motivated the research presented in this work.

RE combines internal irradiation and distal embolization in liver tumors by administrating microspheres (MS) charged with Yttrium-90 (^{90}Y) into the hepatic artery [3]. The key advantage of RE is that a preferential arterial flow gears most MSs into tumor tissues, sparing normal tissues from ^{90}Y radiation [2]. Nevertheless, radiation-induced complications in normal tissues must be avoided to ensure treatment safety. RE optimization aims to adjust the administrated activity, AA, of ^{90}Y – MS to a specific patient that maximizes tumor control over the relative toxic side-effects, i.e., the therapeutic index.

Personalized dosimetry is paramount in RE optimization. Dosimetry quantifies the absorbed dose, D, defined as the amount of deposited energy by radiation particles in tissues per unit mass. RE optimization seeks to achieve the highest possible absorbed dose within the planning tumor volume (PTV) while ensuring a tolerable absorbed dose within the surrounding normal tissues, especially within the normal liver volume (NLV).

Regarding optimization of all radiation therapies, the European Atomic Energy Community (EURATOM) directive 2013/59/EURATOM of 5 December 2013 [4] states that: *"exposures of target volumes shall be individually planned and their delivery appropriately verified taking into account that doses to non-target volumes and tissues shall be as low as reasonably achievable and consistent with the intended radiotherapeutic purpose of the exposure."*.[1] Later in response, the European Association of Nuclear Medicine (EANM) communicated new guidelines for RE. First, the activity of ^{90}Y – MS should be prescribed based

[1] In 2018, Portugal transposed this EURATOM directive into national law [5].

on personalized dosimetry calculations within the NLV and PTV. Second, the biological response and toxicity of different tissues to ^{90}Y – MS radiation should be considered [6].

RE personalized dosimetry, in compliance with the directives mentioned above, should account for three key input variables: (1) the non-uniform activity distribution of ^{90}Y – MS, (2) tissues heterogeneity around ^{90}Y – MS, and (3) segmentation of volumes of interest (VOI), including NLV and PTV [2]. RE treatment planning aims to define the three dosimetry variables, starting with a hepatic angiography and administration of Technetium-99m labelled macroagreggated albumin (^{99m}Tc–MAA). Then, planar scintigraphy and single photon emission computed tomography (SPECT) images allow to evaluate liver-lung shunt and map ^{99m}Tc – MAA as a prediction of ^{90}Y – MS activity distribution. Finally, co-registration of computed tomography (CT) and SPECT images allows for segmenting VOIs and assessing tissue heterogeneity. Following RE treatment delivery with ^{90}Y – MS, positron emission tomography (PET) and CT images allow RE treatment verification.

Currently, RE dosimetry follows the guidelines of MS's manufacturer. Two types of ^{90}Y – MS are commercially available: glass and resin MSs. This work only refers to the former. Glass MS's manufacturer recommends mono-compartment dosimetry with an estimation of a patient-averaged absorbed dose within the whole perfused liver volume segmented in CT images, including tumor and normal tissues[2] [7]. Therefore, current clinical practice does not consider all patient-specific dosimetry variables and does not comply with the EURATOM directive and EANM guidelines, which possibly limits RE patients' overall survival.

A recent clinical trial conducted by glass MS's manufacturer proved that personalized dosimetry improves patients' overall survival (Δ = +16 months) by considering the multi-compartment ^{90}Y – MS distribution within the PTV and NLV [8]. However, multi-compartment dosimetry is not fully personalized because it does not consider the non-uniform activity distribution of ^{90}Y – MS within these VOIs, patient-specific tissue heterogeneity, and radiobiology.

Advanced clinics are investigating voxel-based dosimetry methods to achieve fully personalized dosimetry. Since 2016, voxel S-values (VSV) dosimetry has been investigated and employed in RE scope at Champalimaud Center for the Unknown - Champalimaud Foundation (CCU-CF). VSV dosimetry accounts for the non-uniform activity distribution of ^{90}Y – MS in tissues to calculate absorbed dose distributions (ADD) in a 3D matrix based on planning ^{99m}Tc – MAA SPECT images or verification ^{90}Y – MS PET images [9]. Voxelized ADDs allow balancing absorbed doses within the NLV and PTV and measuring radiobiology effects for RE optimization. However, VSV dosimetry still does not consider

[2]The perfused liver volume comprises the liver volume undergoing angiography. It can be either a lobe (left or right) or one or more segments.

patient-specific tissues heterogeneity, and, thus, ADDs obtained with VSV dosimetry (VSV-ADD) are only semi-personalized.

Monte Carlo (MC) dosimetry is considered the gold standard for personalized RE dosimetry because it accounts for the patient-specific tissue heterogeneity to compute ADDs [10]. Geant4 Application for Tomographic Emission (GATE) toolkit is an MC code capable of simulating ADDs based on medical images. First, GATE uses a CT image to build a geometry that mimics patient-specific tissue heterogeneity by converting CT numbers to tissue parameters: mass density and chemical composition. Then, GATE defines the non-uniform ^{90}Y activity distribution based on planning ^{99m}Tc – MAA SPECT or verification ^{90}Y – MS PET images. Finally, GATE scores an ADD by simulating the interaction of ^{90}Y radiation particles within the pre-defined geometry. The output ADDs obtained with MC-GATE dosimetry (MC-ADD) achieve the highest personalized dosimetry accuracy on a voxel scale and improve RE optimization.

A major drawback of MC dosimetry is the requirement of a high computational power or a long calculation time. The lack of computational power jeopardizes the feasibility of MC dosimetry in the clinical practice as the duration of each MC-ADD simulation might not fit in the clinical schedule. Hence, MC dosimetry should only be employed if it can improve RE optimization compared to VSV dosimetry.

Overall, the legal requirement for fully personalized dosimetry in RE motivated the NM-Radiopharmacology research group at CCU-CF to investigate MC dosimetry to optimize RE and increase patients' overall survival.

1.2 Research Goals and Approach

The main goals of this work are to (1) assess the *accuracy* of VSV dosimetry compared to gold standard MC dosimetry and (2) evaluate the *relevance* and *feasibility* of introducing MC dosimetry in clinical practice to optimize RE and increase patients' overall survival. Pairs of computed VSV- and MC-ADDs were computed and compared for this purpose.

The NM-Radiopharmacology group at CCU-CF retrospectively selected six RE patients from their database, and provided non-hybrid SPECT and CT planning images, hybrid PET/CT verification images, and VOIs segmentation. Then, VSV and MC dosimetry calculations were performed using GATE and *MATLAB*©, based on the clinical images dataset. In total, 12 ADDs were obtained with each dosimetry method.

To achieve the main goals indicated above, the following objectives were set:

1. Calibration of CT numbers to tissue parameters for the in-house CT scanner as

input for MC-GATE dosimetry simulations;

2. Quantification of tissues heterogeneity within the NLV and PTV to predict the level of variations between VSV- and MC-ADDs;

3. MC-GATE simulation of a VSV kernel to use in following VSV dosimetry calculations;

4. Computation of VSV- and MC-ADDs, reporting MC-GATE simulations' duration;

5. Comparison of VSV- and MC-ADDs, within the NLV and PTV and at the liver interface with surrounding tissues, to assess the accuracy of VSV dosimetry;

6. Comparison of planning and verification ADDs, within the NLV and PTV, to assess variations in treatment planning quality between VSV and MC-GATE dosimetry methods.

A short investigation was carried out simultaneous to the comparison of VSV- and MC-ADDs to account for radiobiology in the prediction of the therapeutic index. The mean absorbed dose, $\overline{D}$, and the equivalent uniform biologically effective dose (EUBED) within the PTV and NLV were computed for both VSV- and MC-ADDs. These features were compared to assess: (1) variations in the therapeutic index by neglecting or considering radiobiology (i.e., $\overline{D}$ vs EUBED in a ADD), and (2) variations in EUBED by neglecting or considering tissue heterogeneity in ADDs calculations (i.e., EUBED in VSV- vs MC-ADDs).

1.3 Original Contribution

This work contributes to improving RE optimization by assessing the accuracy of VSV dosimetry compared to gold standard MC-GATE dosimetry, especially at the liver interface with surrounding tissue. In addition, the open-source development of MC-GATE scripts for RE dosimetry directly contributes to the NM community.
Developed code available at: https://github.com/mariainesribeiro/MasterThesis.

The research presented in this work was partially submitted to the *EANM'21 Virtual - Annual Congress of European Association of Nuclear Medicine*. It was accepted as a top-rated oral presentation:

- M. Ribeiro, P. Ferreira, F. P. Oliveira, J. Cruz, D. C. Costa, "Comparison of Two ^{90}Y-charged Glass Microsheres Liver Radioembolisation Dosimetry Methods: Voxel S-values and Monte Carlo - GATE,"presented at *EANM'21 Virtual - Annual Congress of the European Association of Nuclear Medicine*, Vienna, Oct. 20, 2021.

1.4 Outline

In addition to the present brief introduction, this work is structured in seven chapters summarized below:

Chapter 2: Fundamentals of Nuclear Medicine in Radioembolization
RE personalize dosimetry requires a multi-disciplinary knowledge in NM scope to optimize treatment deliver. This chapter outlines the fundamental concepts of NM applied to RE personalized dosimetry. First, radiation physics are introduced with a brief description of ^{90}Y and ^{99m}Tc radioactivity, particle interactions with tissues, and common radiation exposure measurements. Second, the relevant NM imaging modalities are described, including SPECT, PET and and CT systems. Third, the desired characteristics of the diagnostic and therapeutic radiopharmaceuticals (RP) are presented generally and specifically for RE[3]. Finally, the key radiobiology concepts derived from external beam radiotherapy (EBRT) are presented along the challenges of radiobiology in RE.

Chapter 3: Radioembolization State of the Art
This chapter presents the state of the art of RE dosimetry. First, a brief description of the liver anatomy and physiology is given. Second, liver cancer epidemiology and current treatment options are listed, putting RE into its clinical context. Third, the recommended procedures for RE treatment planning, delivery and verification are described. Finally, the evolution of RE dosimetry methods is presented.

Chapter 4: Materials and Methods
This chapter describes the methodological approach to achieve the key objectives, including:

1. Description of the retrospective clinical dataset provided by CCU-FC;

2. Stoichiometric calibration of CT numbers to tissue parameters for the in-house CT scanner using a physical phantom;

3. Quantification of tissue heterogeneity within the NLV and PTV based on the obtained calibration of CT numbers and patients' CT images;

4. Computation of ADDs with VSV and MC-GATE dosimetry methods based on planning SPECT/CT and verification PET/CT images, including the simulation of the VSV kernel with MC-GATE;

[3] ^{90}Y – MSs are not recognize as a RP because they are not metabolized, but they should be handle like other RP [2].

5. Comparison of VSV- and MC-ADDs, testing for voxelwise and global agreement and correlation within the NLV and PTV and at the liver interface with surrounding tissues;

6. Comparison of planning and verification ADDs obtained with each dosimetry method, testing for voxelwise and global agreement and correlation.

Chapter 5: Pre-Dosimetry Results

This chapter presents the results obtained for the stoichiometric calibration of CT numbers to tissue parameters, quantification of tissue heterogeneity within the NLV and PTV, and comparison of the VSV kernel simulated with MC-GATE with reference values.

Chapter 6: Dosimetry Results

This chapter presents the results for the comparison of ADDs. First, VSV- and MC-ADDs are tested for agreement and correlation within the NLV and PTV and at the liver interface with surrounding tissues. Then, planning and verification ADDs obtained with each dosimetry method are tested for agreement and correlation to assess treatment planning quality.

Chapter 7: Discussion

This chapter discusses the results obtained in this work. First, the accuracy of the obtained stoichiometric calibration of CT numbers to tissue parameters is indicated. Second, quantification of tissue heterogeneity within the NLV and PTV allows to predict the accuracy of VSV dosimetry in comparison to gold standard MC dosimetry. Third, the feasibility of MC-GATE dosimetry in RE clinical practice is discussed, considering the clinical schedule fitted for VSV dosimetry and the duration of MC-GATE simulations. Finally, the accuracy of VSV dosimetry and the relevance of introducing MC dosimetry in RE optimization are discussed.

Chapter 8: Conclusion

This chapter gathers the final conclusions of this work and suggests future work.

Chapter 2

Fundamentals of Nuclear Medicine in Radioembolization

NM is a medical specialty that employs RPs to diagnose and treat several pathological conditions, especially cancer [11]. RPs combine a radionuclide that allows diagnostic imaging or a therapeutic effect, and a biologically active molecule that carries the radionuclide to the target location in the patient's body [11]. Medical imaging devices are used after administration of RPs to provide information about the functioning of a person's specific organ or to verify correct treatment delivery [2]. RPs and imaging devices are the fundamental tools of NM. In addition, NM is supported by decades of investigations on EBRT.

RE is emerging in the scope of NM as an innovative therapy for unresectable liver tumors. In RE treatment planning, ^{99m}Tc – MAA is administrated to the patient to predict ^{90}Y – MS distribution in tissues through scintigraphy and SPECT/CT images. In RE treatment delivery, ^{90}Y – MSs are administrated to the patient to deliver a high absorbed dose to the tumor, verified through PET/CT images. ^{99m}Tc – MAA is a RP, but ^{90}Y – MSs are not considered as RPs because MSs are unmetabolized [2]. Nevertheless, ^{90}Y – MSs are delivered in aqueous solution - posing the risk of contamination - and contain a radionuclide that yields a therapeutic effect within a target location. Therefore, ^{90}Y – MSs should be handled like any other RP [2].

Radiation emitted by RPs is key for imaging and therapeutic applications, but it can induce toxicity and severe complications. Understanding the mechanisms of radiation interactions in tissues and radiation's biological effects is paramount to ensure patient safety in NM procedures. Moreover, this knowledge contributes to improving dosimetry accuracy in RE, which is the end goal of this work. This chapter outlines the fundamental concepts of NM, including radiation physics, imaging devices, radiopharmacology, and radiobiology in the scope of RE.

2.1 Radiation Physics

Radiation is the transport of energy by electromagnetic waves or atomic particles [12]. Exposure to ionizing radiation can cause biological damage in tissues through direct

or indirect ionization [13]. Direct ionization occurs when charged particles (e.g., electrons) deposit their energy in absorbing tissues through Coulomb interactions or nuclear reactions[1]. In contrast, indirect ionization occurs when neutral particles (e.g., photons and neutrons) first transfer their energy to charged particles. This section describes radiation emission in radioactivity, radiation interactions with tissues, and radiation exposure measures in RE.

2.1.1 Radioactivity

Radiation is emitted through radioactivity as an unstable nuclide spontaneously decays into a more stable nuclide [12]. ^{99m}Tc and ^{90}Y are examples of radioactive nuclides - or radionuclides - and are employed in RE. The main characteristics of radioactive decay are the decay constant, λ, representing the probability of a decay per time unit and the activity, A, defining the number of decays per unit time in a radioactive substance, expressed in becquerel (Bq). The decay law relates these quantities as:

$$A(t) = N_0 \lambda e^{-\lambda t}, \tag{2.1}$$

where N_0 is the initial amount of the parent nuclides in the radioactive substance and t is the decay time [13]. The half-life $t_{1/2}$ gives the time required for halving N_0 and is derived from the equation above as:

$$t_{1/2} = \frac{ln(2)}{\lambda}. \tag{2.2}$$

Decay chains define the possible sequential decay events between a radionuclide and a stable nuclide. Three decay modes are relevant in NM: alpha decay (emitting helium nucleus), beta decay (emitting electrons and antineutrinos or positrons and neutrinos), and gamma (γ) decay (emitting γ-rays) [13]. In RE scope, ^{99m}Tc and ^{90}Y decay mainly through γ and beta-minus (β^-) emissions, respectively.

A γ-decay occurs after another decay process that resulted in a daughter nuclide in an excited state [13]. In pure γ-decay, the excited atom reaches the ground state instantaneously through the emission of a photon of well-defined energy. In a isomeric transition, the γ-emission takes more than one nanosecond and the parent nuclide is said to be in a metastable state [13]. ^{99m}Tc is a metastable nuclide that decays to ^{99}Tc by isomeric transition over 99% of the times and with $t_{1/2}$ = 6.01 hours [14], as illustrated by ^{99m}Tc decay scheme in Figure 2.1. Around 89% of γ-emissions occur at 140.5 keV [14]. In RE treatment planning, SPECT imaging systems can depict the distribution of ^{99m}Tc-MAA in tissues by detecting these γ-emissions of 140.5 keV. SPECT systems are introduced in Section 2.2.1.

[1] Nuclear reactions are less probable and less relevant for clinical applications.

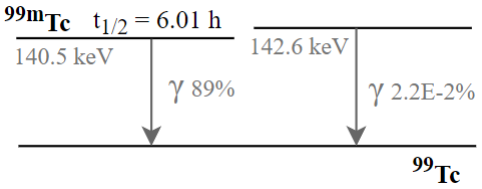

Figure 2.1: ^{99m}Tc decay scheme. Retrieved from: [14]

In β^- decay, a radionuclide transforms a neutron into a proton and ejects a β^- particle (i.e., an electron) and an antineutrino [13]. ^{90}Y decays to zirconium-90 (^{90}Zr) with $t_{1/2}$ = 64.05 hours and it is considered to be a pure β^- emitter, as illustrated by ^{90}Y decay scheme in Figure 2.2. ^{90}Y decay includes a minor branch to the first excited state of ^{90}Zr that emits γ-rays of 1760 keV with an intensity of 0.015 % [15]. In RE treatment verification, the interaction of these γ-rays with tissues allow PET imaging systems to depict the distribution of ^{90}Y – MS in tissues. PET systems are introduced in Section 2.2.2.

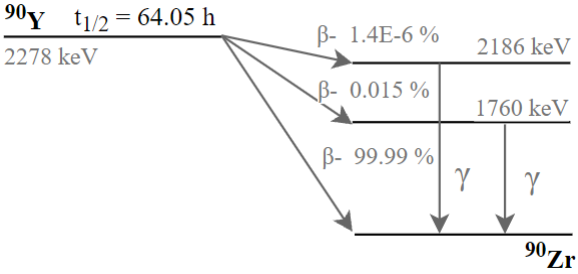

Figure 2.2: ^{90}Y decay scheme. Retrieved from: [15]

The main characteristic of β^- decay is the continuous energy spectrum of the β^- particle, between zero and the mass difference between the parent and the daughter nucleus [12]. The average energy of the β^- particle is approximately one-third of the endpoint energy. Figure 2.3 displays the β^- spectrum of ^{90}Y, with a mean energy of 932 keV and an end-point energy of 2278 keV [16].

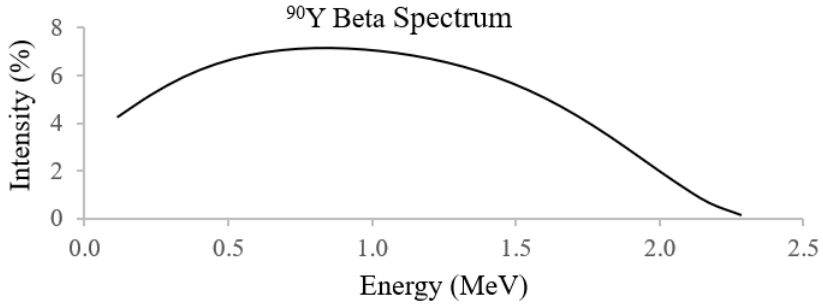

Figure 2.3: ^{90}Y beta energy spectrum, with a mean energy of 932 keV and an end-point energy of 2278 keV. Adapted from: [16].

2.1.2 Photons Interactions with Tissues

In RE, the decay chains of ^{99m}Tc and ^{90}Y directly or indirectly yield photons that interact with surrounding tissues. In the clinical energy range, as a photon beam penetrates a tissue, it can interact with (1) the tightly bound electrons in the photoelectric effect (PEE) and Rayleigh scattering (RS), (2) the loosely bound orbital electrons in Compton scattering (CS), or (3) the electrostatic field of the atomic nucleus in pair production (PP) [13]. A physical cross-section gives the probability of each interaction type. Figure 2.4 illustrates photons interactions with tissues, described in detail below.

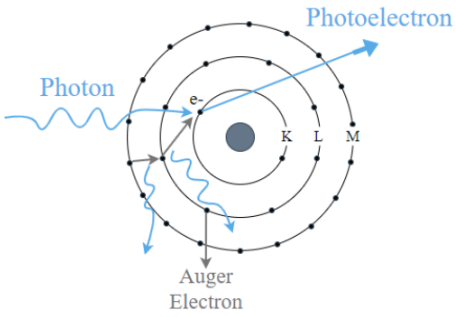

(a) PEE: a photon interacts with an inner shell electron, which is ejected.

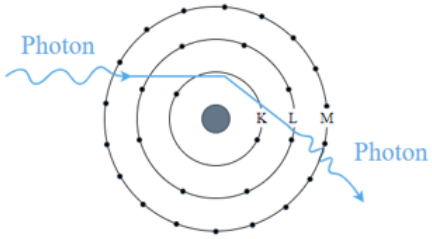

(b) RS: a photon is scattered without energy loss.

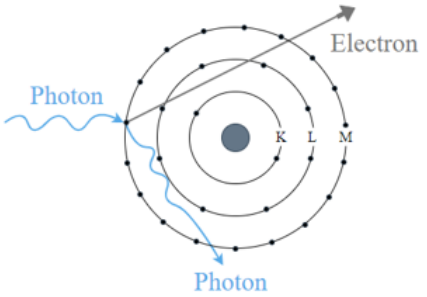

(c) CS: a photon is scattered with energy loss loss

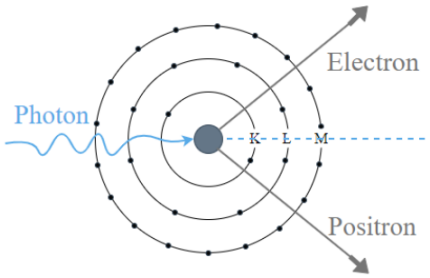

(d) PP: a photon is annihilated, and an electron and a positron are created.

Figure 2.4: Photons interactions with tissues. Adapted from [17].

In PEE (Figure 2.4a), a photon transfers all its energy to a bounded electron that leaves the atom with kinetic energy [18]. The ejected electron, usually called photoelectron, deposits its energy in the surrounding areas. An outer shell electron fills the vacancy left in the electron shell, with the emission of a photon of well-defined energy (characteristic X-ray) or an electron (Auger electron) [17].

Scattering interactions might be coherent or incoherent. In RS (Figure 2.4b), a low-energy photon is scattered by the electron cloud, without energy loss [13]. Thus, this interaction does not contribute to energy deposition in tissues through the generation of free charged particles. In CS (Figure 2.4c), the incoming photon transfers part of its

energy to an outer shell electron. As a result, the electron is ejected, and the photon is scattered in a continuous spectrum of energies [17].

In PP (Figure 2.4d), the nuclear Coulomb field of an atom annihilates a high energy photon, creating an electron and a positron with equal kinetic energy. The photon energy threshold is 1.022 MeV - the sum of the electron and positron rest masses [17].

Overall, photon interactions with tissues result in photon beam attenuation, i.e., the number of photons in a beam decreases while penetrating tissues. Beam attenuation has been extensively studied in the scope of EBRT. In RE, photons are not generated in a beam, instead they are emitted by administrated radionuclides. Nevertheless, measures of beam attenuation are relevant to parameterize RE dosimetry with MC simulations, as explained in Chapter 4.

Each interaction type contributes differently to the macroscopic beam attenuation, according to the photon energy, E, and the tissue parameters, such as the atomic mass, Z, and mass density, ρ. The macroscopic attenuation of a monoenergetic narrow photon beam of intensity I in an homogeneous medium of thickness x is expressed as:

$$I(x) = I_0 e^{-\mu x}, \tag{2.3}$$

where I_0 is the initial beam intensity and μ is the total linear attenuation coefficient. The coefficient μ characterizes the fraction of photons that is attenuated per unit length in the medium and is given by:

$$\mu = \rho \, \sigma_{\mathrm{T}} \, N, \tag{2.4}$$

where σ_{T} is the total cross-section of all possible photon interactions and N is the number of atoms per unit volume. Note that μ depends on the medium mass density, and hence the mass attenuation coefficient μ/ρ is usually employed to compare attenuation in different mediums [18].

Figure 2.5 plots the relative predominance of the three photon interactions that contribute to beam attenuation and energy deposition in tissues (i.e., PEE, CS, and PP) for mediums with different atomic number, Z, as a function of the photon energy, E. The linear attenuation coefficient of each interaction describes its relative predominance: τ for PEE, σ for CS, and κ for PP. In the diagnostic energy range up to 150 keV, PEE predominates and τ is proportional to Z^5/E [13]. CS is most relevant at higher E used in EBRT, as σ decreases with E and increases with Z for $E > 1$ MeV [13]. Finally, PP only occurs for $E > 1.022$ MeV and κ increases above this threshold and varies with Z^2. In RE, PEE predominates for γ emissions of $^{99\mathrm{m}}$Tc at 140.5 keV, and PP can occur for γ emissions following ^{90}Y decay to the first excited state of ^{90}Zr.

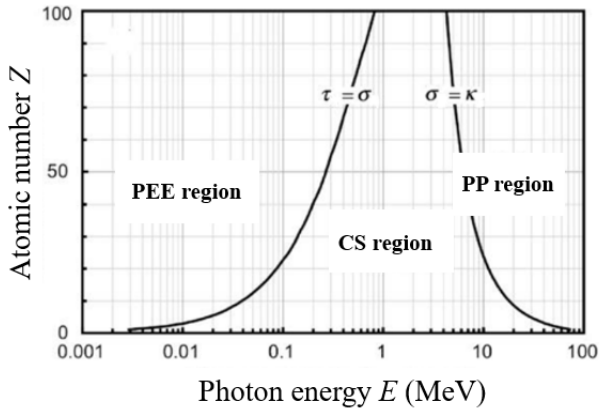

Figure 2.5: Relative predominance of the three main photon interactions with mediums of different atomic number, Z, as a function of the photon energy, E. Retrieved from: [13]

Figure 2.6 shows exponential attenuation profiles of photon narrow-beams of different energy in water. Higher energy photons have a higher penetration power at any given depth. Figure 2.7 displays attenuation profiles of 140 keV (the characteristic energy for γ-emissions of ^{99m}Tc decay) in three standard materials: lungs, water, and bone. Photons penetrate more in the lungs than in water or bones. Overall, it is clear that photons are highly penetrating in human tissues and can travel long distances within a patient's body [12].

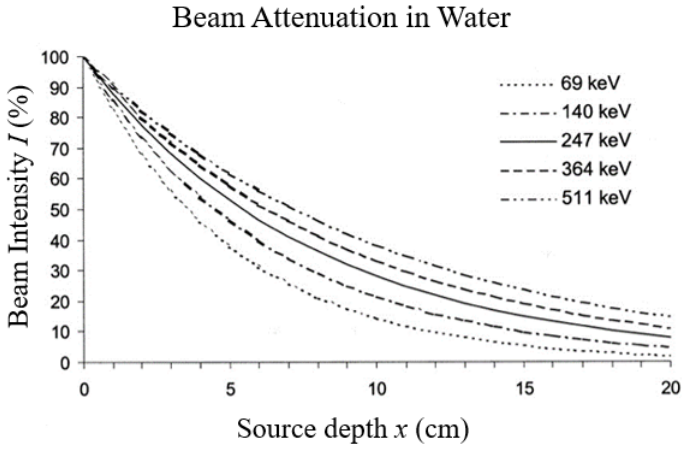

Figure 2.6: Beam intensity as function of source depth in water phantom for photons of different energies. Retrieved from: [19]

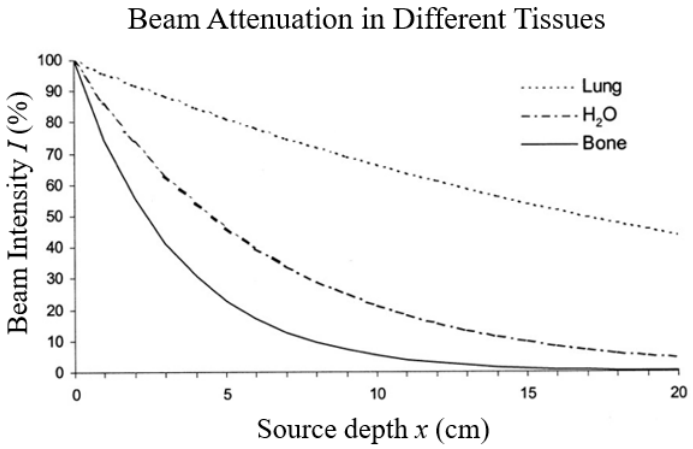

Figure 2.7: Beam intensity as function of source depth in water phantom for 140 keV and different attenuating media. Retrieved from: [19]

Two special tissue thicknesses are commonly used in EBRT to describe the photon beam attenuation in tissues: the half-value layer (HVL), and the mean free path (MFP). The former is the thickness of the medium that halves the initial beam intensity, and the latter is the expected distance that a photon goes through the medium without interacting with it [13]. These quantities depend on μ according to Equation 2.1, as:

$$HVL = \frac{-ln(1/2)}{\mu}, \tag{2.5}$$

and

$$MFP = \frac{1}{\mu}. \tag{2.6}$$

2.1.3 Electrons Interactions with Tissues

In RE, ^{90}Y – MSs emit electrons that travel through tissues and interact with them. Electrons deposit their energy in tissues - contributing to dose absorption - through a high number of collisions and radiation losses until they are finally stopped [13].

In collision losses, electrons interact with bound atomic electrons, yielding excitation or ionization of target atoms in the tissues. The ionizing potential defines the minimum energy required to induce ionization, i.e., to eject orbital electrons. While high energy electrons can interact with inner shell electrons (hard collisions), lower energy electrons can only interact with valence electrons (soft collisions) [17]. In RE, collision losses of β^- radiation emitted by ^{90}Y yield energy deposition in tissues, contributing to the local dose absorption.

In radiation losses, an incident electron is scattered by nuclei in the tissue and looses energy to a secondary photon, referred to as Bremsstrahlung radiation. The energy

spectrum in inelastic scattering is continuous, ranging from zero to the kinetic energy of the incident electron [13]. In RE, radiation losses of β^- radiation emitted by ^{90}Y are a concern because Bremsstrahlung radiation can yield energy deposition in tissues away from the radiation source, contribution to dose absorption away from ^{90}Y – MSs.

The stopping-power, S, defines the average energy deposited by a charge particle in a medium per unit path length [20]. Considering the charged particle to be an electron, the stopping-power is the sum of the collision stopping-power, S_{col}, with the radiation stopping-power, S_{rad}. Each component depends on the energy, E, of the incident electron and on the mass density, ρ, and atomic number, Z, of the medium. The mass stopping-power, S/ρ, is usually used to describe electrons' energy loss in different media because it is independent of the medium's mass density.

Figure 2.8 illustrates the relationship between the two stopping-power contributions in soft tissues as a function of the electron energy. Collision losses to Bremsstrahlung radiation are small in low atomic number mediums and increase as the electron energy and the atomic number increase [21]. For example, only 1.4% of the stopping-power in soft tissues is related to the radiation component for 1 MeV electrons [21].

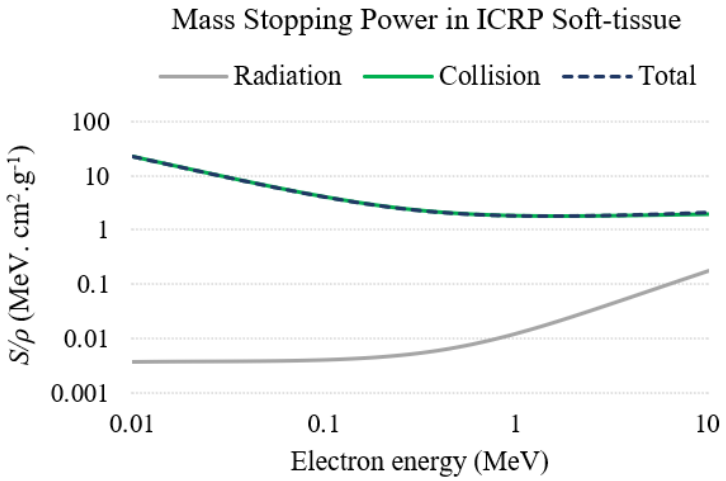

Figure 2.8: Mass stopping power in ICRP soft-tissue medium as a function of electron energy. Data collected from: [21]

The electron range in tissues depends on the stopping-power and is usually short. In RE, electrons emitted by ^{90}Y penetrate on average only 2.5 mm in soft tissues, reaching a maximum of 11 mm. This small range allows inducing biological radiation effects only near the radiation sources. Figure 2.8 shows that radiation losses are small in the energy range of β^- particles emitted by ^{90}Y, minimizing radiation effects away from the radiation sources by yielding only a reduced amount of highly penetrating secondary photons.

In addition to electron emissions, the less frequent γ-emissions after ^{90}Y decay

(Figure 2.2) can produce positrons through PP. Positrons interact with tissues in a similar fashion to electrons, suffering collision and radiation losses. However, just before positrons are completely stopped, they are annihilated as illustrated in Figure 2.9.

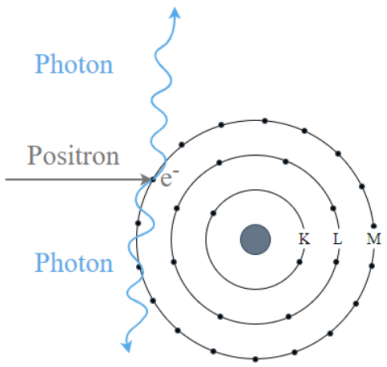

Figure 2.9: Annihilation: an incident positron interacts with an orbital electron, resulting in two 511 keV photons going in the opposite direction. Adapted from [17]

In annihilation, a positron is attracted by an orbital electron and both particles are converted into two photons of 511 keV emitted in opposite directions. In RE treatment verification, positron annihilation occurs after PP of photons emitted after ^{90}Y decay to the first excited state of ^{90}Zr. Photons pairs allow PET systems to depict the distribution of ^{90}Y – MS in tissues [17], as explained in the upcoming Section 2.2.2.

2.1.4 Radiation Exposure Measures

The accurate measurement of radiation exposure is highly important in all medical uses because it induces biological responses in tissues. The most widely used quantity to describe radiation dose is the absorbed dose, D, defined as the mean energy imparted, $\overline{E}$, by ionizing radiation to tissues per unit mass, m, following [22]:

$$D = \frac{d\bar{E}}{dm}. \tag{2.7}$$

Voxelized ADDs describe the spatial distribution of absorbed dose in a 3D matrix and allow to quantify the radiation-induced biological effects in tissues. Section 2.4 introduces relevant radiobiology concepts to understand RE.

Dose-volume histograms (DVH) have been used in EBRT - and recently in RE - to describe ADDs within segmented VOIs. There are two useful mathematical forms of DVHs: (1) the differential DVH (dDVH) plots the relative volume receiving absorbed doses in a specified range, and (2) the cumulative DVH (cDVH) plots the relative volume receiving absorbed doses greater than or equal to a given value [22]. DVHs allow to assess the ADD uniformity in the target volume, identify hot spots (high absorbed dose

volumes in normal tissues), and predict tumor control probability (TCP) and normal tissue complications probability (NTCP) [22].

2.2 Imaging Methods: instrumentation and image formation

Medical images depict different characteristics of a patient body in a non-invasive way. In the scope of NM and RE, SPECT and PET systems map the distribution of radionuclides in tissues and allow to diagnose diseases and plan or verify patient-specific treatment strategies [23]. Hybrid SPECT/CT and PET/CT systems add anatomical information and improve imaging accuracy [24]. This section describes SPECT, PET, and CT imaging devices and an alternative to hybrid modalities with fiducial markers (FM).

Modern medical images are digital, i.e., they are represented by a matrix of numeric elements: pixels in 2D images and voxels in 3D images. The pixel or voxel size relates the number of matrix elements and the field-of-view (FOV) size. Digital image quality is described by many parameters, such as spatial resolution, energy resolution, sensitivity, and noise [25]. Table 2.1 describes these parameters for NM imaging modalities.

Table 2.1: Definition of image characteristics in NM [25].

Characteristic	**Definition**
Spatial Resolution	Minimum distance between two radioactivity sources such that they can be discriminated. It is expressed in terms of full width at half maximum (FWHM) of a point spread function.
Energy Resolution	FWHM of the energy distribution measured from a mono-energetic radioactivity source
Sensitivity	Percent of detected photons from a known radiation activity
Noise	Uncertainty in pixel/voxel counts due to the random decay of radiation. It is Poisson distributed.

2.2.1 SPECT

Gamma-cameras produce planar scintigraphy or tomographic SPECT images of *in vivo* radioactivity distribution by measuring photon emissions of an injected radionuclide [26]. Pixel or voxel values represent photon counts emitted in a position of the patient's body and are proportional to the local radionuclide concentration. In RE treatment planning, gamma-cameras can quantify the distribution of ^{99m}Tc-MAA because ^{99m}Tc emits characteristic photons of 140.5 keV. In RE treatment verification, gamma-cameras could quantify the distribution of ^{90}Y-MS because the β^- radiation emitted by ^{90}Y yields Bremsstrahlung photons in tissues, but spatial resolution would be poor.

Gamma-cameras and SPECT scanners comprise one to three heads that map photons onto 2D views, and a gantry that allows 3D imaging by moving the head around the patient, as illustrated in Figure 2.10 [25]. Each head is built of two main components: a collimator and a detector. The collimator limits detection to photons (X-rays or γ-rays) traveling at right angles to the detector[2], estimating the direction of the photon origin in the patient [25]. The detector comprises scintillation crystals made of sodium iodide doped with thallium (NaI(Tl)) that convert an incident photon into visible light. Then, an array of photomultiplier tubes converts this light into an electrical signal with high gain [25]. After detection of several photons in a single gamma camera angular orientation, a computer system processes the photomultiplier tubes' output signals to return a 2D image histogram of the counted photons along each direction defined by the collimator, i.e., the line integrals [26].

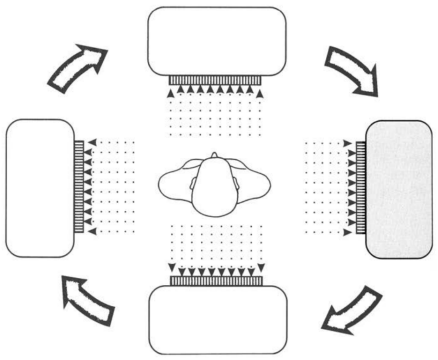

Figure 2.10: SPECT system: a gamma camera rotating around the patient to acquire multiple views. Retrieved from: [27].

Gamma cameras detect photons in a wide range of energies, while diagnostic radionuclides emit characteristic rays. In RE treatment planning, ^{99m}Tc emits mostly γ-rays at 140.5 keV. However, less energetic photos produced through CS interactions of the primary γ-rays with tissues are also detected because the collimator is incapable of rejecting them [28]. Figure 2.11 displays the photon counts per energy in a SPECT acquisition following an injection of ^{99m}Tc – MAA. Despite the evident counts' peak at around 140 keV, scattered γ-rays are detected at lower energies. SPECT systems can reject γ-rays that lie outside a pre-defined energy window of interest (usually [135-145] keV) in a first approach to attenuation corrections.

The mathematical problem of computed tomography in SPECT, represented in Figure 2.12a, consists of obtaining a 3D image of a patient through a set of 2D views acquired at different angles. In each 2D view, $g(s,\theta)$ describes multiple line integrals of photons detected at any position along a cross-sectional slice, s, at an angular position, θ. These line integrals are corrupted by photon attenuation and scattering in the tissues,

[2]There are special collimators for low-, medium- and high-energy photons.

degrading image accuracy [28]. The unknown quantity $f(x,y)$ represents the number of photons emitted at any point (x,y) in the cross-sectional slice, related to the local RP concentration [29].

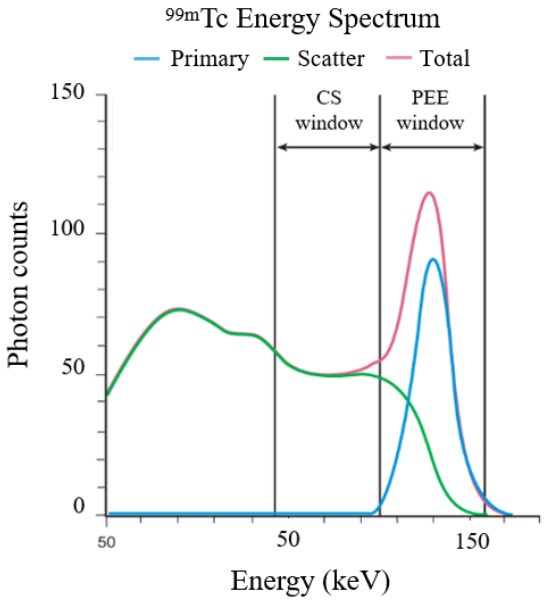

Figure 2.11: Photon counts per energy in a SPECT acquisition for a ^{99m}Tc point source in an attenuating medium. Retrieved from: [28].

In each planar view, photons emitted at different depths along the same direction contribute to counts in the same position along cross-sectional slice, s (Figure 2.12a). Thus, only multiple views can define the original position of the photon emission [30]. A sinogram organizes multiple projections of a cross-sectional slice acquired at different angles, as in Figure 2.12b. The Randon transform theorem allows to mathematically reconstruct a 2D cross-sectional image of a patient from a sinogram [30]. Collections of successive cross-sectional slices represent the typical medical 3D images.

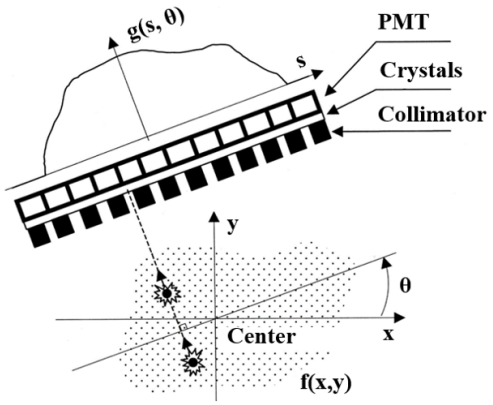

(a) At each angle θ, 2D projections $g(s,\theta)$ are acquired along direction s. Adapted from [30]

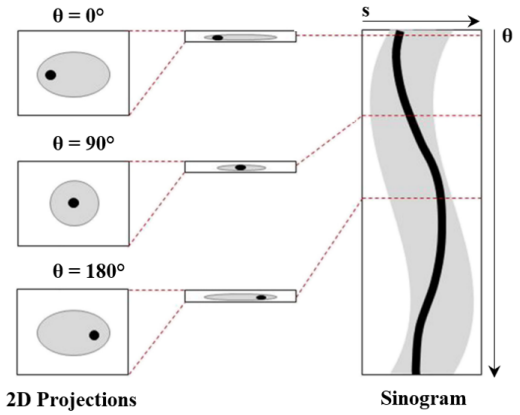

(b) Planar views acquired at different angular orientations build a sinogram. Adapted from [31]

Figure 2.12: Principle of tomographic acquisition and geometric considerations.

The algorithms used for the reconstruction of 3D images are categorized as analytical methods, such as filtered backpropagation (FBP), or interactive methods, such as maximum likelihood expectation maximization (MLEM), ordered-subsets expectation-maximization (OSEM), or more specific algorithms developed by vendors, such as the Astonish[3]. The former are faster, but the latter feature attenuation and scatter corrections in hybrid equipment (combining SPECT and CT) [32]. In this work, images were reconstructed by the OSEM or Astonish algorithms.

SPECT devices achieve a spatial resolution typically in the range of 8 to 15 mm, depending on many factors, such as the collimator type, the detector stopping-power, crystals dimensions and light output, the number of photomultiplier tubes, the patient-detector distance and the reconstruction algorithm [26]. Energy resolution is typically 9.5% at 140 keV for NaI(Tl) crystals [25]. Sensitivity is below 0.01%, which is very low due to the use of a collimator and a limited number of detector heads [25].

2.2.2 PET

PET systems produce tomographic images of *in vivo* radioactivity distribution by measuring positron emissions of an injected radionuclide. The principle of PET imaging is the detection of two coincidence 511 keV photons travelling in opposite directions after positron annihilation within a short-range in tissues. In RE treatment verification, a PET system can quantify the distribution of ^{90}Y – MS because positron annihilation occurs following PP of photons emitted after ^{90}Y decay to the first excited state of ^{90}Zr.

[3] Astonish is an OSEM optimized for Philips gamma-cameras

A PET system comprises parallel rings of detectors that surround the patient and define the possible lines of response (LOR) for coincidence detection, as in Figure 2.13. Each ring simultaneously detects photons arriving from multiple angles in a cross-sectional slice [26]. Individual detectors are very similar for SPECT and PET systems, but PET systems require crystals of higher stopping-power values for 511 keV photons [26]. Lutetium oxyorthosilicate or lutetium yttrium oxyorthosilicate scintillation crystals are commonly used [33].

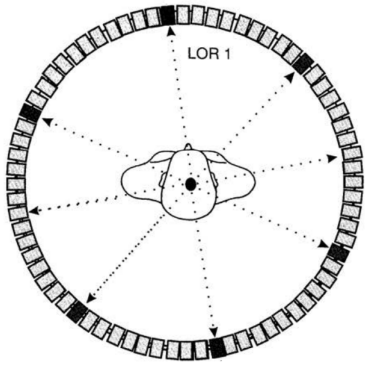

Figure 2.13: PET system: a ring of detectors identify the LOR along which the emission and annihilation of positrons occurred. Adapted from: [27]

PET systems identify coincidence photons originating at the same annihilation event if there is an overlap between electrical pulses of two separate detectors within in a predefined time window [34]. Each coincidence annihilation event is associated with a LOR, and the number of events in each LOR is proportional to the integral activity distribution along that LOR [26]. Modern time-of-flight (TOF) PET systems narrow down the annihilation position along LOR to a 1.5 cm line based on the time difference between the detection of coincidence photons (Figure 2.14). As a result, TOF-PET systems achieve better spatial resolution [33].

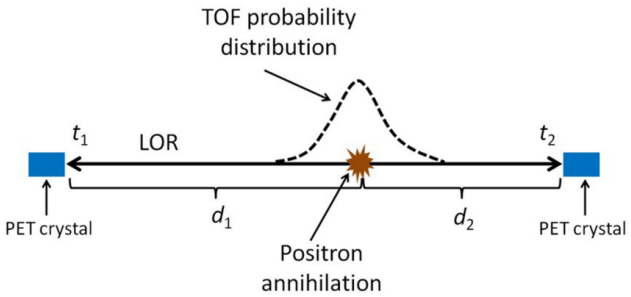

Figure 2.14: Illustration of the TOF principle. A positron annihilation originates two photons that are detected by two PET detectors in a LOR. Taking the time difference ($t_1 - t_2$) between detection and speed of light, the annihilation distance difference ($d_1 - d_2$) to both detectors can be computed and associated with a probability distribution. Retrieved from: [33]

Many coincidence events are recorded at multiple LORs for successive cross-sectional slices, estimating the line integrals of radioactivity that represent 2D views. Image reconstruction of PET images is similar to SPECT, relying on the Randon transform and employing the same analytical or iterative algorithms [25].

A significant advantage of PET systems over SPECT systems is their significantly higher sensitivity (1% vs 0.01%) that improves image quality and reduces acquisition time [35]. Moreover, PET clinical systems can also achieve better spatial resolutions, ranging from 2.4 mm [25]. For these reasons, RE treatment verification employs PET systems to quantify the distribution of ^{90}Y – MS. Several factors limit PET spatial resolution nevertheless, including the width and count of detector elements, the positron range in tissues, the distance between opposing detectors, and the penetration of the incident photons on the detector [36]. Energy resolution depends on the detector crystal properties at 511 keV peak and is around 10 % for lutetium oxyorthosilicate [35].

2.2.3 CT

CT systems measure transmission profiles of X-rays penetrating a patient and depict tissues density variations inside the body [37]. In RE treatment planning and verification, CT images provide information on tissues heterogeneity and facilitate segmentation of the relevant anatomical structures. CT systems provide a higher spatial resolution than SPECT and PET systems, achieving sub-millimetre values in clinical systems [37].

The main components of a CT system include an X-ray generator, a gantry with a ring of detectors and a computer. An X-ray generator produces fan-shaped X-ray beams controlled by user-defined parameters, such as current and peak kilovolts, as illustrated in Figure 2.15 [38]. The X-ray generator scans the patient in a helical fashion, i.e. the patient table translates continuously as the gantry rotates the X-ray tube around the patient [38]. During the scanning process, the array of detectors records the intensity of the beam penetrating through the patient [38]. As a result, multiple attenuation profiles are acquired at different angles and for successive cross-sectional slices. 3D image reconstruction is possible through tomographic mathematical operations, just like in SPECT or PET.

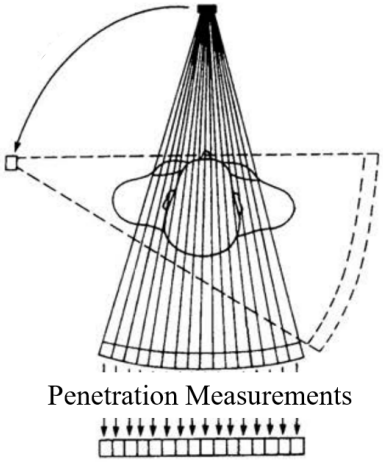

Figure 2.15: CT system: an X-ray beam scans the patient and the attenuation profiles are measured in an array of detectors. Adapted from: [27]

The Hounsfield unit (HU) scales the attenuation profiles for each voxel in a reconstructed CT image by relating attenuation values in different tissues to the attenuation of water, as:

$$HU = (\frac{\overline{\mu}}{\overline{\mu}_{H_2O}} - 1) \times 1000 \tag{2.8}$$

where $\bar{\mu}$ is the linear attenuation coefficient of the local tissue and $\overline{\mu}_{H_2O}$ is the water linear attenuation coefficient [39]. Different tissues are associated to characteristic ranges of HU values and allow to depict anatomical structures in a gray scale.

2.2.4 Hybrid SPECT/CT and PET/CT advantages

Hybrid SPECT/CT and PET/CT systems provide higher imaging accuracy because CT attenuation profiles provide means for attenuation and scatter corrections of SPECT and PET images and add anatomical data with good spatial resolution that eases segmentation of VOIs [28]. When hybrid systems are not available, co-registration of separate images provide a similar output after a resampling step. FMs can be attached to the patient skin in the FOV to allow image alignment in the co-registration step. Figure 2.16 displays a cross-sectional view of co-registered SPECT and CT images of a RE patient, revealing a FM in both imaging modalities.

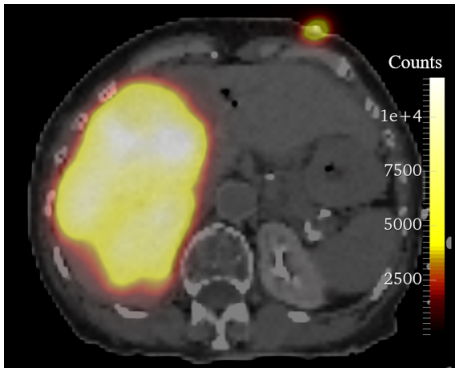

Figure 2.16: Cross-sectional view of co-registered SPECT and CT images, acquired in RE treatment planning. A FM is shown at the skin surface in the left-upper corner. Color bar represents photon counts.

FMs are visible in CT images because they are made of a radiopaque material. PET and SPECT systems can also spot FMs if a small amout of a visible radionuclide has been injected in the central hole of FMs. In RE treatment planning, around 1 MBq of ^{99m}Tc can be injected into FMs to allow co-registration of SPECT and CT images.

2.3 Radiopharmacology

Radiopharmacology studies RPs and their interactions with living organisms. In diagnostic imaging, RPs are administrated to enable quantitative measures of activity distribution with medical imaging devices [40]. In the treatment modality, RPs aim to deposit a high radiation dose in a diseased organ (e.g. to kill tumor cells), yielding a therapeutic effect [11]. This section summarizes the key concepts in both diagnostic and therapeutic RPs relevant in RE scope.

2.3.1 Diagnostic Radiopharmaceuticals

RPs in diagnostic imaging are also called tracers because they map a specific physiological or pathological process in the body. Imaging methods, already described above, allow to quantitatively depict the tracers distribution in target locations, as 2D or 3D images that represent the desired functional conditions. Examples of diagnostic applications using RPs are exams to blood flow in the brain, functioning of the liver, lungs, heart or kidneys, and bone metabolism [11]. In RE treatment planning, 75-150 MBq of ^{99m}Tc – MAA are injected through the hepatic artery and a SPECT system estimates their distribution to predict the distribution of ^{90}Y – MSs [41].

RPs used in medical imaging shall have the following characteristics: (1) the decay

of the radionuclide should be in the detector specific energy ranges ([100;200] keV for gamma cameras and 511 keV for PET cameras) and in sufficient intensity for tomographic techniques; (2) the decay mode should not include particle emission to minimize dose absorption in patients; (3) the radionuclide half-life should be of a few hours; (4) the RP should not have toxicity or manifest physiological effects; (5) the RP should not dissociate *in vivo* or *in vitro*; (6) the RP should reach the target organ quickly and accurately [11]. Overall, an ideal diagnostic RP has null therapeutic effect and deposits an insignificant radiation dose in the patient. However, any use of RPs induces radiation exposure risks, which should be avoided or minimized.

In RE treatment planning, ^{99m}Tc – MAA is employed because it has similar biokinetics to ^{90}Y – MSs, allowing to predict its distribution. In addition, it checks for all the requirements of diagnostic RPs mentioned above. First, ^{99m}Tc is the most suitable radionuclide for SPECT imaging due to its high intensity γ-ray emission at 140.5 keV with a short half-life [25]. Second, ^{99m}Tc emits only low-energetic β^- particles with a low intensity, allowing to minimize radiation exposure risks and ensure patient safety [42].

2.3.2 Therapeutic Radiopharmaceuticals

RP therapy (RPT) is defined as the systemic or local administration of RPs to internally irradiate and kill tumor cells. The key advantages of RPT is that it selectively deposits high radiation dose in the target volume, while sparing the surrounding normal tissues from toxicity [40]. RPT also benefits from NM imaging techniques to potentiate personalized treatment planning and verification with patient-specific dosimetry calculations [6].

Some characteristics mentioned for diagnostic RPs are even more relevant in RPT. For example, if RPs are poorly targeted to the tumor or if they dissociate *in vivo*, they deposit high radiation doses to normal tissues [40]. The half-life of RPT radionuclides should also be of a few hours to facilitate the logistics of distribution from the manufacturer and yield the desired dose-rate and therapeutic effect [40]. Ideally, RPT radionuclides decay should also be detectable by imaging devices to allow treatment verification.

In contrast to diagnostic RPs, therapeutic RPs should yield a therapeutic effect. Hence, RPT radionuclides emit either beta or alpha radiation to deliver high radiation dose locally [40]. The linear energy transfer (LET) coefficient describes the ratio of energy transferred by a charged particle to the tissues per unit length. Alpha particles have a greater LET than beta particles, depositing a higher radiation dose in a shorter range. Beta particles are preferred when a higher penetration power is relevant to cover more tumor volume [40].

In RE, the preferential uptake of ^{90}Y – MS in the tumor and the range of ^{90}Y β^- radiation allow to achieve high absorbed dose in the tumor volume, while keeping the parenchyma toxicity low [43]. As mentioned before, ^{90}Y – MSs are not considered a RP and RE is not a RPT because the MSs are not a biologically active molecule. Nevertheless, the characteristics and requirements of therapeutic RPs apply to ^{90}Y – MSs as they contain a radionuclide that aims for a therapeutic effect in a target location and that should be detectable by imaging systems. In RE treatment verification, a PET system can quantify the distribution of ^{90}Y – MS because positron annihilation occurs following PP of photons emitted after ^{90}Y decay to the first excited state of ^{90}Zr.

Two types of ^{90}Y – MSs are commercially available: glass (Therasphere®) and resin (SIR-Spheres®). The choice between the two MS depends more on the institutional experience, as no clinical trial has determined clinical superiority for neither of them [44]. In the remainder of my work, RE is only described in the context of glass MS because the NM-Radiopharmacology group at CCU-CF exclusively employs them in the management of liver cancer. Table 2.2 summarizes the key characteristics of ^{90}Y glass MS and ^{90}Y radioactive decay, already described in section 2.1.

Table 2.2: Characteristics of ^{90}Y glass MS. Adapted from [7], [45]

Characteristic	**Definition**
^{90}Y **glass Microspheres**	
Commercial name	TheraSphere®
Particle size	20 to 30 μm
Number of spheres per vial	1.2 to 8 million
Activity per vial	3, 5, 7, 10, 15, 20 GBq
^{90}Y **radiation**	
Decay mode	Pure β^-
Mean energy	932 MeV
Maximum energy	2278 MeV
Mean range in tissues	2.5 mm
Max range in tissues	11 mm

2.4 Radiobiology

Radiobiology studies the biological effects of ionizing radiation on cells, tissues and organs, both normal and diseased. Currently, insights into radiobiology play a major role in treatment planning of EBRT [46]. However, the knowledge gained over decades in EBRT cannot be applied directly in RPTs or RE because these therapeutic modalities exhibit divergent radiation characteristics [46]. This section provides the fundamentals of radiobiology studied on a EBRT context and presents its challenges in RE.

2.4.1 Cellular Radiation Effects

At a microscopic level, ionizing radiation deposits energy in cells almost instantaneously ($< 10^{-18}$ s), leading to ionization events [47]. Electrons can damage biological structures through chemical interactions. At a macroscopic level, radiation induces tissue functional deterioration after lethal damage being inflicted to a large number of cells. This might take between a few minutes to decades [47].

Radiation therapies ultimately aim to damage and kill tumor cells or prevent their reproduction [48]. The radiobiology paradigm states that DNA is the main cellular target to promote radiation-induced cell death, through division delay, reproductive failure or apoptosis [47]. Only a portion of DNA lesions yields permanent effects because DNA repair systems undo damage to same extent. Modern radiobiology experiments show that non-targeted and non-DNA radiation damage also plays a role in radiation response [48].

2.4.2 Radiation Response Factors

Several radiation and biological factors determine the degree of biological damage induced by radiation exposure. Radiation factors include the LET value and the dose-rate. Biology factors include the cell-cycle phase, cell repair capability, and cell type.

High-LET radiation leads to denser distributions of ionization in DNA and greater levels of biological damage. Conversely, low-LET radiation induce smaller amount of damage in tissues, but travel the longest distances [49]. Alpha and beta radiation have high LET, and γ-rays and X-rays have low LET. As the LET value influences the spatial damage rate, the dose-rate describes the temporal damage rate. There is a higher chance of repair for slower dose-rates and thus, more cellular damage can be reversed [50]. In RE, β^- radiation emitted by ^{90}Y – MS has high LET and low dose-rates.

Biological factors influence radiosensitivity [47]. Throughout the cell cycle, radiosensitivity is the greatest after DNA synthesis and during mitotic phases because there is a lower chance of chromosomal repair [51]. Cells with higher repair capacities undergo less permanent damage [50]. Rapidly dividing tumor cells are more radiosensitive than normal cells.

2.4.3 Radiobiology in EBRT

The linear quadratic (LQ) model has been used in radiobiology to describe the cell survival fraction, SF, after radiation exposure and is expressed as:

$$SF = exp(\alpha D + \beta D^2), \tag{2.9}$$

where α and β are radiosensitivity coefficients. In the DNA-target theory, the α term reflects cell death from 'single hit' events proportional to the absorbed dose D, while the β term represents 'multiple hit' cell death resulting from the interaction of sub-lethal damage from different radiation tracks, proportional to D^2 [49].

The degree of curvature in the survival fraction is frequently defined in terms of the α/β ratio, in Gy. Figure 2.17 evidences that cells with high α/β ratios see a relatively constant rate of cell killing with increasing absorbed dose, while those with a low α/β ratio show a pronounced curvature [49]. Tumor cells have high α/β ratios (7-10 Gy), revealing a higher radiosensitivity for small absorbed doses compared to normal tissues with low α/β ratios (3-5 Gy) [49]. EBRT fractionation preferentially spares the less radiosensitive normal tissues by delivering sparsed lower radiation exposures, allowing an escalation of the absorbed dose in the tumour. In RE, fractionation does not apply because ^{90}Y – MS are delivered in a single administration procedure, but radiosensitivity of different tissues is still relevant due to a slower dose-rate throughout ^{90}Y decay.

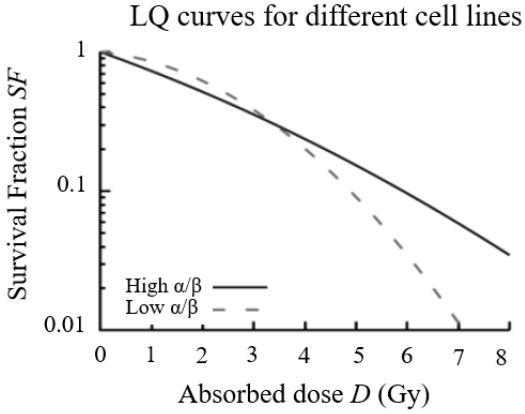

Figure 2.17: Illustration of LQ curves for cell lines with high and low α/β ratios. Retrieved from: [49]

The LQ model is used in EBRT to assess the biological effective dose (BED) [46], i.e., the effect of the absorbed dose in tumors uniformly delivered in multiple fractions, and is given as:

$$BED_{\mathrm{EBRT}} = D \times \left(1 + \frac{D/N_{\mathrm{f}}}{\alpha/\beta}\right), \tag{2.10}$$

where D is the total dose delivered throughout N_{f} fractions [45]. The LQ model is also used in EBRT to assess the TCP and NTCP. Figure 2.18 plots the TCP and NTCP sigmoid curves in function of the absorbed dose D, derived from the LQ model.

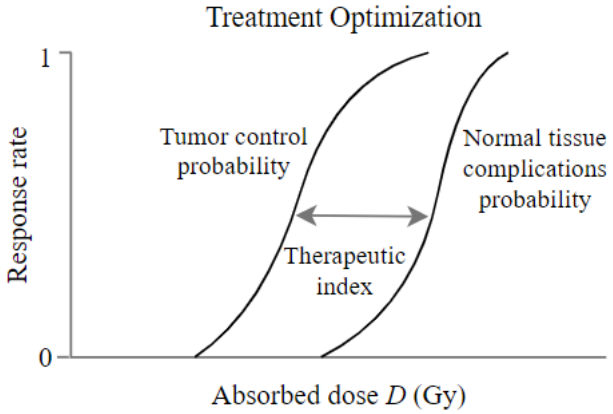

Figure 2.18: TCP and NTCP for EBRT as a function of the absorbed dose. Adapter from: [52]

The main goal in EBRT treatment optimization - and also in RE - is to maximize TCP within acceptable NTCP. The therapeutic index is the greatest at maximum deviation between the TCP and NTCP curves. Treatment optimization is achieved when delivering an absorbed dose at or close to that maximum point.

2.4.4 Radiobiology in Radioembolization

EANM recently reported the pressing need for radiobiology investigations specific to RPTs and RE because the EBRT background knowledge cannot be directly applied [46]. Figure 2.19 depicts the key difference between these therapies, i.e., in EBRT the radiation source is outside the patient's body, whereas in RPTs and RE it is positioned locally. In addition to this inherent difference, EBRT is characterized by a constant radiation quality, short exposure time, high dose-rates and mostly homogeneous irradiation; while RPTs and RE present mixed radiation qualities (due to the radioactive decay modes), time-varying and protracted exposures, low dose-rates and highly non-uniform ADDs [48].

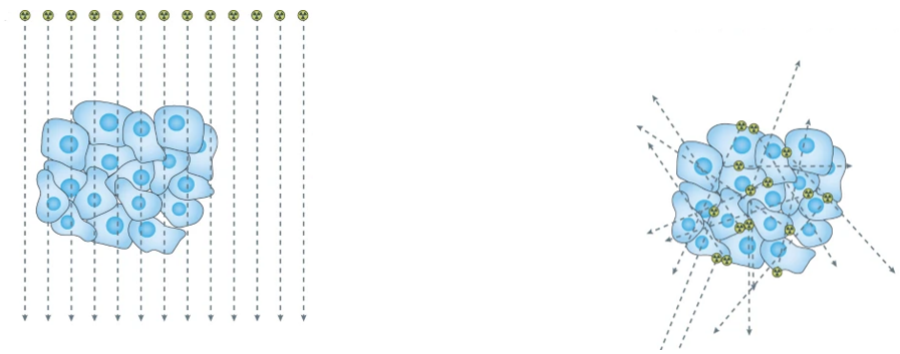

(a) EBRT. (b) RPT and RE.

Figure 2.19: EBRT vs RPT and RE: radiation direction and origin. Adapted from: [40]

Radiobiology is not considered in the treatment planning of most NM therapies. RE forms the exception to this rule, as absorbed dose thresholds in normal liver and tumor are being investigated in recent dosimetry approaches [46]. However, the guidelines are based on a naive uniform ADD within the PTV and NLV. RE treatment planning should not only consider the non-uniform ADD, but also the low dose-rate and damage repair rates. In the next chapter, current investigations on radiobiology quantities in RE are discussed.

Chapter 3

State of the Art

Personalized dosimetry is paramount to optimize the therapeutic index of RE. This work aims to compare the output of two voxel-based dosimetry methods: VSV dosimetry employed in advanced clinics and MC dosimetry considered the gold standard. This chapter presents the state of the art of RE dosimetry. First, a brief description of the liver anatomy and physiology is given. Second, liver epidemiology and current treatment options are listed, putting RE into its clinical context. Third, the recommended procedures for RE treatment planning, delivery and verification are described. Finally, the evolution of RE dosimetry is presented.

3.1 Clinical Background

3.1.1 Anatomy and Physiology of the Liver

The liver is the largest human internal organ, weighting around 2% of the total body [53]. It is divided into a left and a right lobe, and it is positioned in the right upper quadrant of the abdominal cavity, beneath the diaphragm and protected by the rib cage, as illustrated in Figure 3.1. The liver is responsible for many critical functions, including secretion of bile, detoxification, metabolism of bilirubin and nutrients, and storage of blood, minerals and vitamins [54].

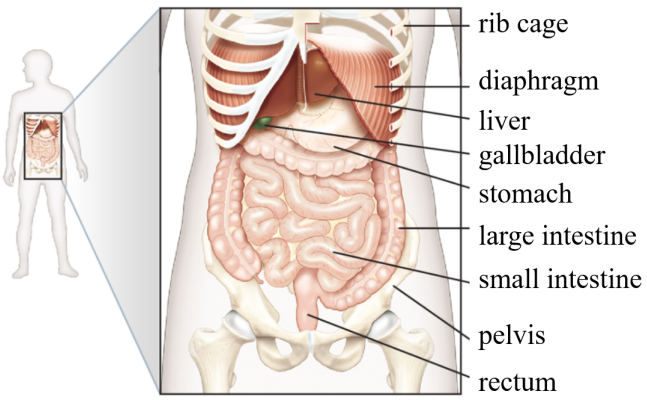

Figure 3.1: Liver position in the abdominal cavity. Adapted from: [55]

Figure 3.2 illustrates liver vascularization. Blood supply to the liver is dual: the portal vein supplies 80% of the blood, coming from the intestine and spleen; and the hepatic artery supplies the remaining 20%, bringing nutrients and oxygen [56]. In the presence of hepatocellular carcinoma (HCC), tumors draw over 80% of their blood supply from the hepatic artery, while normal tissues draw over 80% of their blood supply from the portal vein [2]. Three hepatic veins achieve venous drainage, combining into the inferior vena cava. The intrahepatic biliary tree produces and transports bile to the duodenum and follows the portal vein branches [56].

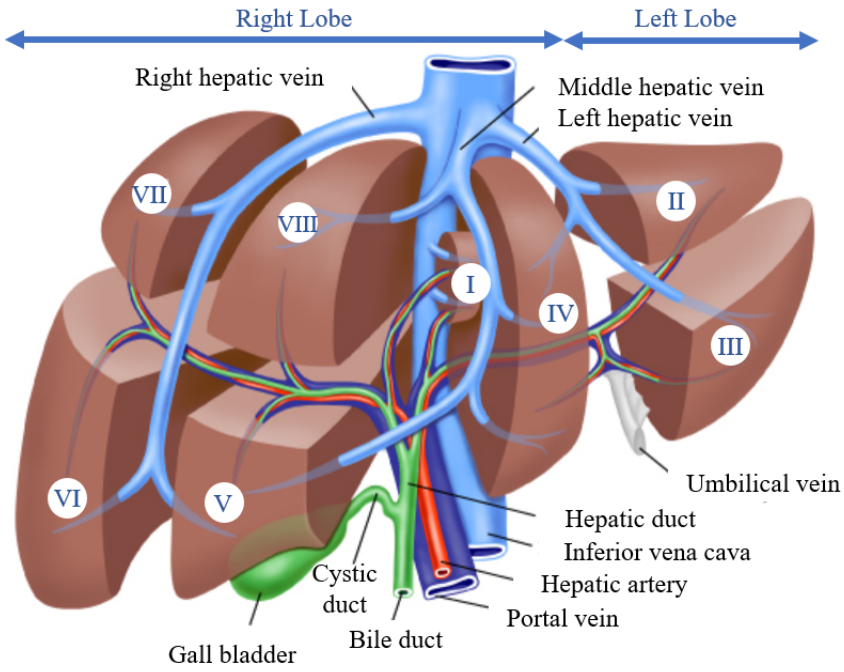

Figure 3.2: Coindaud's liver segments and liver vascularization. Adapted from: [57]

The conventional Couinaud's segmentation divides the liver into eight functional segments according to the vascular branching pattern, as illustrated in Figure 3.2 [58], [59]. Radiologists and surgeons extensively use this segmentation scheme for accurate localization of focal hepatic malignancies [53].

3.1.2 Liver Cancer and Treatment Options

Primary liver cancer was responsible for over 830,000 deaths worldwide in 2020 [1]. In Portugal, 1518 deaths were reported in the same year [60]. Primary liver cancer originates in the liver and includes mostly HCC (75%-85% of cases) and intrahepatic cholangiocarcinoma (CCA) (10%-15% of cases) [1]. Secondary liver malignancies represent the most frequent metastases originating from other cancers types and are actually more common than primary liver cancers [61].

Management of liver cancer is complex as only 10 to 20% of patients are eligible for curative surgeries [2]. The European Association for the Study of the Liver (EASL) recommends the following therapy choice, depending on cancer stage: (1) surgical resection for patients with early-stage tumours[1] and normal liver function, (2) transplantation for unresectable tumours within the Milan criteria[2], (3) radiofrequency ablation for small solitary tumors[3], (4) transarterial chemoembolization (TACE) for unresectable tumors in a intermediate stage[4], and (5) systemic chemotherapy for advanced-stage tumours[5,6][63]. EASL recommends RE, with moderate evidence, in early-stage tumours for bridging to transplantation and in intermediate and advanced tumours as an alternative to TACE and systemic therapy [63]. Currently, data show a good safety profile and local tumour control, but fail to show benefit in patients' overall survival compared to systemic treatment [63]. This work focuses on RE.

3.2 Radioembolization

RE is a form of brachytherapy defined as the administration of MS charged with ^{90}Y into the hepatic artery to internally irradiate tumour cells (Figure 3.3). It is indicated for unresectable liver cancers, both primary and metastatic, or as a neoadjuvant to surgery [7]. RE can target subsegmental, segmental or lobar malignancies by manipulating the catheter position in liver vessels [3].

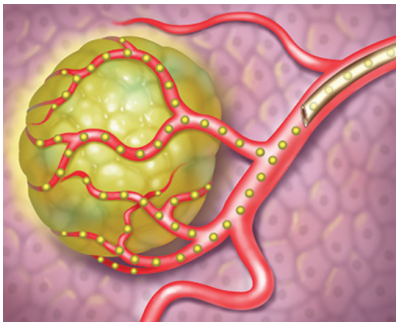

Figure 3.3: Administration of ^{90}Y – MS through the hepatic artery via catheterization. Retrieved from: [64]

The main advantage of RE is its capability to selectively target the PTV with a high absorbed dose while sparing the surrounding NLV with a low absorbed dose [9],

[1] Single tumour smaller than 2 cm in diameter without vascular invasion

[2] Milan criteria: single tumour diameter less than 5 cm; not more than three foci of tumour, each one not exceeding 3 cm; no angioinvasion; no extrahepatic involvement.

[3] Unresectable single tumors smaller than 2-3 cm

[4] Multinodular with preserved liver function

[5] Portal invasion and extrahepatic spread

[6] Note that EBRT (strongly recommended to treat other cancers) does not play a role in the management of liver cancer because it yields a high risk of radiation-induced liver disease [62].

[10]. In HCC, selectivity is possible due to tumoural hypervascularization, preferential arterial flow to HCC in the dual blood supply (>80%), and catheter positioning in the hepatic artery [65]. In liver metastases, hypervascularization may be absent, but local administration can still achieve selectivity [2].

Despite good selectivity of RE, excessive irradiation of NLV causes most complications, which are often avoidable with appropriate treatment planning. In addition, shunting of MS to other organs at risk can lead to severe complications. Shunting to the gastrointestinal tract may cause chronic pain, ulceration, and bleeding; and shunting to the lungs may cause edema, fibrosis, and pneumonitis [7]. RE treatment planning estimates the distribution of MS in the liver and extrahepatic regions, rejecting patients to whom complications are unavoidable for sufficient tumour control.

For eligible patients, RE should be optimized to achieve the maximum therapeutic effect, i.e., sufficient tumour control within acceptable toxicity levels in the normal tissues. The activity of ^{90}Y – MS and the position of the catheter are the only variables that a physician can control. To optimize RE, EANM strongly recommends that the activity of ^{90}Y should: (1) be prescribed based on personalized dosimetry calculations at PTV and organs at risk, and (2) consider the biological response and toxicity in these tissues [6]. Treatment delivery should also be verified with personalized dosimetry calculations. These guidelines are in compliance with the EURATOM directive of February 2018 requiring that for all patients undergoing radiation therapies, including RE, absorbed doses in target and non-target tissues should be individually planned and verified [4]. This section outlines the most recent guidelines for RE treatment planning, delivery, and verification.

3.2.1 Radioembolization Treatment Planning

RE treatment planning is performed 1 to 2 weeks before treatment delivery and aims to assess patient eligibility and optimize the activity of ^{90}Y – MS to be administered. According to EANM guidelines for RE, treatment planning includes three essential steps: (1) hepatic angiography with possible prophylatic embolization of extrahepatic vessels, (2) assessment of pulmonary and gastrointestinal shunts by injection of ^{99m}Tc – MAA followed by scintigraphy, and (3) prescription of the optimum activity of ^{90}Y – MS through dosimetry calculations based on ^{99m}Tc – MAA images [2]. Figure 3.4 summarizes the flow of treatment planning procedure. Each step is described below.

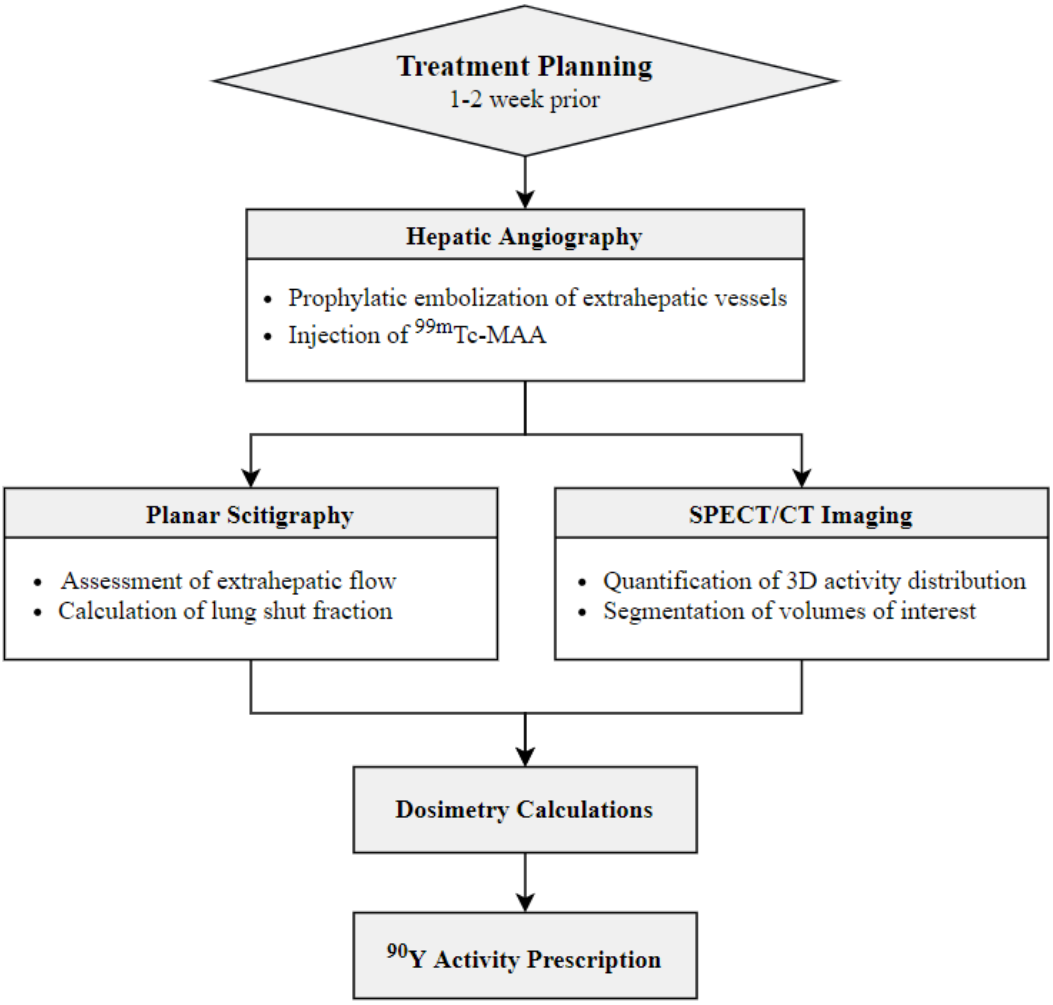

Figure 3.4: RE treatment planning procedure flowchart.

Hepatic angiography aims to assess the hepatic vascularization variants and position the catheter in the direction of the tumor. Prophylactic coil embolization of the gastroduodenal artery is considered to avoid the risk of ^{90}Y-MS reflux to the gastrointestinal tract [2]. During the angiographic procedure, 75-150 MBq of ^{99m}Tc – MAA are injected through the hepatic artery to simulate the *in vivo* distribution of ^{90}Y – MS, within diagnostic radiation exposure levels [2].

Studies have shown that simulations with ^{99m}Tc – MAA accurately estimate the distribution of ^{90}Y – MSs through scintigraphy or SPECT images [66]. However, the distribution of ^{99m}Tc – MAA is not entirely reproducible by the ^{90}Y – MSs on a voxel scale due to many inherent confounding factors [67]. Firstly, a higher activity and a higher number of particles are injected for ^{90}Y – MSs. Secondly, the size of MAA compounds is poorly calibrated, ranging from 10 to 150 μm, while ^{90}Y – MSs are well-calibrated, with a mean size of 25 ± 5 μm [68]. Thirdly, ^{99m}Tc – MAA often dissociates *in vivo*,

facilitating the flow of ^{99m}Tc alone to further locations[7]. Physiological and angiographic factors additionally impact the biokinetics of ^{99m}Tc – MAA and ^{90}Y – MSs daily, including variations in tumour vascularization, tumour size and catheter position [68].

Following the angiographic procedure, a planar scintigraphy image estimates the extrahepatic uptake of ^{99m}Tc – MAA. The lung shunt fraction (LSF) predicts the liver-lung shunt of ^{90}Y – MSs as the ratio of scintigraphy counts in the lungs to the sum of scintigraphy counts in the lungs and liver, as:

$$LSF = \frac{Lung_{\text{counts}}}{Lung_{\text{counts}} + \text{Liver}_{\text{counts}}}. \tag{3.1}$$

Patients with LSF higher than 20%, which cannot be corrected through angiographic techniques, are not eligible for RE because the absorbed dose in lungs would be higher than the toxicity limit of 30 Gy [2], [69]. Prediction of LSF based on a single planar image, without attenuation corrections as performed for reconstruction of SPECT images[8], yields a large overestimation due to a much lower photon attenuation in the lungs compared to that in the abdominal cavity [2]. The geometric average of counts in two planar images, acquired from anterior and posterior views, can partially make up for the absence of attenuation corrections [10].

SPECT/CT images allow to (1) map the 3D activity distribution of ^{99m}Tc – MAA in the liver, predicting the 3D activity distribution of ^{90}Y – MS, and (2) segment VOIs (PTV and NLV). Figure 3.5 gives a cross-sectional view of a typical SPECT/CT image of an RE patient with a color-bar scale for SPECT counts. It is clear that activity is mostly centered in the PTV region, but there is still some activity in the NLV.

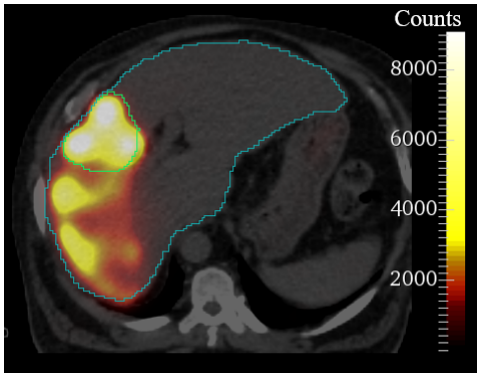

Figure 3.5: SPECT/CT image for patient 6 in RE treatment planning. Outlines of the PTV (green) and NLV (blue). Colorbar scale for SPECT counts.

[7] A short time interval between labelling of MAA with ^{99m}Tc, administration of ^{99m}Tc – MAA and image acquisition minimizes this effect [2].

[8] If the acquired SPECT images include the whole lungs, then the LSF can be estimated based on SPECT counts considering attenuation corrections

The last step of RE treatment planning comprises dosimetry calculations to determine the optimum activity of ^{90}Y – MS, aiming for a sufficient absorbed dose within PTV and the lowest possible absorbed dose within the NLV. RE dosimetry is described in Section 3.3.

3.2.2 Radioembolization Treatment Delivery and Verification

RE treatment delivery and verification procedure resemble the treatment planning scheme with some twists. It also initiates with hepatic angiography to accurately position the catheter in the hepatic artery as decided in treatment planning. Afterwards, the Therasphere® Administration Kit is used to slowly administrate the Therasphere® dose vial content (i.e., the ^{90}Y – MSs), avoiding backflow and providing β^- radiation shielding [7]. The percentage of the vial activity actually delivered to the patient can be calculated based on ion-chamber radiation detector measurements of the radioactive residual waste, R, that remains in the injector circuit after the RE procedure. Measuring radioactive residual waste is relevant not only for treatment verification, but also to predict it for dosimetry in future treatment planning procedures[9].

Following the administration of ^{90}Y – MSs, RE treatment verification comprises the acquisition of PET/CT images to assess the distribution of ^{90}Y – MS and segment the VOIs. PET images are preferred to SPECT images because they provide better spatial resolution, as previously explained in Section 2.2. Dosimetry calculations should be performed for comparison with planning goals and to verify safe and efficient treatment delivery.

3.3 Dosimetry Methods in Radioembolization

The goal of dosimetry in RE treatment planning is to determine a personalized activity of ^{90}Y – MSs that maximizes tumor control and ensures patient safety. This can be accomplished by achieving a sufficient absorbed dose to the PTV that does not yield an absorbed dose to the NLV and lungs above the toxicity limit. The recommended dosimetry thresholds are set for the mean absorbed dose, $\overline{D}$, within these VOIs: $\overline{D}_{\text{PTV}} > 205$ Gy, $\overline{D}_{\text{NLV}} < 60$ Gy, and $\overline{D}_{\text{lungs}} < 30$ Gy [2], [8], [9]. Following treatment delivery, the goal of dosimetry is to verify efficient and safe treatment delivery.

In both treatment stages, the key input variables required to perform personalized dosimetry calculations are: (1) the LSF estimated through planning ^{99m}Tc – MAA scintigraphy images, (2) the activity distribution depicted in planning ^{99m}Tc – MAA SPECT

[9] At the NM-radiopharmacology group at CCU-CF, R is set to 2.7% by default for dosimetry in treatment planning.

images or verification ^{90}Y – MS PET images, (3) the tissue heterogeneity depicted in CT images, (4) the segmentation of VOIs (PTV, NLV), and (5) the anticipated or measured radioactive residual waste, *R*. In addition, radiobiology measurements of the dose-effect relationship within the PTV and NLV should be performed based on dosimetry results. Different dosimetry methods for RE can consider some or all of these variables, including the mono-compartment medical internal radiation dose (MIRD) scheme, multi-compartment macrodosimetry, VSV dosimetry and MC simulations.

Therasphere® manufacturer recommends mono-compartment dosimetry, which only considers an patient-averaged absorbed dose in the whole target liver volume (TLV) [7]. This method does not comply with EURATOM directives and EANM recommendations already presented [2], [4]. Because of that, clinical trials are currently ongoing to shift guidelines to multi-compartment dosimetry, which assumes different (yet uniform) activities within the NLV and PTV. Advanced clinics already employ voxel-based dosimetry methods, such as VSV and MC, which recognize the non-uniform activity distribution depicted in a SPECT or a PET image and, for the latter, the tissue heterogeneity depicted in a CT image[10]. The output of voxel-based dosimetry is a 3D matrix representing an ADD, allowing voxel-based measurements that can take into account dose-effect relationships [10]. Table 3.1 lists RE dosimetry variables that each method does or does not consider.

Table 3.1: Variables of personalized dosimetry considered by each method.

	Dosimetry Variables				
Method	**LSF**	***R***	**Segmentation**	**Activity distribution**	**Tissue heterogeneity**
Mono-comp.	+	+	−	−	−
Multi-comp.	+	+	+	+/−	−
VSV	+	+	+	+	−
MC	+	+	+	+	+

This section describes each dosimetry method and presents the results of the most recent investigations.

3.3.1 Mono-compartment Macrodosimetry

The guidelines of Therasphere® manufacturer suggest to deliver an absorbed dose to the TLV in the range of 80 to 150 Gy, calculated following the mono-compartment MIRD macrodosimetry, as:

$$\overline{D}_{\mathrm{TLV}}[Gy] = \frac{AA[GBq] \times 50 \times (1 - LSF) \times (1 - R)}{m_{\mathrm{TLV}}[kg]}, \tag{3.2}$$

where m_{TLV} is the mass of the TLV derived from the measured volume on CT image [7]. TLV can be a single segment, multiple segments, a lobe or (not ideally) the whole

liver volume (WLV), depending on the catheter position for administration of ^{90}Y – MS. Thus, mono-compartment dosimetry considers a uniform activity distribution in the TLV, does not consider NLV and PTV segmentation and tissue heterogeneity. These naive assumptions limit dosimetry accuracy and gear activity prescription to average patient safety instead of personalized treatment efficacy. The result is tumour under dosage to many patients to avoid complications [70].

The Therasphere® manufacturer provides an online tool - the interactive Dose Ordering Calculator (iDOC) - to assist with calculating and ordering the appropriate activity in a dose vial to achieve the desired $\overline{D}_{\text{TLV}}$, based on Equation 3.2. It also provides treatment scheduling options based on the dose vial assembly time and ^{90}Y decay.

3.3.2 Multi-compartment MIRD Macrodosimetry

Multi-compartment dosimetry is the most simple form of personalised dosimetry. It calculates different absorbed doses to the NLV an PTV by assuming different activity uptakes in these compartments based on planning ^{99m}Tc – MAA SPECT images or verification ^{90}Y PET images. Absorbed doses in the PTV and the NLV are calculated as:

$$\overline{D}_{\text{PTV}}[Gy] = \frac{AA[GBq] \times (1-R) \times 50 \times FU_{\text{PTV}}}{m_{\text{PTV}}[kg]} \tag{3.3}$$

and

$$\overline{D}_{\text{NLV}}[Gy] = \frac{AA[GBq] \times (1-R) \times 50 \times FU_{\text{NLV}}}{m_{\text{NLV}}[kg]}, \tag{3.4}$$

where m_{PTV} and m_{NLV} are respectively the masses of PTV and NLV extracted from CT segmentation and FU_{PTV} and FU_{NLV} are respectively the fractional uptake of activity in the PTV and NLV, defined as:

$$FU_{\text{PTV}} = (1-LSF) \times \left[\frac{TLR \times m_{\text{PTV}}}{TLR \times m_{\text{PTV}} + m_{\text{NLV}}} \right], \tag{3.5}$$

and

$$FU_{\text{NLV}} = (1-LSF) \times \left[\frac{m_{NLV}}{TLR \times m_{\text{PTV}} + m_{\text{NLV}}} \right], \tag{3.6}$$

where TLR is the tumor to liver ratio of image counts.

The main advantage of multi-compartment dosimetry is its simple formulation to balance $\overline{D}_{\text{PTV}}$ and $\overline{D}_{\text{NLV}}$ [10]. A level I clinical trial showed that the prescription of ^{90}Y – MSs activity supported by multi-compartment dosimetry improved patients' median overall survival by 16 months compared to mono-compartment dosimetry [8]. An ongoing global retrospective study is reinforcing the correlation between a high absorbed dose within the PTV that is tolerable within the NLV and patients' overall survival [71]. Despite the promising results, multi-compartment dosimetry assumes a uniform activity distribution and homogeneous tissues within each compartment. Therefore, these

assumptions might still lead to a non-optimal personalized activity prescription for excellent patient safety and treatment efficacy.

3.3.3 Voxel S-values Dosimetry

VSV dosimetry is a simple method for voxel-based dosimetry. ADDs are obtained through the convolution of a VSV kernel and the integrated activity distribution (IAD) obtained from SPECT or PET images, as:

$$ADD[Gy] = \sum VSV \times IAD. \tag{3.7}$$

A VSV kernel describes the ADD per unit of integrated activity from a central source voxel emitting radiation to the surrounding target voxels, in Gy MBq^{-1} s^{-1}, as illustrated in Figure 3.6 [72]. VSV kernels are computed for homogeneous mediums by MC simulation[10]. ADDs allow to compute mean absorbed doses within the NLV and PTV for RE optimization and radiobiology quantities. Overall, VSV dosimetry returns results very fast and is rather simple, motivating its implementation in some advanced clinics [9].

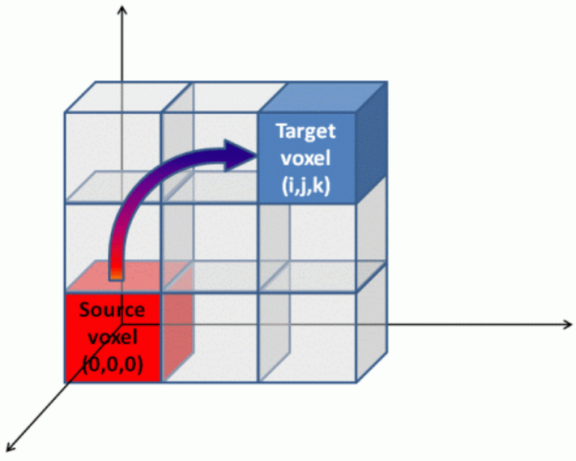

Figure 3.6: Matrix of VSV. A source voxel deposits energy in the surrounding target voxels. Retrieved from: [72]

VSV dosimetry takes another step in the direction of personalized treatment planning by considering a non-uniform activity distribution and allowing voxel-based dosimetry measurements that can take into account dose-effect relationships. However, the assumption of a homogeneous medium limits VSV dosimetry accuracy. Within the NLV and PTV, this approximation may lead only to small dosimetry accuracy losses because the liver is a rather uniform organ and liver tumors are iso-density masses [9], [74], [75].

[10] A database of VSV for standard human tissues is available online for multiple radionuclide sources and voxel dimensions [73].

Larger variations might be seen in the liver interface with surrounding tissues, such as the lungs or bones with significantly different properties.

Multiple VSV methods have been studied to consider tissue heterogeneities [76]–[78]. This method uses a limited number of VSV simulated for multiple tissues and employs them in the convolution operation. Lee *et. al* showed that 20 different VSV yielded similar ADDs to previous MC simulations taking less than 1% of the MC computation time [77]. Despite being fast and considering a limited number of tissue heterogeneities, multiple VSV fail to accurately describe absorbed dose variations in the boundaries of significantly different tissues.

3.3.4 Monte Carlo Dosimetry

MC simulations estimate mathematical functions and mimic real complex systems through random sampling and statistical modeling [79]. Many fields use MC simulations, including risk management, financial engineering, and medical physics. MC methodology has four steps: (1) defining a deterministic model which resembles a real scenario; (2) generating a statistical model to define the behaviour of stochastic variables through a set of probability distribution functions (PDF); (3) repeatedly generating random numbers from the PDFs and collection the outputs; and (4) computing the statistic of interest [79], [80].

MC simulations are considered the gold standard for personalized dosimetry because they closely mimic a patient morphology and the radiation interactions at a microscopic level [10]. In RE dosimetry, a MC simulation receives a CT image to construct a voxelized phantom resembling tissue heterogeneities through a pre-defined conversion of HU to tissue parameters (mass density and chemical composition). SPECT or PET images define the activity distribution of ^{90}Y – MS throughout this phantom [81]. Then, the transport of ^{90}Y radiation is simulated using PDFs associated to the physical interactions in the constructed phantom [82]. The energy deposited in each interaction yields the ADDs that allow computing the mean absorbed doses within the NLV and PTV for RE optimization and verification and radiobiology quantities [83]. Figure 3.7 illustrates the flow of MC simulations in RE.

Popular MC codes used for dosimetry applications are EGS (Electron Gamma Shower), MCNP (Monte Carlo N-Particle), PENELOPE (Penetration and Energy Loss of Positrons and Electrons), GAMOS (Geant4-based Architecture for Medicine-Oriented Simulations), FLUKA (Fluktuierende Kaskade) and TOPAS (Tool for Particle Simulation). In 2004, Jan *et al.* introduced GATE as a MC toolkit tailored to NM [84]. This protocol is trending in RE dosimetry due to its accurate physics modeling based on Geant4 and its user-friendly interface [84], [85].

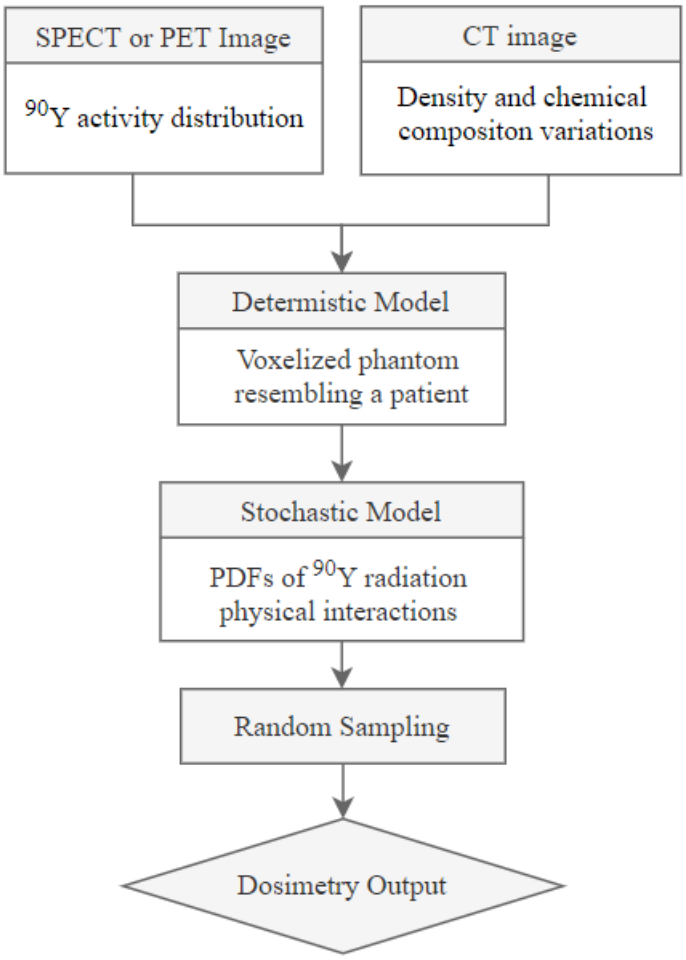

Figure 3.7: Flowchart of MC dosimetry in RE.

MC dosimetry is the only method capable to fully consider tissue heterogeneity within a patient that impact energy deposition in RE. However, long simulation times, high computation power, and complexity levels have discouraged its use in clinical practice of RE[86]. Currently, no clinical trials have been conducted to validate MC dosimetry in RE, and the conducted investigations consist of retrospective clinical studies.

Recent studies investigate the use of MC dosimetry in internal radiation therapies [87]–[91]. In the scope of RE, Hashikin *et al.* concluded that multi-compartment dosimetry methods underestimate the absorbed dose in NLV because they exclude cross-fire at the PTV/NLV boundary [92]. Milano *et al.* recently validated the MC internal dosimetry tool (MCID) for MC-GATE dosimetry in RE applications, using virtual voxelized phantoms to set activity ground truth. Dosimetry outputs from MC-GATE and VSV dosimetry showed good agreement for homogeneous phantoms, but significantly varied after introducing heterogeneity in phantoms [86]. Auditore *et al.* showed that ADDs obtained by means of MC-GAMOS and VSV methods using patient's clinical data generally agreed, except for lung voxels at liver-lung interface, which are significantly affected by liver

irradiation [93].

Currently, the potential of optimizing the administrated activity of ^{90}Y – MS in RE based on MC dosimetry is unvalidated. Retrospective studies can justify investing in MC dosimetry clinical trials if they reveal promising results to increase patient's overall survival. With this in mind, there is the need to further compare dosimetry outputs from multi-compartment, VSV and MC dosimetry using real retrospective clinical data of RE patients.

3.3.5 Radiobiology Quantities in Radioembolization

RE voxel-base dosimetry methods, such as VSV and MC, allow to consider dose-effect relationships for activity prescription. In RE, BED has been employed for this purpose, but its expression has not been agreed on. A popular expression to obtain BED in a voxel k from ADDs can be expressed as:

$$BED_k = D_{\mathrm{k}}\left(1 + \frac{D_{\mathrm{k}} \times T_{\mathrm{rep}}}{T_{\mathrm{rep}} + T_{\mathrm{phys}} \times \alpha/\beta}\right) \tag{3.8}$$

where D_{k} is the absorbed dose in voxel k, T_{rep} and T_{phys} are respectively the half-life for cell repair and ^{90}Y decay and α/β is the radiosensitivity ratio [10], [45]. EUBED describes the ADD within a VOI as:

$$EUBED = -\frac{1}{\alpha} ln\left(\frac{\sum_{n=k}^{N_{\mathrm{V}}} exp(-\alpha BED_k)}{N_{\mathrm{V}}}\right) \tag{3.9}$$

where N_{V} is the number of voxels in the VOI [10].

Currently, there is still a limited number of studies related to the use of radiobiology in RE and the use of these dose-response relationships are still under investigation [91], [94]–[96]. There are no clear guidelines provided by the MS manufacture in how to optimize RE based on BED or EUBED parameters, much less TCP or NTCP curves [10], [46].

3.3.6 In-house State of the Art

Since 2016, the NM-Radiopharmacology reasearch group at CCU-CF has been investigating VSV dosimetry to optimize Therasphere® activity prescription in RE applications based on absorbed doses in the PTV and NLV [97]. In 2018, the group evaluated the predictive value of pre-treatment ^{99m}Tc – MAA SPECT images at a voxel level [98]. Recently, the group adapted the use of DVH and BED measurements from EBRT to RE activity prescription, aiming for personalized treatment planning.

An example of an RE clinical schedule employing VSV dosimetry followed by the group in clinical practice is described below:

Week 1	
Day 1	- Angiography with administration of ^{99m}Tc-MAA, followed by SPECT and CT imaging
Day 2	- LSF calculation
	- Image processing: SPECT reconstruction and co-registration with CT resampling, and cropping)
	- VOIs segmentation
Day 3	- VSV Dosimetry calculations with recommendation of optimum A of ^{90}Y
	- ^{90}Y vial order to the manufacturer
Week 2	
Day 4	- Expected arrival of ^{90}Y vial and quality control measurements
Day 5	- Treatment delivery and measurement of vial R
Day 6	- Image processing (similar to treatment planning)
	- VSV dosimetry and treatment planning quality verification

The group is invested in contributing to the development of accurate and personalized dosimetry in RE applications to increase patients' overall survival. Hence, MC dosimetry represents the logic next step in their research agenda. This work kicks off the investigation of MC dosimetry in RE.

Chapter 4

Materials and Methods

This chapter describes the dataset and methodology followed in this work to (1) assess the accuracy of VSV dosimetry compared to the gold standard MC dosimetry and (2) evaluate the relevance and feasibility of introducing MC dosimetry in the clinical practice to optimize RE and boost patient's overall survival.

4.1 Clinical Dataset

The clinical dataset provided to this work comprises six RE patients retrospectively selected from the database of the NM-Radioparmacology group at CCU-CF. The administrated activity of ^{90}Y – MS, measured radiaoactive residual waste, and estimated LSF were reported for dosimetry purposes. Table 4.1 lists these values and each patient's main diagnoses, including tumor localization.

Table 4.1: Clinical dataset description, including diagnostic and lesion localization, PTV, NLV, administrated activity of ^{90}Y – MS, radiaoactive residual waste, and LSF. (PM - pancreatic metastases)

Patient	Diagnostic	PTV(cm^3)	NLV (cm^3)	*AA* (MBq)	*R*(%)	LSF (%)
1	CCA; right lobe	95	975	1780	2.7	2.6
2	HCC; right lobe	1047	1387	5190	2.7	11
3	PM; right lobe	658	1416	3560	2.7	6.5
4	HCC; left lobe	772	1723	3416	2.7	9.7
5	CCA; segment IV	256	1531	398	2.7	5.5
6	CCA; right lobe	353	2608	4600	3.0	6.2

Planning non-hybrid ^{99m}Tc-MAA SPECT and CT images, and verification hybrid ^{90}Y-MS PET/CT images were also provided to support dosimetry. Image acquisition, processing and segmentation followed by NM physicians and medical physics experts are described below.

4.1.1 Image acquisition

In treatment planning, SPECT images were acquired using the SPECT Philips BrightView system following the administration of ^{99m}Tc – MAA. CT images were acquired afterwards using the CT component of PET/CT Philips Gemini system. In treatment verification, PET/CT images were acquired with PET/CT Philips Gemini system following the administration of ^{90}Y – MS. Table 4.2 summarizes the main characteristics of the two imaging systems: SPECT Philips BrightView and PET/CT Philips Gemini.

Table 4.2: Characteristics of imaging systems employed in RE.

Characteristic	**PET/CT Philips Gemini**	**SPECT Philips BrightView**
PET or SPECT		
Image matrix	144 x 144	128 x 128
Voxel size (mm^3)	4 x 4 x 4	4 x 4 x 4
CT		
Image matrix	512 x 512	-
Voxel size (mm^3)	1.17 x 1.17 x 1	-
kV	120	-

For Patients 1 to 5, images were reconstructed with the OSEM algorithm (iteractions = 3; subsets = 8) and a Butterworth filter was applied (cut off = 2; order = 10). For patient 6, images were reconstructed with the Astonish algorithm and no filters were applied. All clinical images were initially recorded in DICOM format but were only available to this work in NIfTI format for anonymization purposes and to simplify image archiving and processing.

4.1.2 Image Co-registration, Resampling and Cropping

Before imaging acquisition in treatment planning, a NM physician placed five FMs on each patient that allowed for *co-registration* of non-hybrid planning CT and SPECT images. Therefore, the dataset includes six co-registered planning SPECT/CT images and six hybrid verification PET/CT images. Only linear transforms were used to align the image pairs.

A *resampling* operation was applied to obtain the same voxel size for all image modalities: 2.21 x 2.21 x 2.21 mm^3. The voxel size was chosen according to the smallest size of the available VSV kernels [72].

After the resampling process, each patient's images were *cropped* to a smaller box around the abdominal cavity to decrease the time of dosimetry calculations. The cropped images include only a tiny inferior portion of the lungs.

4.1.3 Image Segmentation

A NM physician segmented VOIs for each patient based on CT images, including the WLV, PTV, and NLV. An expansion of five voxels (11.05 mm) was applied to the WLV to ensure that all ^{90}Y – MSs deposited within the liver were covered, avoiding partial volume artifacts. This VOI was called reference WLV (RWLV). All segments were recorded in NIfTI format. Table 4.1 lists the NLV and PTV for each patient.

4.2 Stoichiometric Calibration of HU to Tissue Parameters

Converting CT numbers, in HU, to tissue parameters yields the input for MC-GATE dosimetry simulations that account for tissue heterogeneity. GATE requires a linear calibration of HU to mass density and a discrete calibration of HU to chemical composition. Such calibrations should be provided to GATE in two separate files: *DensitiesTable.db* and *MaterialsTable.db*. When an MC-GATE dosimetry simulation is initialized, the code automatically assigns the adequate tissue parameters to each voxel in a CT image, generating a geometry that mimics patient-specific tissue heterogeneity.

HU are scanner-dependent due to variations in the X-ray spectral energy function, effective X-ray energy, detector energy, scanner diameter, and image matrix size. Therefore, it is mandatory to obtain a calibration specific to the in-house CT scanner and clinical scanning protocol. This section describes the methodology followed to (1) define a stoichiometric calibration of HU to tissue parameters for the CT component of the in-house PET/CT Philips Gemini scanner, using 120 kV and 195 mAs as x-ray tube parameters and an image slice thickness of 1 mm; and (2) generate GATE's input files based on the obtained calibration.

Developed code available at: https://github.com/mariainesribeiro/MasterThesis/tree/main/Stoichiometric_Calibration_of_HU

4.2.1 Parametrizing a CT Scanner with Tissue Substitutes

CT imaging systems are described in section 2.2. HU in CT images relate photon attenuation in a local tissue to that in water, as expressed in Equation 2.8. The mean linear attenuation coefficient varies with the tissue's mass density and chemical composition, following:

$$\overline{\mu} = \rho N_{\mathrm{A}} \sum_{i=1}^{n} \left(\frac{w_i}{A_i} \times \sigma_{\mathrm{i}}^{\mathrm{T}} \right), \tag{4.1}$$

where N_A is the Avogadro's constant, ρ is the tissue's mass density, and w_i, A_i, and σ_i^T are weight, atomic mass, and total cross-section of each chemical element i [99]. Hence, HU are intrinsically related to the tissue parameters required to perform MC-GATE dosimetry simulations.

Each element's total cross-section is unknown because the X-ray spectral energy function of the CT scanner is undefined. In the diagnostic X-ray energy range, the dominant physical interactions between radiation and patient's tissues are only three: PEE, CS, and RS. The empirical formula presented by Rutherford *et al.* [100] gives a good approximation of $\overline{\mu}$, as follows:

$$\overline{\mu} = \rho N_A \sum_{i=1}^{n} \frac{w_i}{A_i} \left(Z_i \overline{K}^{KN} + Z_i^{2.86} \overline{K}^{sca} + Z_i^{4.62} \overline{K}^{ph} \right), \tag{4.2}$$

where the coefficients $\overline{K}^{KN}$, $\overline{K}^{sca}$, and $\overline{K}^{ph}$ include the energy and scanner dependence of each possible physical interaction. For any tissue attenuation relative to water, we get:

$$\frac{\overline{\mu}}{\overline{\mu}_{H_2O}} = \frac{\overline{\rho}}{\overline{\rho}_{H_2O}} \frac{\sum_{i=1}^{n} (w_i/(A_i))(Z_i + Z_i^{2.86} k_1 + Z_i^4 .62 k_2)}{(w_H/(A_H))(1 + k_1 + k_2) + (w_O/(A_O))(8 + 8^{2.86} k_1 + 8^{4.62} k_2)} \tag{4.3}$$

with

$$k_1 = \frac{\overline{K}^{sca}}{\overline{K}^{KN}}, \tag{4.4}$$

and

$$k_2 = \frac{\overline{K}^{ph}}{\overline{K}^{KN}}. \tag{4.5}$$

Thus, only k_1 and k_2 must be fitted to parametrize a CT scanner response to tissue parameters due to the HU dependence on $\frac{\overline{\mu}}{\overline{\mu}_{H_2O}}$ [99].

Schneider *et al.* [99] proposed a stoichiometric calibration by (1) scanning a set of tissue substitutes (TS) with known mass density and chemical composition and (2) measuring their respective HU in the output CT image. The dependence of the photon attenuation as a function of the TS's parameters is defined by parametrizing k_1 and k_2, carrying out a least-square fit of the measured HU to the calculated HU according to equations 2.8 and 4.3, i.e., by minimizing:

$$\sum_{n=1}^{N} \left[\left(\frac{\overline{\mu}}{\overline{\mu}_{H_2O}} (k_1, k_2) \right)_n - \left(\frac{HU_{meas}}{1000} + 1 \right)_n \right]^2 \tag{4.6}$$

In this work, a CATPHAN 604 phantom was used to support this fit for the CT component of PET/CT Philips Gemini scanner. The phantom includes nine different TS: air, polymethylpentene (PMP), low-density polyethylene (LDPE), polystyrene, acrylic, bone 20%, bone 50%, delrin, and teflon (Figure 4.1a). The composition of TS influences the CT calibration, and hence should be selected with caution [101]. In this work, teflon

($[C_2F_4]_n$) was discarded because it contains fluorine, which is absent in human tissues. Table 4.3 lists the mass density and chemical composition of the remaining eight TS in the CATPHAN 604 phantom.

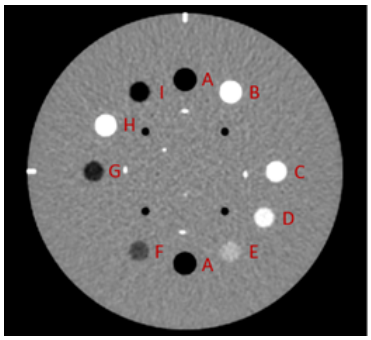

(a) A: Air; B: Teflon; C: Delrin; D: Bone20%; E: Acrylic; F: Polystyrene; G: LDPE, H: Bone50% and I: PMP.

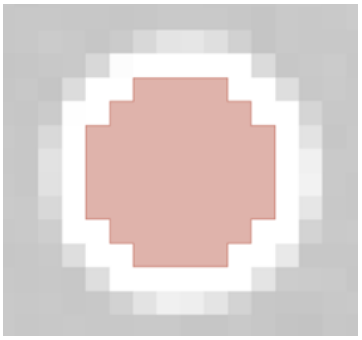

(b) Bone50% segmentation drawn with *3D Slicer*©.

Figure 4.1: CATPHAN 604 cross-sectional view and segmentation of TS.

Table 4.3: Chemical composition and mass density of the eight TS included in CATPHAN 604 phantom.

TS	**Elemental weight (%)**							ρ **(g/cm^3)**
	H	**C**	**N**	**O**	**P**	**Ar**	**Ca**	
Air	-	-	78.00	21.00	-	1.00	-	0.0013
PMP	14.37	85.63	-	-	-	-	-	0.83
LDPE	14.37	85.63	-	-	-	-	-	0.92
Polystyrene	7.74	92.26	-	-	-	-	-	1.03
Acrylic	8.05	59.99	-	31.96	-	-	-	1.18
Bone20%	6.00	51.00	6.00	30.00	3.00	-	6.00	1.14
Bone50%	4.00	35.00	6.00	34.00	6.00	-	14.00	1.40
Delrin	6.71	40.00	-	53.28	-	-	-	1.42

The CATPHAN 604 phantom was scanned with the CT protocol employed to acquire RE patients' images: 120 kV and 195 mAs as x-ray tube parameters, respectively, and 1 mm as image slice thickness. Afterward, eight cylindrical VOIs were segmented using the *3D Slicer*© software. Only the voxels entirely inside the TS region were selected, giving it a margin to avoid partial volume artifacts (see white voxels in the example of Figure 4.1b). The mean HU in each ROI was measured and used to fit k_1 and k_2. Finally, empirical HU of each TS were calculated according to equations 2.8 and 4.3 and using the fitted parameters.

4.2.2 Converting Hounsfield Units to Tissue Parameters

The two-step method suggested by Kanematsu *et al.* [102] was used to convert HU to mass density and mass density to chemical composition. The authors sorted standard human tissues from the most recent compilation of International Commission on Radiological Protection (ICRP Publication 110 [103]) into groups according to their mass density and defined 11 representative tissues (RT) by finding the mass-weighted average of tissues parameters per group. Table 4.4 lists the reference RT's parameters.

Table 4.4: Chemical composition and mass density of the 11 RT by [102].

RT	Elemental Weight (%)													ρ (g/cm^3)
	H	C	N	O	Na	Mg	P	S	Cl	Ar	K	Ca	Fe	
Air	-	0.01	75.52	23.17	-	-	-	-	-	1.30	-	-	-	0.00
Lung	10.30	10.70	3.20	74.60	0.20	-	0.20	0.30	0.30	-	0.20	-	-	0.38
Extra lung	10.30	10.70	3.20	74.60	0.20	-	0.20	0.30	0.30	-	0.20	-	-	0.80
Fat	11.96	76.87	-	11.17	-	-	-	-	-	-	-	-	-	0.90
Adipose/Marrow	11.40	58.91	0.75	28.64	0.10	-	-	0.10	0.10	-	-	-	-	0.95
Muscle/General	10.25	14.59	3.21	70.85	0.11	-	0.21	0.27	0.13	-	0.36	0.02	-	1.05
Miscellaneous	9.94	20.92	3.85	63.72	0.22	-	0.43	0.27	0.29	-	0.09	0.26	0.01	1.09
Heavy Spongiosa	9.32	39.14	2.21	41.79	0.19	-	2.34	0.29	0.13	-	0.04	4.53	-	1.14
Mineral Bone	3.60	15.90	4.20	44.80	0.30	0.20	9.40	0.30	-	-	-	21.30	-	1.92
Tooth	2.20	9.50	2.90	42.10	-	0.70	13.70	-	-	-	-	28.90	-	2.75
Hydroxyapatite	0.20	-	-	41.41	-	-	18.50	-	-	-	-	39.89	-	3.16

Note that the *Muscle/ General* RT represents soft tissues, including the liver. The 11 RT were then used to interpolate tissue parameters through a poly-line calibration. This section explains how the final GATE calibration was achieved for the in-house PET/CT Philips Gemini scanner according to the method proposed by Kanematsu *et al.*.

4.2.2.1 Converting Hounsfield units to mass density

GATE requires two-dimensional points for the linear calibration of HU to mass density, i.e. (HU, ρ). This collection of points allows GATE to define a poly-line calibration between every two consecutive points. In this work, HU of each RT in Table 4.4 were computed according to Equations 2.8 and 4.3 and using the fitted k_1 and k_2 values for PET/CT Philips Gemini scanner. Then, calculated HU and mass density of RTs represented GATE's input points for the linear calibration of HU to mass density.

4.2.2.2 Converting mass density to chemical composition

GATE requires a discrete characterization of HU to chemical composition. In Kanematsu *et al.* [102] calibration, an arbitrary tissue of mass density ρ can be regarded as a binary mixture of consecutive RT 1 and RT 2, where $\rho_1 < \rho < \rho_2$. Each elemental weight w_i of a tissue composition is then defined linearly by interpolation between those of the adjacent RT, through:

$$w_i = \frac{\rho_2 - \rho}{\rho_2 - \rho_1} w_{1,i} + \frac{\rho - \rho_2}{\rho_2 - \rho_1} w_{2,i}. \tag{4.7}$$

To transform this continuous calibration into a discrete calibration, the HU range was segmented into bins of constant chemical composition according to the RT density poly-line. First, the chemical composition of each bin was defined to that of the respective RT. Then, each bin's HU upper and lower limits were calculated as the mean value of two consecutive RT, except between air (HU = -999) and lung (HU = -620). Air has a standard density of around 0.001 g/cm^3, varying with atmospheric conditions, while lung tissues have yielded HU as low as -900 [104]. Therefore, a smaller upper HU limit was assumed to the air RT, interpolated from the poly-line at ρ = 0.1 g/cm^3.

Vanderstraenten *et al.* demonstrated the relevance of multiple bins in the HU range of bone tissues to accomplish dosimetry accuracy[1] [39]. Because of that, the HU bin from heavy spongiosa to mineral bone was segmented, adding eight intermediate bins

[1] The elemental weights of hydrogen and calcium vary significantly between skeletal tissues. Hydrogen and calcium have the most significant impact on physical cross-sections of particles' interactions due to their high electron density and high atomic number, respectively.

with equal width[2]. The elemental weight values in each additional bin were obtained according to the poly-line density calibration through equation 4.7.

4.3 Tissue heterogeneity within the NLV and PTV

The key difference between MC and VSV dosimetry is that the former considers tissue heterogeneity based on each patient's density distributions, including heterogeneity within each organ or tumor, whereas the latter treats each organ or tumor as being homogeneous. Thus, the level of tissue heterogeneity predicts the variation between MC- and VSV-ADDs. As ADDs are the most relevant within the NLV and PTV to RE optimization in clinical practice, tissue heterogeneity was investigated within these VOIs.

Each voxel in patients' CT images was converted to mass density and assigned to a chemical composition bin according to the HU calibration previously obtained. Then, the statistical distribution of mass density and the percentage of voxels assigned to each bin within each patient's NLV and PTV were reported.

Developed code available at: https://github.com/mariainesribeiro/MasterThesis/tree/main/Quantification_of_Tissue_Heterogeneity

4.4 Computation of Absorbed Dose Distributions

This section describes the methodology to compute VSV- and MC-ADDs in RE scope. In this work, 12 ADDs were computed by each dosimetry method, including planning and verification ADDs for six patients.

Developed code available at: https://github.com/mariainesribeiro/MasterThesis/tree/main/Dosimetry_Calculations

4.4.1 Voxel S-values dosimetry

Figure 4.2 illustrates the implemented algorithm for VSV dosimetry. The algorithm steps are described below.

[2]In practice, the intermediate bins between heavy spongiosa and mineral bone do not add useful information to the HU-density calibration. In other words, the intermediate RTs are already in the continuous poly-line and only improve the discrete chemical composition-HU calibration by decreasing the step variation of elemental weights between two consecutive bins in the HU range of skeletal tissues.

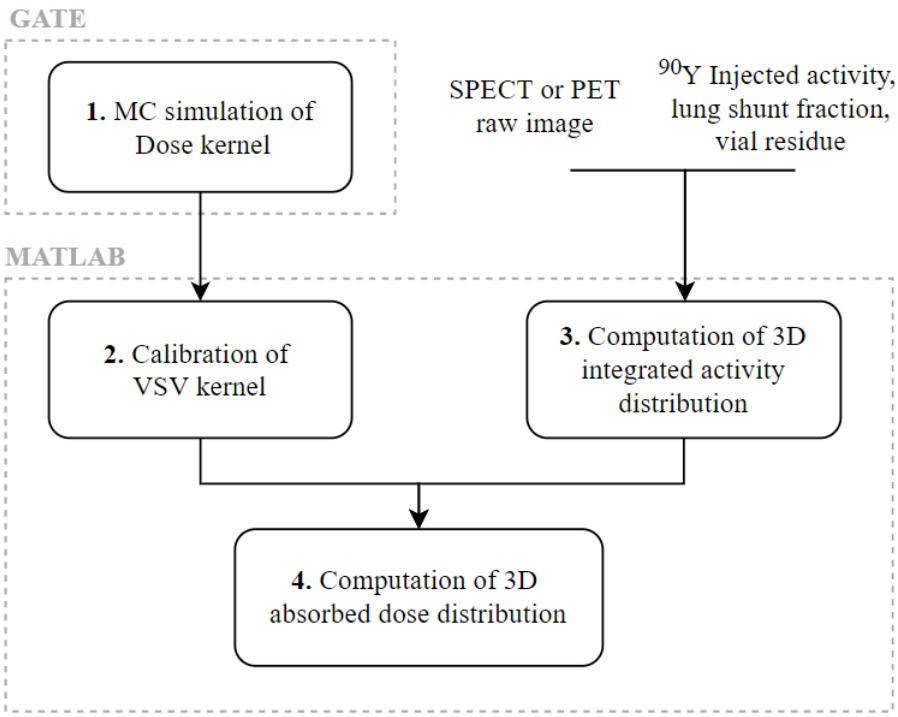

Figure 4.2: Diagram of the VSV dosimetry algorithm for the computation of 3D ADD based on either planning ^{99m}Tc – MAA SPECT or verification ^{90}Y – MS PET images.

STEP 1: MC simulation of a general absorbed dose kernel for ^{90}Y. GATE simulated an ADD, in Gy, for a central source voxel of ^{90}Y emitting isotropically in a general soft tissue medium. The ADD was scored in a 3D grid of 11x11x11 cubic voxels of 2.21 mm edge[3]. This step is explained in detail in section 4.4.3. The absorbed dose kernel was simulated only once, and used for all patients. GATE's output for the absorbed dose kernel simulation is proportional to the number of simulated primary particles, N_{PP}, i.e., the total simulated activity.

STEP 2: Calibration of a general VSV kernel for ^{90}Y. To obtain a VSV kernel, in mGy.MBq^{-1}.s^{-1}, a linear calibration was applied to GATE's output for the absorbed dose kernel simulation:

$$VSV\,[\text{mGy.MBq}^{-1}.\text{s}^{-1}] \;=\; D\;kernel \times \frac{10^3}{N_{PP}/10^6}. \tag{4.8}$$

STEP 3: Calculation of the patient-specific integrated activity distribution (IAD) from planning ^{99m}Tc – MAA SPECT or verification ^{90}Y – MS PET images. Planning SPECT images predict ^{90}Y – MS distribution in tissues by counting ^{99m}Tc radioactive

[3]In all directions, the minimum distance from the centre voxel to the furthest voxel included in the absorbed dose kernel is 11.05 mm, which is greater than the range of ^{90}Y β-radiation in soft tissues.

emissions in a 3D grid, while verification PET images actually depict ^{90}Y – MS distribution in tissues by counting ^{90}Y radioactive emissions in a 3D grid. In this work, both SPECT and PET raw images were used to calculate patient-specific IAD, in MBq.s, for ^{90}Y radioactive decay and were scaled according to the values of administrated activity within the RWLV, radioactive residual waste and LSF through a linear calibration:

$$IAD\,[\text{MBq.s}] = Raw\ image \times \frac{AA \times (1-R) \times (1-LSF) \times \lambda_t}{C_{RWLV}} \tag{4.9}$$

where C_{RWLV} is the sum of SPECT or PET counts within the RWLV, and λ_t is a time integral factor for ^{90}Y activity, calculated as:

$$\lambda_t = \int_0^\infty \exp\left(-\frac{\ln 2}{t_{1/2}} \times t\right) dt \tag{4.10}$$

STEP 4: Computation of patient-specific ADD. Convolution of the general VSV kernel and patient-specific IAD yields the final ADD, in Gy, as:

$$ADD\,[\text{Gy}] = \sum VSV \times IAD \times 10^3. \tag{4.11}$$

4.4.2 Monte Carlo dosimetry

Figure 4.3 illustrates the implemented algorithm for MC-GATE dosimetry. The algorithm steps are described below.

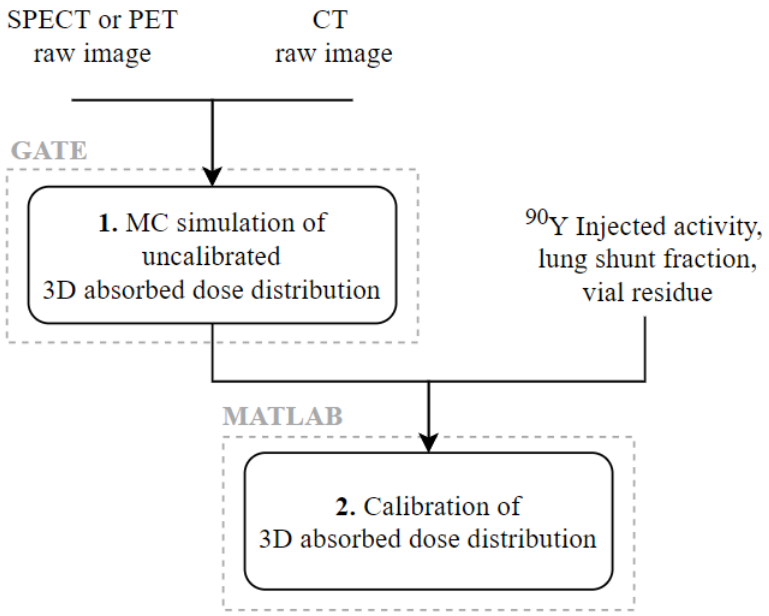

Figure 4.3: Diagram of the MC dosimetry algorithm for the computation of 3D absorbed dose distribution based on either planning ^{99m}Tc – MAA SPECT or verification ^{90}Y – MS PET images.

STEP 1: MC simulation of a patient-specific uncalibrated ADD. GATE simulated uncalibrated ADDs based on each patient's planning ^{99m}Tc – MAA SPECT/CT and verification ^{90}Y – MS PET/CT images, considering ^{90}Y radioactive decay in both cases. This step is explained in detail in section 4.4.3. GATE's output ADD is again proportional to the number of simulated primary particles, N_{PP}, and requires calibration.

STEP 2: Calibration of GATE's output ADD. The following linear calibration was applied to calibrate GATE's output ADD for ^{90}Y radioactive decay and according to values of administrated activity within the RWLV, residual waste and *LSF*:

$$ADD\ [\mathrm{Gy}] = GATE's\ output \times \frac{C_{box} \times AA \times (1-R) \times (1-LSF) \times \lambda_t}{C_{RWLV} \times N_{\mathrm{PP}}} \tag{4.12}$$

where C_{box} are the counts sum within the box volume of the raw SPECT or PET image.

4.4.3 Monte Carlo Simulations with GATE

In this work, two types of MC-GATE dosimetry simulations were developed:

1. **For VSV dosimetry:** GATE simulated a *absorbed dose kernel*, in Gy, for a central source voxel of ^{90}Y emitting isotropically in a soft tissue medium, and scored in a 3D grid of 11x11x11 cubic voxels of 2.21 mm edge. The absorbed dose kernel was simulated only once to compute a VSV kernel used in VSV dosimetry for all RE patients. The simulation set-up was configured to resemble the conditions employed for the reference VSV kernel [72].
   Full GATE script available at: https://github.com/mariainesribeiro/MasterThesis/blob/main/Dosimetry_Calculations/VoxelSvalues/GATEscript_VSVdosimetry.mac

2. **For full MC dosimetry:** GATE simulated *uncalibrated ADDs*, in Gy, scored in a 3D grid with voxels of 2.21 mm edge, according to patient-specific planning SPECT/CT or verification PET/CT images. This simulation was performed 12 times: one for each patient and procedure (i.e., treatment planning and verification).
   Full GATE script available at: https://github.com/mariainesribeiro/MasterThesis/blob/main/Dosimetry_Calculations/MonteCarlo/GATEscript_MCdosimetry.mac

The architecture of each MC-GATE dosimetry simulation includes six key steps: (1) geometry definition, (2) physics set up, (3) output selection, (4) initialization, (5) source definition, and (6) acquisition start. This section describes the configuration of these key steps for the two types of MC-GATE dosimetry simulations developed in this work. Software installation and hardware specifications are also described.

4.4.3.1 GATE Installation and Hardware Specifications

OpenGATE Collaboration provides Virtual GATE (vGate) as a complete virtual machine running on a Ubuntu operating system that includes GATE, GEANT4 and additional packages for data processing. In this work, vGate v9.0 was installed, including GATE 9.0 and GEANT4 10.06.1, and it was launched from VirtualBox.

A personal Windows laptop hosted the virtual machine. The laptop's computational power limited the virtual machine's specifications, which in turn limited MC simulations speed. Table 4.5 lists the specifications of the personal laptop and vGate.

Table 4.5: Specifications of personal laptop and vGATE employed in this work.

Specification	**Personal Laptop**	**vGATE**
Operating Sytem	Windows 10	Ubuntu LTS 10.04
Base memory	16 GB	11300 MB
Processor	Intel(R) Core(TM) i7-8550UCPU @ 1.80GHz 1.99 GHz	4 CPU

4.4.3.2 Geometry Definition

In MC-GATE dosimetry simulations, radiation particles are tracked through geometric volumes. Each volume is characterized by shape, size, position, and material parameters, including mass density and chemical composition. Material parameters influence the calculation of physical cross-sections and hence can markedly affect dosimetry calculations. This is how MC-GATE dosimetry simulations account for tissue heterogeneity.

GATE geometry is defined as a tree structure of volumes: the *world* volume is the base and all user-defined volumes are defined as its *daughters*. For both simulation types in this work, the *world* was set to a 1 meter edge cube of air material, as:

```
/gate/world/setMaterial                                    Air
/gate/world/geometry/setXLength                            1 m
/gate/world/geometry/setYLength                            1 m
/gate/world/geometry/setZLength                            1 m
```

Daughter volumes were defined according to the simulation type:

1. **Absorbed dose kernel simulation:** A homogeneous cubic box made of a soft tissue material represents the absorbed dose kernel simulation geometry. The box size was set to 50x50x50 cm^3, comprising a volume beyond the kernel matrix (of 11x11x11 cubic voxels of 2.21mm edge) to allow for particle back-scattering. The soft tissue

material was defined according to Cristy and Eckerman *et al.* [105], described in Table 4.6.

Table 4.6: Chemical composition and mass density of soft tissue material defined for absorbed dose kernel simulation. Retrieved from: [105]

Element	**Percent by weight (%)**
H	10.454
C	22.663
N	2.490
O	63.525
Na	0.112
Mg	0.013
Si	0.030
P	0.134
S	0.204
Cl	0.133
K	0.208
Ca	0.024
Fe	0.005
Zn	0.003
Rb	0.001
Zr	0.001
Mass density	1.04 g/cm^3

2. **Uncalibrated ADD simulation:** A *voxelized geometry* was set to describe tissue heterogeneity based on patient-specific CT images. First, the algorithm *ImageNestedParametrisedVolume* was inserted to track particles from voxel to voxel. Second, CT images in MetaImage format were provided as input to GATE and placed at the isocenter of the simulation. Third, GATE automatically converted each voxel HU to material parameters according to two input calibration files with the required data, as explained in section 4.2:

   - *DensitiesTable.db*: linearly calibrates HU to mass density (g/cm^3);
   - *MaterialsTable.db*: segments the HU range into materials of constant chemical compositions.

   Finally, GATE creates a single material for each HU range with densities differing less than a tolerance value, assigning it to the correct chemical composition, and stores them in a database.

   Command lines to generate voxelized geometry:

```
# VOXELLIZED GEOMETRY
/gate/world/daughters/name                                  patient
/gate/world/daughters/insert        ImageNestedParametrisedVolume
/gate/patient/geometry/setImage                  [CTfilename].mhd
/gate/geometry/setMaterialDatabase                 HUmaterials.db
/gate/patient/geometry/setHUToMaterialFile             HU2mat.txt
/gate/patient/geometry/TranslateTheImageAtThisIsoCenter    0 0 0 m

# HU CALIBRATION
/gate/HounsfieldMaterialGenerator/SetMaterialTable            ...
                                                MaterialsTable.txt
/gate/HounsfieldMaterialGenerator/SetDensityTable              ...
                                                DensitiesTable.txt
/gate/HounsfieldMaterialGenerator/SetDensityTolerance  0.01 g/cm3
/gate/HounsfieldMaterialGenerator/SetOutputMaterialFilename    ...
                                                  HUmaterials.db
/gate/HounsfieldMaterialGenerator/SetOutputHUMaterialFilename  ...
                                                      HU2mat.txt
/gate/HounsfieldMaterialGenerator/Generate
```

4.4.3.3 Physics Set up

In MC-GATE dosimetry simulations, all physical interactions between a radiation particle and a volume have to be defined. GATE uses well-validated and accurate Geant4 models to list all physical interactions. In this work and for both types of simulations, the *EM Opt3* list was set to describe electromagnetic interactions of photons, electrons and positrons, ranging from 0.1 keV to 10 GeV:

```
/gate/physics/addPhysicsList                          emstandard_opt3
/gate/physics/setEMin                                        0.1 keV
/gate/physics/setEMax                                         10 GeV
```

For each particle type, the following physical interactions are considered in the *EM Opt3* list:

- **Photons:** pair production, Compton and Rayleigh scattering, and photoeletric effect;
- **Electrons and positrons:** Coulomb scattering, Bremsstrahlung, ionization, and positron annihilation.

GATE physics can be further customized by defining particle's production thresholds, special cuts, and step limiters. These parameters can reduce the simulation time, which is very important for the feasibility of MC dosimetry in the clinical practice schedule. Nevertheless, they should be defined carefully to yield a minimum impact in the

dosimetry output and best resemble a real situation. In this work, physics customization parameters were set equally for both types of simulation and are described below:

- **Production thresholds:** Define the energy level bellow which no secondary particles are generated in a given volume. This threshold should be defined as a cut-off range for photons, electrons, and positrons, which GATE internally converts to an energy for individual materials. In this work, the cut-off range was defined to be equivalent to 10 keV, for all particle types.
  Command line:

```
/gate/physics/[ParticleType]/SetCutInRegion   [VolumeName] [range]
```

- **Particle minimum kinetic energy:** Stops a particle that has less energy than the pre-defined *minimum kinetic energy*. When a particle is stopped, the energy is deposited locally. Ideally, the track-length of a stopped particle is shorter than the voxel size of ADDs to ensure dosimetry accuracy. Appendix A describes an investigation conducted as part of this work on the mean track-length of electrons and photons with varying energy in three different materials: lungs, soft tissue and compact bone. The goal was to define the maximum particle energy that would not allow it to escape the voxel where it was generated. In other words, the particle would deposit its energy in the same voxel where it was generated even if it was not stopped. According to the obtained results, *minimum kinetic energy* was set to 20 keV for electrons and 10 keV for photons.
  Command lines:

```
/gate/physics/SetMinKineticEnergyInRegion    [VolumeName] [Energy]
/gate/physics/ActivateSpecialCuts                      [ParticleType]
```

- **Particle maximum step size:** Defines the maximum distance between two consecutive particle interactions in a particle track within a geometry volume. For ^{90}Y radiation, the electron step should be limited to simulate more accurately the non-linear electron track, but a too small electron step significantly increases the computational cost of the simulation. Papadimitroulas et al. investigated the optimal electron step limiter value for multiple isotopes, based on the electron energy and the materials' stopping power [106]. The group defined the electron step limiter for ^{90}Y radioactivity as 0.11 mm for a water material. In this work, the electron's *maximum step size* was set to 0.11 mm for all materials as it is defined to an entire geometry volume instead of a specific material.
  Command line:

```
/gate/physics/SetMaxStepSizeInRegion           [VolumeName] [step]
/gate/physics/ActivateStepLimiter                    [ParticleType]
```

4.4.3.4 Output Actors

The *SimulationStatisticActor* was activated to return the number of simulated primary particles, the simulation time and speed in an ASCII file, following:

```
/gate/actor/addActor              SimulationStatisticActor [ActorName]
/gate/actor/[ActorName]/save                      output/[Filename].txt
```

The *DoseActor* was activated to generate 3D images of dosimetry measurements, in MetaImage format, according to the physical interactions that a particle undergoes as it is tracked through the pre-defined geometry. For spatial configuration, the *DoseActor* was attached to the *daughter* volume and placed at the isocenter, the voxel size was set to 2.21 mm, and the matrix size was set according to the simulation type:

1. **Absorbed dose kernel simulation:** The matrix size was set to 11x11x11 cubic voxels;
2. **Uncalibrated ADDs simulation:** The matrix size was set to the size of the cropped input SPECT/CT or PET/CT images[4]

In addition, *DoseActor* can be defined by the *HitType* and *DoseAlgorithm* parameters. *HitType* defines the level of a particle step where energy is deposited. In this work, *HitType* was set to *random*, i.e., energy is randomly distributed from the beginning of a particle step to its end. *DoseAlgorithm* defines how dosimetry measurements are computed. In this work, *DoseAlgorithm* was set to *MassWeighting*, so that dosimetry measurements considered voxels' mass.

The following commands built *DoseActor* and saved its output in the MetaImage format:

```
/gate/actor/addActor                              DoseActor [ActorName]
/gate/actor/[ActorName]/attachTo                          [VolumeName]
/gate/actor/[ActorName]/stepHitType                               random
/gate/actor/[ActorName]/setVoxelSize            2.21 2.21 2.21   mm
/gate/actor/[ActorName]/setPosition                      0. 0. 0. cm
/gate/actor/[ActorName]/setResolution                     [X] [Y] [Z]
/gate/actor/[ActorName]/setDoseAlgorithm                MassWeighting
/gate/actor/[ActorName]/save                           [Filename].mhd
```

The 3D dosimetry measurements calculated and returned by *DoseActor* are described bellow:

- **Deposited energy distribution in MeV:** Maps the sum of deposited energy within a volume as radiation particles undergo physical interactions within a geometry. The

[4]The input SPECT or PET images used in VSV and MC-GATE dosimetry are the same, i.e., they are cropped around the liver.

deposited energy E_{k} in each voxel k is calculated as:

$$E_k = \sum_{k=1}^{N_{\mathrm{PP}}} e_{k,i} \tag{4.13}$$

where $e_{\mathrm{k,i}}$ is the energy deposited by an independent primary particles i in voxel k.
Command line to enable output:

```
/gate/actor/[ActorName]/enableEdep                    true
```

- **Squared deposited energy distribution in MeV^2:** Maps the squared deposited energy within a volume, as:

$$E_k^2 = \sum_{k=1}^{N_{\mathrm{PP}}} {e_{k,i}}^2 \tag{4.14}$$

Command line to enable output:

```
/gate/actor/[ActorName]/enableSquaredEdep             true
```

- **ADD in Gy:** Converts the deposited energy distribution to absorbed dose. The absorbed dose in a voxel k is computed through the *MassWeighting* algorithm, following:

$$D_k = \frac{\sum_{i=k}^{N_{\mathrm{PP}}} e_{k,i}}{m_k} \tag{4.15}$$

where m_k is the mass in voxel k according to the HU calibration.
Command line to enable output:

```
/gate/actor/[ActorName]/enableDose                    true
```

- **Squared absorbed dose distribution in Gy^2:** Maps the squared absorbed dose within a volume, as:

$$D_k^2 = \sum_{k=1}^{N_{\mathrm{PP}}} d_{k,i}^2 \,, \tag{4.16}$$

where $d_{\mathrm{k,i}}$ is the absorbed dose in voxel k by an independent primary particle i.
Command line to enable output:

```
/gate/actor/[ActorName]/enableSquaredDose             true
```

- **Statistical uncertainty distribution:** Maps the relative statistical uncertainty of a dosimetry simulation. The statistical uncertainty in a voxel k is estimated using the history-by-history method as:

$$SU_k = \frac{\sqrt{\frac{1}{N_{\mathrm{PP}}-1}\left(\frac{\sum_{i=1}^{N} d_{k,i}^2}{N_{\mathrm{PP}}} - \left(\frac{\sum_{i=1}^{N} d_{k,i}}{N_{\mathrm{PP}}}\right)^2\right)}}{D_k/N_{\mathrm{PP}}} \tag{4.17}$$

The squared energy and squared absorbed dose distributions can be used to calculate the statistical uncertainty distribution when adding multiple dosimetry output

files, following Equation 4.17. This is very handy when successive simulations are performed to achieve a smaller level of *SU*.
Command line to enable output:

```
/gate/actor/[ActorName]/enableUncertaintyDose                    true
```

4.4.3.5 Initialization of Simulation

After defining the simulation geometry, physics and output actors, each simulation was initialized through:

```
/gate/run/initialize
```

During initialization, GATE performs pre-dosimetry computation, including the cross-sections for physical interactions, the stopping power and the ionization potential in each geometry material. After initialization, the simulation's geometry, physics and outputs cannot be modified.

As a GATE-MC dosimetry simulation is initialized, it is paramount to set a *seed* for random sampling, which supports all the statistical computations that follow in a MC simulation to study the transport of radiation in a medium[5]. In this work, the *seed* was set to the simulation's start date as:

```
/gate/random/setEngineSeed                                    [DDMMYYYYHH]
```

4.4.3.6 Definition of Radiation Sources

In MC-GATE dosimetry simulations, radiation sources have to be defined, including particle type, position, energy spectrum, angular distribution, and spatial distribution. In this work, ^{90}Y is the key radiation source for both dosimetry methods. Therefore, a uniform cubic source of 2.21 mm edge emitting ^{90}Y radiation was activated for all simulations, as described below:

- **Source type:** GEANT4 General Particle Source (GPS) was used to define the radiation source.
  Command line:

  ```
  /gate/source/addSource                                  Y90source gps
  ```

- **Particle type:** The electron (e^-) particle was set to describe ^{90}Y beta-spectrum.
  Command line:

  ```
  /gate/source/Y90source/gps/particle                             e-
  ```

[5]Note that all simulations should be initialized with a different seed to generate different results.

- **Energy spectrum:** A *UserSpectrum* was used to define the energy of the radiation source in a histogram mode. The energy beta-spectrum that characterizes ^{90}Y decay was extracted from the Brookhaven National Laboratory database [15].
  Command line:

```
/gate/source/Y90source/gps/energytype                UserSpectrum
/gate/source/Y90source/gps/setSpectrumFile         [Filename].txt
```

- **Spatial distribution:** A *Volume* source confines the generation of primary particles to a cube with the size of an image voxel: 2.21x2.21x2.21 mm^3. The spatial distribution of primary particles generation within this volume is uniform.
  Command lines:

```
/gate/source/Y90source/gps/pos/type                     Volume
/gate/source/Y90source/gps/pos/shape                      Para
/gate/source/Y90source/gps/pos/halfx                  1.105 mm
/gate/source/Y90source/gps/pos/halfy                  1.105 mm
/gate/source/Y90source/gps/pos/halfz                  1.105 mm
```

- **Angular distribution:** The direction in which the primary particles are emitted from the source was set to the *isotropic* mode.
  Command line:

```
/gate/source/Y90source/gps/ang/type                       iso
```

- **Position:** The source was set at the isocenter of the simulation.
  Command line:

```
/gate/source/Y90source/gps/pos/centre                 0 0 0 cm
```

The count and spatial distribution of uniform ^{90}Y cubic sources was set according to the simulation type:

1. **Absorbed dose kernel simulation:** A single cubic source was placed at the center of the simulation. No other commands are required to parameterize this source.

2. **Uncalibrated ADDs:** Multiple cubic sources were employed to describe the activity distribution based on patient-specific SPECT or PET images in MetaImage format. GATE's *voxelized source* mechanism was used to convert SPECT or PET images into activity distributions aligned with the *voxelized geometry*. *Voxelized source* generates primary particles in each cubic source proportionally to the count in input images' voxels.
   Command lines:

```
/gate/source/addSource                          Y90Source voxel
/gate/source/Y90Source/reader/insert                      image
/gate/source/Y90Source/imageReader/linearTranslator/setScale  ...
                                                        1 MBq
/gate/source/Y90Source/imageReader/readFile       [Filename].mhd
/gate/source/Y90Source/TranslateTheSourceAtThisIsoCenter  0 0 0 cm
```

4.4.3.7 Acquisition set up and start

MC-GATE dosimetry simulations require the definition of the total number of primary particles to be simulated as:

```
/gate/application/setTotalNumberOfPrimaries [N_PP]
```

A higher number of simulated primary particles yields a lower statistical uncertainty for the *DoseActor* output, but increases the duration of simulations. Therefore, the number of simulated primary particles was set for each simulation type as:

1. **Absorbed dose kernel simulation:** $N_{\mathrm{PP}} = 100 \times 10^6$.

2. **Uncalibrated ADD simulation:** The international atomic energy agency (IAEA) recommends that the mean statistical uncertainty, $\overline{SU}$, within the target volume should be less than 2% for MC simulations in EBRT treatment plans [107], but guidelines for MC simulations in the scope of RE dosimetry are undefined to date. A short investigation presented in Appendix B explores a threshold for $\overline{SU}$ below which the obtained ADDs are sufficiently accurate while keeping the simulation time as low as possible, and defines N_{PP} for ADDs simulations. This investigation concluded that a threshold of 2% for the mean statistical uncertainty in voxels with $D_k > 80$ Gy within the PTV should be reached to ensure dosimetry accuracy. Therefore, the following algorithm was developed to obtain uncalibrated ADDs for each patient:

   a) Initially, ADDs were simulated with $N_{\mathrm{PP}} = 25 \times 10^6$ primary particles;

   b) If the $\overline{SU}_{D_{\mathrm{k}}>80Gy}$ threshold was not reached, a second simulation was started with a different seed.

   c) Then, the first and second simulation's output ADDs were added, and the final statistical uncertainty distribution was computed through Equation 4.17.

   d) Finally, $\overline{SU}_{D_{\mathrm{k}}>80Gy}$ threshold was checked again, repeating steps *b)* and *c)*, if needed.

After defining the number of primary particles, MC-GATE simulations were started following:

```
/gate/application/start
```

4.5 Comparison of VSV- and MC-ADDs

This section describes how the 12 pairs of VSV- and MC-ADDs were compared to test agreement and correlation between them, indicating the *accuracy* of VSV dosimetry and the *relevance* of introducing MC dosimetry in the clinical practice. Special attention was given to the relevant VOIs in RE optimization, i.e., the NLV and PTV, and to the liver interface with surrounding tissues. MC-ADDs were considered the reference ADDs. No considerations were made to differ treatment planning and verification ADDs.

Developed code available at: https://github.com/mariainesribeiro/MasterThesis/tree/main/Comparison_of_VSV_and_MC-ADDs

The following statistical tools were employed to compare VSV- and MC-ADDs, with a significance level of 5%:

- **Bland-Altman plot (BAP):** scatter plot of the relative difference between two paired measurements of a quantity ((A-B)/B) as a function of the average of these measures ((A+B)/2) [108]. Tests the agreement between two measurements.
- **Interclass correlation coefficient (ICC):** tests the absolute agreement between two measurements.
- **Pearson correlation coefficient (PCC):** tests the correlation between two measurements.
- **Relative difference, RD, and absolute relative difference, $\overline{RD}$:** assess the relative and absolute relative change between two measurements as a percentage of the reference measurement.

4.5.1 Comparison within the NLV and PTV

4.5.1.1 Voxelwise Agreement and Correlation

Voxelwise agreement and correlation between VSV- and MC-ADDs, within the NLV and PTV, were assessed through BAPs, ICC and PCC of the absorbed dose in matching voxels.

4.5.1.2 Global Agreement and Correlation

Global agreement and correlation between VSV- and MC-ADDs within the NLV and PTV were assessed by comparing DVHs, mean absorbed doses and EUBEDs computed

for both VOIs.

Agreement and correlation of cDVHs and dDVHs within the NLV and PTV computed for VSV- and MC-ADDs was assesed through the maximum difference, ICC and PCC between equivalent DVHs. The bin width of DVHs was set to 1 Gy.

Agreement and correlation of the mean absorbed dose, $\overline{D}$, within the NLV and PTV computed for VSV- and MC- ADDs was assessed through BAPs, RD, $\overline{\mathrm{RD}}$, ICC, and PCC. The mean absorbed doses within the NLV and PTV are employed in the clinical practice to optimize RE, i.e. to prescribe the optimum activity of ^{90}Y – MS. Therefore, a good agreement and correlation between these features would indicate an equivalent RE optimization outcome, and hence no increase in patients' overall survival.

Agreement and correlation of EUBED within the NLV and PTV computed for VSV- and MC- ADDs was assessed through the same tools as the mean absorbed dose. EUBED considers the non-uniform ADD to quantify the radiobiologic effects of RE within the NLV and PTV, providing more information than only the mean absorbed dose and a single measurement to compare non-uniform ADDs in RE with uniform ADDs in EBRT. Moreover, EUBED might suffer a greater variation between VSV- and MC-ADDs as the latter might yield greater non-uniformity in ADDs due to tissue heterogeneity. EUBED was computed according to Equations 3.8 and 3.9. $T_{1/2}^{EFF}$ was defined as the actual $t_{1/2}$ of ^{90}Y, assuming a null biological clearance of ^{90}Y – MS, i.e., permanent entrapment of ^{90}Y – MS in the liver. Currently, the radiobiological parameters for ^{90}Y – MS irradiation are still unvalidated. In this work, the radiobiological parameters indicated by Chiesa *et al.* [95] were employed (Table 4.7) [6]. These radiobiology parameters were derived from parenchyma volume reduction and TCP analysis.

Table 4.7: Radiobiological parameters used in calculation of EUBED. Retrieved from: [95].

Tissue	α (**Gy**$^{-1}$)	α/β (**Gy**)	$\mathbf{T}_{1/2}^{\mathbf{REP}}$ (**h**)
Normal	0.002	10	2.5
Tumor	0.004	10	1.5

4.5.2 Comparison at the Liver Interface with Surrounding Tissues

Tissue intra- and inter-heterogeneity within the PTV and NLV is expected to be low. In contract, tissue heterogeneity outside the WLV is expected to be significant as it

[6] The values for α and α/β proposed by Chiesa *et al.* are very different form the parameters derived from EBRT ($\alpha = 0.0095$ for normal tissues; $\alpha = 0.01$ for tumors; $\alpha/\beta = 2.5$ for normal tissues; $\alpha/\beta = 15$ for tumors). The smaller α values are explained by a highly non-uniform dose distribution in RE that results in a large waste of deposited energy in overkilling cells. Equal α/β values for normal and tumor tissues were reached for RE because the dose-rate effect is negligible.

includes both lung and bone tissues. Some border voxel within the WLV might already include unexpected tissue heterogeneity due to partial volume artifacts. Therefore, VSV- and MC-ADDs were compared at the liver interface with surrounding tissues to investigate variations due to the tissue heterogeneity and their relevance in the surrounding organs-at-risk.

For each patient, inner (IN) and outer (OUT) volumes were segmented at the liver interface with surrounding tissues using the *3D Slicer*©. OUT volumes might include the following tissues: lung, bone, gallbladder, stomach, intestine, heart and spleen. The segmentation method is described bellow:

1. Expansion of WLV by a margin of 5 voxels (11.05 mm);
2. Shrinkage of WLV by a margin of 5 voxels (11.05 mm);
3. Subtraction of the original WLV to the expanded WLV to obtain OUT volume;
4. Subtraction of the shrunken WLV to the original WLV to obtain IN volume.

Within IN and OUT volumes, the agreement between VSV- and MC-ADDs and the correlation between the relative difference of VSV- and MC-ADDs and tissue heterogeneity were assessed through:

- Relative difference of the mean absorbed dose: assesses the relative change between the mean absorbed dose in VSV- and MC-ADDs within IN and OUT volumes.
- Relative difference/ Heterogeneity plots: plot the relative difference of the mean absorbed dose between VSV- and MC-ADDs within IN and OUT volumes against the mean CT number within the same volumes.
- Patient-specific 1D profiles: plot the absorbed dose in matching k voxels in VSV- and MC-ADDs and the CT number for the same voxel k in a selected 1D profile crossing relevant interface regions, including PTV, NLV, and lungs volume. These plots assess if there is an interface behaviour of absorbed dose in MC-ADDs due to tissue heterogeneity.

To predict and support the results obtained in this section, appendix C investigated the interface behaviour of absorbed dose for a uniform ^{90}Y – MS activity distribution based on MC-GATE dosimetry in comparison to VSV dosimetry. First, a voxelized geometry was set with three adjacent cubes made of three uniform tissues: *lung* RT, *muscle/general* RT and *mineral bone* RT. Then, two different voxelized sources of ^{90}Y were simulated: one with a global uniform source distribution within the three geometry cubes, and the other with a uniform source distribution within the center *muscle/general* RT cube

and null activity in the remaining geometry. The second configuration better resembles the non-uniform activity distribution in RE as ^{90}Y – MS are mostly located within the liver, which is represented by *muscle/general* RT. For this configuration, VSV dosimetry underestimated absorbed doses in *lung* RT voxels at the interface with *muscle/general* RT voxels. Similar results were expected for real RE patient's at the liver interface.

4.6 Comparison of Planning and Verification ADDs

This section describes how the six pairs of planning and verification VSV-ADDs and the six pairs of planning and verification MC-ADDs were compared to assess variations in treatment planning quality between VSV and MC-GATE dosimetry methods.

Developed code available at: https://github.com/mariainesribeiro/MasterThesis/tree/main/Comparison_of_Planning_and_Verification_ADDs

4.6.1 Voxelwise Agreement and Correlation within the NLV and PTV

Voxelwise agreement and correlation between the 12 pairs of planning and verification ADDs (six pairs of VSV-ADDs; six pairs of MC-ADDs) were assessed through voxelwise ICC, PCC, and γ-index test within the NLV and PTV. In this work, the γ-index test was implemented using an algorithm developed by Ferreira. P *et al.* at CCU-CF [98]. The γ-index test has been extensively used in EBRT quality assurance by comparing planning a verification ADDs [109]. The concept of the γ-index test is described below.

The γ-index test computes a γ-index for each matching voxel in planning and verification ADDs, according to dose difference (DD) and distance to agreement (DTA) combined criteria and then uses the γ-index to determine the passing rate (PR) of all voxels in a VOI [109]. DD is the maximum tolerated dose difference of two voxels in planning and verification ADDs, in percentage. DTA is the maximum tolerated distance between a reference voxel and a test voxel that meets the defined DD criterion. In more detail, the γ-index PR within a VOI is computed as:

1. For each voxel v in a verification ADD, the following quantities are computed against each voxel p in a matching planning ADD:
   a) $\Delta r(v,p)$, euclidean distance between v and p;
   b) $\Delta D(v,p)$, dose difference between p and v.
   c) $\Gamma(v,p) = \sqrt{\frac{\Delta D^2(v,p)}{DD^2} + \frac{\Delta r^2(v,p)}{DTA^2}}$, a map of γ-index candidates for voxel v;
   d) $\gamma(v) = min\{\Gamma(v,p)\}, \forall\{p\}$, the selected γ-index candidates for voxel v.

2. For all $\gamma(v)$ within a VOI, PR is the percentage of voxels where $\gamma(v) < 1$, assuming that the planning and verification ADDs were normalized to the verification ADD.

4.6.2 Global Agreement and Correlation within the NLV and PTV

Global agreement and correlation between planning and verification ADDs obtained with each dosimetry method were assessed through the ICC and PCC computed for the mean absorbed doses within the NLV and PTV. In addition, the mean absorbed doses in planning ADDs were plotted against those in verification ADDs for both dosimetry methods and within the NLV and PTV.

Chapter 5

Pre-Dosimetry Results

This chapter describes the results obtained in the stoichiometric calibration of HU to tissue parameters, quantification of tissue heterogeneity within each patient's NLV and PTV, and computation of a VSV kernel with a MC-GATE dosimetry simulation.

5.1 Stoichiometric Calibration of Hounsfield Units to Tissue Parameters

5.1.1 Parameterization of a CT Scanner with Tissue Substitutes

The parameterization of the PET/CT Philips Gemini scanner resulted in $k_1 = -5.51 \times 10^{-4}$ and $k_2 = 4.39 \times 10^{-5}$. Table 5.1 lists both measured and calculated HU for each TS. The maximum deviation occurs for air ($\Delta = 23$ HU). An excellent coefficient of determination of 99.96% was achieved between measured and calculated HU, as illustrated in Figure 5.1.

Table 5.1: Measured and calculated HU for the eight TSs in CATPHAN 604.

TS	Measured HU	Calculated HU
Air	-976	-999
PMP	-177	-177
LDPE	-90	-88
Polystyrene	-32	-36
Acrylic	117	121
Bone20%	226	225
Bone50%	671	671
Delrin	345	345

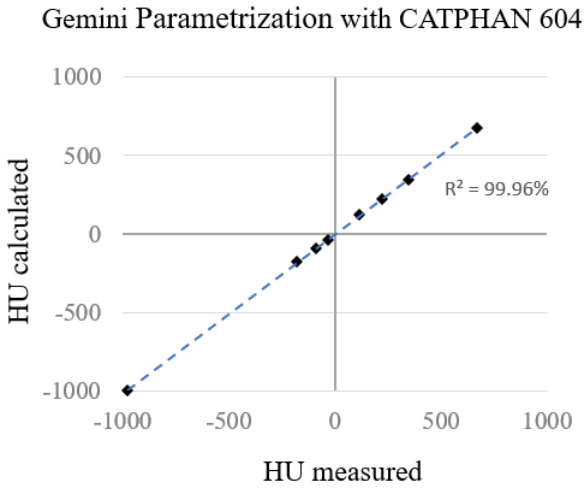

Figure 5.1: PET/CT Philips Gemini parametrization with TS of CATPHAN 604 (air, PMP, LDPE, polystyrene, acrylic, bone 20%, bone 50% and delrin). The coefficient of determination is 99.96%.

5.1.2 Converting Hounsfield Units to Tissue Parameters

5.1.2.1 Converting Hounsfield units to mass density

Table 5.2 lists the calculated HU for each of the 11 RTs. The calculated HU of the 11 RTs and their mass density values were used to defined GATE's input file for the poly-line calibration of HU to mass density. GATE's input file for the poly-line calibration of HU to mass density are available at: https://github.com/mariainesribeiro/MasterThesis/blob/main/Stoichiometric_Calibration_of_HU/GATE's_files/GEMINIDensitiesTable.txt

Table 5.2: Calculated HU for the 11 RTs.

RT	HU
1. Air	-999
2. Lung	-620
3. Extra lung	-205
4. Fat	-122
5. Adipose/Marrow	-70
6. Muscle/General	42
7. Miscellaneous	81
8. Heavy Spongiosa	207
9. Mineral Bone	1603
10. Tooth	3130
11. Hydroxyapatite	4386

The empirical HU of each standard tissue in ICRP Publication 110 was calculated

according to equations 2.8 and 4.3 and using the fitted k_1 and k_2 values for PET/CT Philips Gemini scanner. Then, their mass density was estimated according to the calibration poly-line. Figures 5.2 and 5.3 plot the HU-density poly-line and the scatter points of ICRP standard tissues in the full HU range and in the HU range of soft tissues ([-100; 100]), respectively.

Most tissues lie in the calibration curve, indicating a good HU calibration accuracy. The median difference, absolute median difference, median relative difference, and absolute median relative difference between the reference mass density and the estimated one are -4.2×10^{-15} g/cm^3, 3.9×10^{-3} g/cm^3, -1.95×10^{-13}% and 3.91×10^{-1}%, respectively. The maximum absolute difference (0.05 g/cm^3) and maximum absolute relative difference (4.65%) occur for the thyroid tissue deviating from the poly-line (see Figure 5.3)[1].

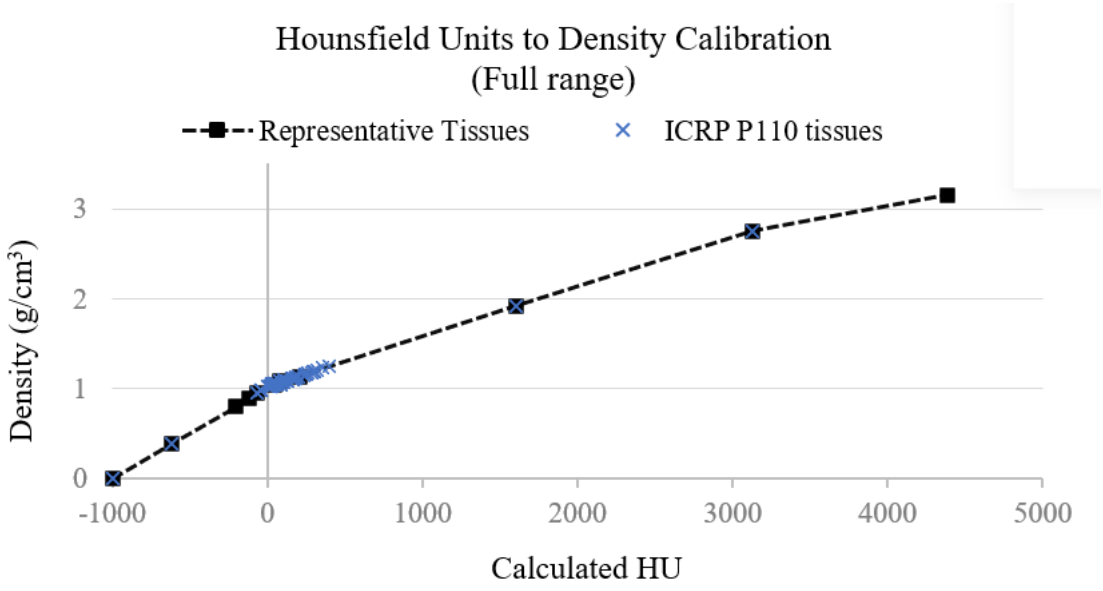

Figure 5.2: Calibration poly-line to convert HU to mass density in the full HU range, i.e. [-1000, 4500]. The empirical (HU, mass density) points of ICRP standard tissues are plotted.

[1]Thyroid deviates because it contains a small percentage of iodine (0.1%) that has a very high atomic number ($Z = 53$) comparing to the other elements in human tissues ($Z < 20$), significantly increasing the photoelectric effect cross-section.

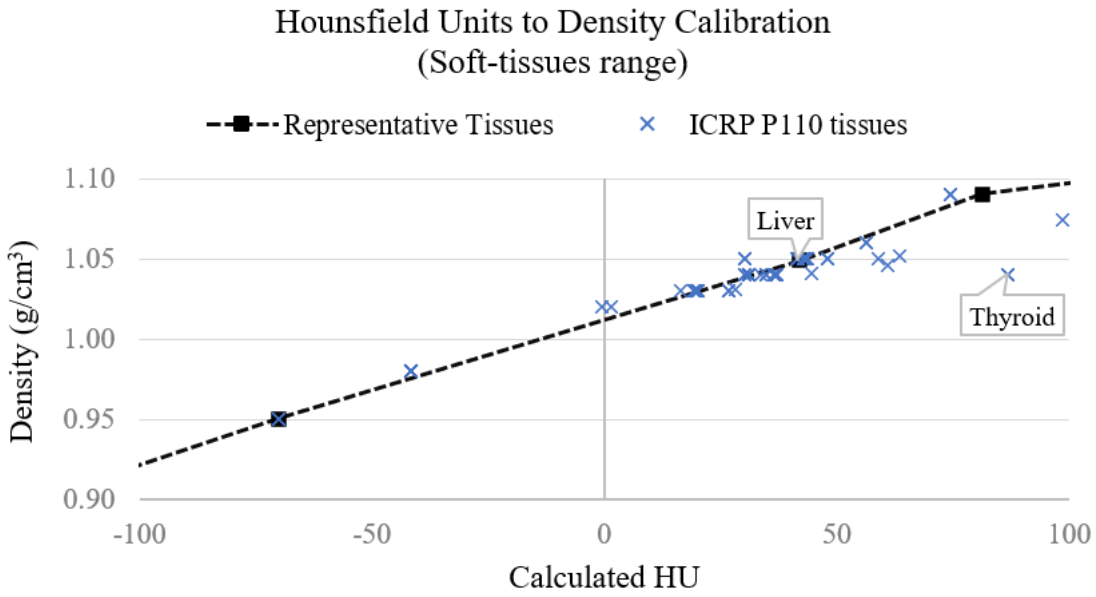

Figure 5.3: Calibration poly-line to convert HU to mass density in the soft tissues HU range, i.e. [-100, 100]. The empirical (HU, mass density) points of ICRP standard tissues are plotted.

5.1.2.2 Converting mass density chemical composition

Table 5.3 presents the tissue parameters of the 19 bins created to convert HU to the chemical composition in GATE. GATE input file to calibrate HU to chemical composition available at: https://github.com/mariainesribeiro/MasterThesis/blob/main/Stoichiometric_Calibration_of_HU/GATE's_files/GEMINIMaterialsTable.txt

The reference elemental weights of each standard tissue in ICRP Publication 110 were compared to those of the respective RT. The maximum absolute differences are: hydrogen 1.15%, carbon 37.01%, nitrogen 2.71%, oxygen 35.95%, sodium 0.29%, magnesium 0.08%, phosphorus 1.77%, sulfur 0.63%, Chlorine 0.27%, potassium 0.36%, calcium 3.86% and ion 0.10%. The biggest deviation occurs between carbon and oxygen because soft tissues have very different contents of water ($w_C = 0\%; w_O = 88.8\%$) and fat ($w_C = 58.9\%; w_O = 28.7\%$) [99].

Table 5.3: Chemical composition, mass density, and bin HU limits of the 19 RTs.

Representative Tissue	HU Bin		Elemental Weight (%)												ρ(g/cm^3)
	Min	Max	H	C	N	O	Na	Mg	P	S	Cl	Ar	K	Ca	Fe	
1. Air	-1000	-901	-	0.01	75.52	23.17	-	-	-	-	-	1.30	-	-	-	-
2. Lung	-900	-412	10.30	10.70	3.20	74.60	0.20	-	0.20	0.30	0.30	-	0.20	-	-	0.38
3. Extra lung	-411	-163	10.30	10.70	3.20	74.60	0.20	-	0.20	0.30	0.30	-	0.20	-	-	0.80
4. Fat	-162	-96	11.96	76.87	-	11.17	-	-	-	-	-	-	-	-	-	0.90
5. Adipose/Marrow	-95	-14	11.40	58.91	0.75	28.64	0.10	-	-	0.10	0.10	-	-	-	-	0.95
6. Muscle/General	-13	62	10.25	14.59	3.21	70.85	0.11	-	0.21	0.27	0.13	-	0.36	0.02	-	1.05
7. Miscellaneous	63	144	9.94	20.92	3.85	63.72	0.22	-	0.43	0.27	0.29	-	0.09	0.26	0.01	1.09
8. Heavy Spongiosa	145	284	9.32	39.14	2.21	41.79	0.19	0.02	2.34	0.29	0.13	-	0.04	4.53	-	1.14
9. HS-MB 1	285	440	8.69	36.56	2.43	42.13	0.20	0.03	3.12	0.29	0.12	-	0.04	6.39	-	1.22
10. HS-MB 2	441	595	8.05	33.97	2.65	42.46	0.21	0.06	3.91	0.29	0.10	-	0.04	8.26	-	1.31
11. HS-MB 3	596	750	7.42	31.39	2.87	42.80	0.22	0.08	4.69	0.29	0.09	-	0.03	10.12	-	1.40
12. HS-MB 4	751	905	6.78	28.81	3.09	43.13	0.24	0.10	5.48	0.29	0.07	-	0.02	11.98	-	1.48
13. HS-MB 5	906	1060	6.14	26.23	3.32	43.46	0.25	0.12	6.26	0.29	0.06	-	0.02	13.85	-	1.57
14. HS-MB 6	1061	1216	5.51	23.65	3.54	43.80	0.26	0.14	7.05	0.30	0.04	-	0.01	15.71	-	1.66
15. HS-MB 7	1217	1371	4.87	21.07	3.76	44.13	0.27	0.16	7.83	0.30	0.03	-	0.01	17.57	-	1.75
16. HS-MB 8	1372	1526	4.24	18.48	3.98	44.47	0.29	0.18	8.61	0.30	0.01	-	-	19.44	-	1.83
17. Mineral Bone	1527	2367	3.60	15.90	4.20	44.80	0.30	0.20	9.40	0.30	-	-	-	21.30	-	1.92
18. Tooth	2368	3758	2.20	9.50	2.90	42.10	-	0.70	13.70	-	-	-	-	28.90	-	2.75
19. Hydroxyapatite	3759	-	0.20	-	-	41.41	-	-	18.50	-	-	-	-	39.89	-	3.16

5.2 Tissue Heterogeneity within the NLV and PTV

5.2.1 Mass Density Heterogeneities

Figure 5.4 plots the distribution of mass density associated to voxels in patients' CT images, according to the HU calibration, within the PTV and NLV. The outliers are not represented. The mean mass density within each patient's NLV and PTV ranges from 1.017 to 1.074 g/cm^3 and 1.028 to 1.069 g/cm^3, respectively. The maximum IQR of mass density within each patient's NLV and PTV is 0.018 and 0.016 g/cm^3, respectively.

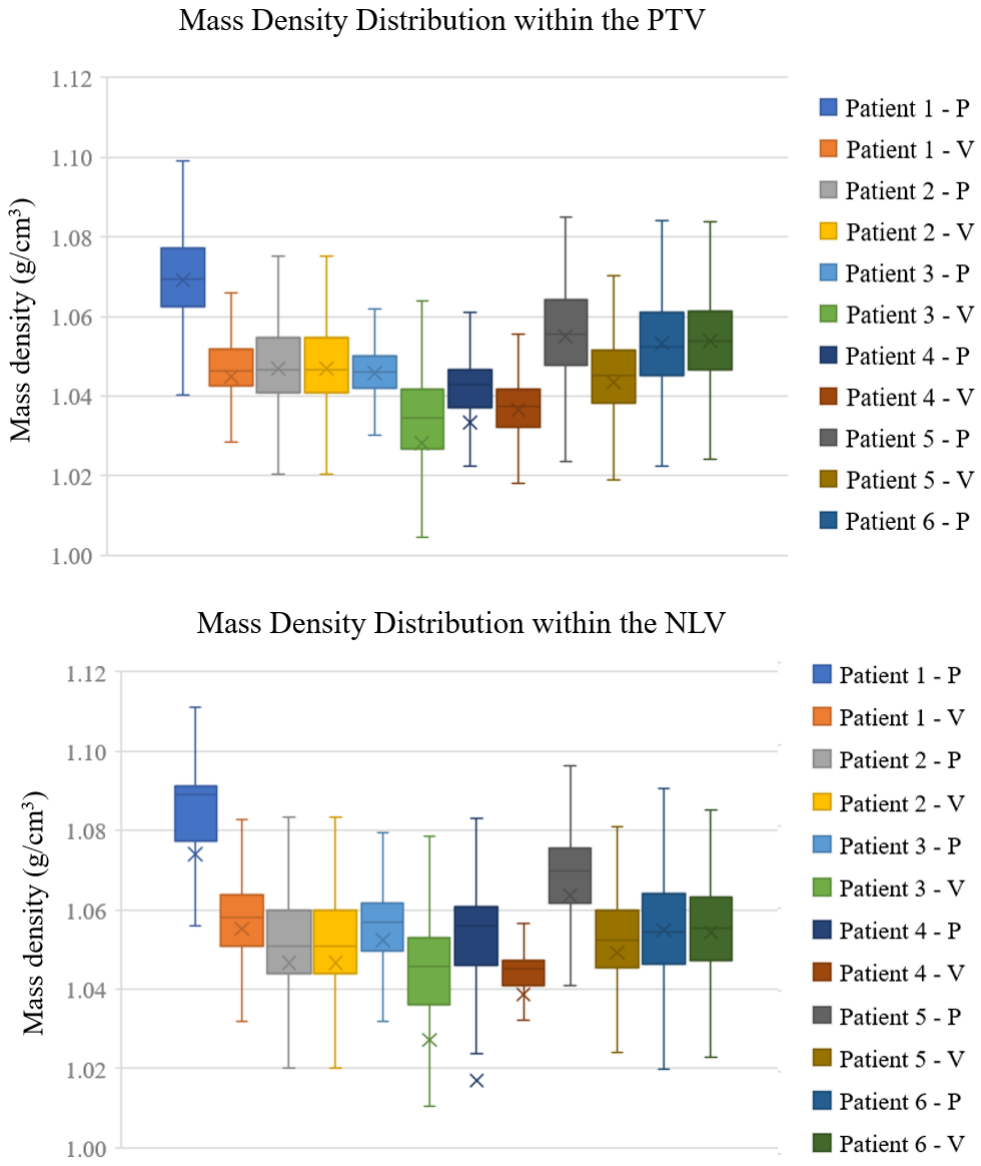

Figure 5.4: Mass density distribution associated to voxels in CT images according to the HU calibration. Outliers are not represented. (P - Planning; V - Verification)

5.2.2 Chemical Composition Heterogeneities

Tables 5.4 and 5.5 list the percentage of voxels in patients' CT images assigned to 3 of the 11 RTs (*Adipose/Marrow*, *Muscle/General*, and *Miscellaneous*) after HU calibration within the PTV and NLV, respectively. Less than 1% of the voxels within the VOIs are associated to each of the remaining RTs. The median percentages of voxels assigned to the *Muscle/ General* RT within the NLV and PTV are 81.3% and 94.3%, respectively.

Table 5.4: Percentage of voxels in CT images within the PTV assigned to RT 5 to 7 after the HU calibration. (P - planning; V - verification; RT 5 - Adipose/Marrow; RT 6 - Muscle/ General; RT 7 - Miscellaneous.)

	Patient 1		**Patient 2**		**Patient 3**		**Patient 4**		**Patient 5**		**Patient 6**	
	P	**V**	**P**	**V**	**P**	**V**	**P**	**V**	**P**	**V**	**P**	**V**
RT 5	0.6	2.1	0.2	0.2	0.1	0.9	3.0	0.2	1.0	1.7	0.1	0.4
RT 6	37.2	96.6	93.3	93.3	99.7	97.4	95.5	99.8	78.9	95.3	84.4	86.0
RT 7	62.2	1.3	6.3	6.3	0.2	0.2	0.3	0.0				

Table 5.5: Percentage of voxels in CT images within the NLV associated to RT 5 to 7 after the HU calibration. (P - planning; V - verification; RT 5 - Adipose/Marrow; RT 6 - Muscle/ General; RT 7 - Miscellaneous.)

	Patient 1		**Patient 2**		**Patient 3**		**Patient 4**		**Patient 5**		**Patient 6**	
	P	**V**	**P**	**V**	**P**	**V**	**P**	**V**	**P**	**V**	**P**	**V**
RT 5	1.7	1.7	3.9	3.9	1.5	4.0	3.3	2.0	2.3	2.4	0.8	1.3
RT 6	11.6	81.8	83.1	83.1	91.2	89.1	83.1	96.3	33.5	86.4	77.8	80.8
RT 7	85.3	16.3	11.8	11.8	7.0	3.3	6.7	0.1	63.0	10.6	21.3	17.8

5.3 Voxel S-Values Kernel Simulation with MC-GATE

The MC-GATE simulation of absorbed dose kernel took approximately 11.4 hours. Afterward, the absorbed dose kernel was calibrated to the VSV kernel as described in section 4.4.1. The time required to simulate the absorbed dose kernel should be neglected in VSV dosimetry clinical time schedule because it is performed only once a priori and it is suitable for all future patients.

Figure 5.5 plots the simulated and reference S-values in cubic voxels of 2.21 mm edge as a function of the distance to the center ^{90}Y source voxel irradiating isotropically in a soft tissue medium. Appendix D lists theses values in an octant of the VSV kernel in more detail[2].

[2]Only an octant of the VSV kernel was analysed because the kernel is symmetric with respect to the

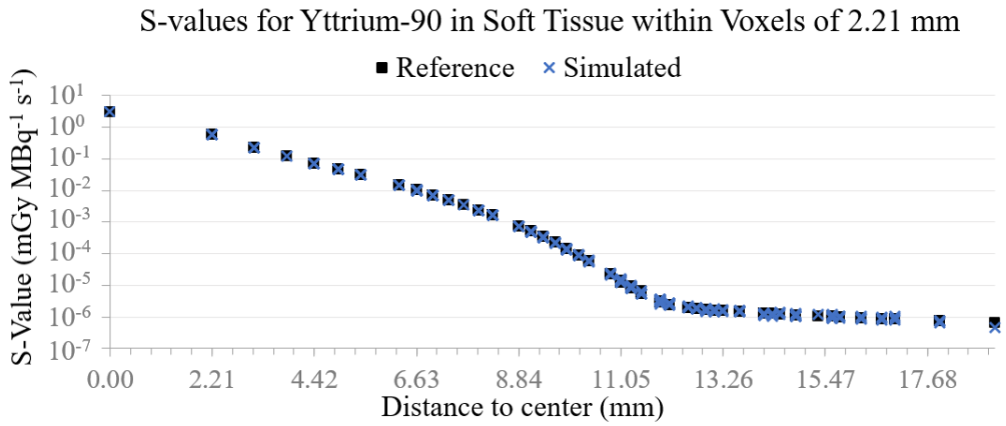

Figure 5.5: Reference and simulated voxel S-values for Yttrium-90 in cubic voxel of 2.21 mm.

Figure 5.6 plots the relative difference between the simulated and reference S-values as a function of the distance to center. The agreement between reference and simulated S-values is described below, as a function of the distance to the center source voxel[3].

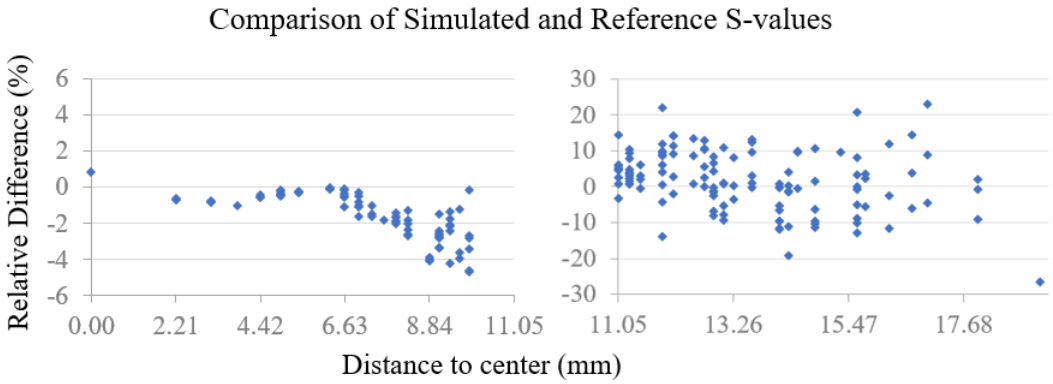

Figure 5.6: Relative difference between reference and simulated voxel S-values for ^{90}Y in cubic voxel of 2.21 mm.

1. **At the center source voxel**, a relative difference of +0.8% was achieved. Such good agreement at the source voxel is relevant for dosimetry accuracy because this voxel absorbs at least 10 times more dose than any other voxel in the VSV kernel. The small relative difference is due to range and energy cuts set for the physics in the MC-GATE simulation. Physics cuts result in a higher absorbed dose within the source voxel. A VSV kernel simulation with minor physics cuts was performed in this work, returning a relative difference of only +0.1% at the source voxel, but the simulation

center, i.e. to the source voxel.

[3]When simulating the absorbed dose kernel, the center voxel is the only voxel emitting radiation that contributes to dose absorption within itself and in the whole kernel. For this reason, the center voxel is called *source voxel* and the remaining voxels in the kernel are called *target voxels*. However, note that all voxels in a VSV kernel contribute to the absorbed dose in VSV dosimetry calculations with the convolution operation

time was 7 times longer. For VSV dosimetry, such increase in simulation time would be acceptable because the VSV kernel is simulated only once, being immediately available for all future patient. However, it could jeopardize the clinical feasibility of direct MC dosimetry to simulate ADDs without a significant gain in accuracy. Because of that, cuts were maintained for the simulation of the VSV kernel to control the comparison of VSV and MC-ADDs.

2. **For voxels within 11.05 mm to the center**, the absolute relative difference is smaller than 5% and the relative difference is negative for all voxels. Physics' cuts are again responsible for the negative relative difference within these voxels. With increasing distance to the center source voxel, there is a higher variance of simulated S-values because only a few primary beta-minus particles reach further voxels as the maximum range of ^{90}Y $\beta-$ radiation in soft tissues is around 11 mm. A poorer agreement within these voxels was considered acceptable for VSV dosimetry because the S-value decreases exponentially as the distance to the center voxel increases.

3. **For voxels further than 11.05 mm to the center**, the relative difference is random because (1) only secondary Bremsstrahlung photons with greater penetration power can reach such voxels, and (2) the number of Bremsstrahlung photons is rather small. Overall, a random relative difference at voxels further than 11.05 mm has low impact on VSV-ADD because the S-values are at least 10^5 times smaller than that at the source voxel.

Chapter 6

Dosimetry Results

This chapter describes the results obtained in the comparison of ADDs. First, the duration of MC-GATE simulations of patient-specific ADDs was reported to assess the feasibility of MC dosimetry in the clinical practice. Second, VSV- and MC-ADDs were tested for agreement and correlation to assess the accuracy of VSV dosimetry and relevance of MC dosimetry in the clinical practice. Finally, planning and verification ADDs obtained with the same dosimetry method were compared to assess variations in treatment planning quality.

Figure 6.1 illustrates VSV- and MC-ADDs obtained for Patient 1 treatment planning and verification and the voxelwise difference between matching ADDs. The most relevant observations are listed below.

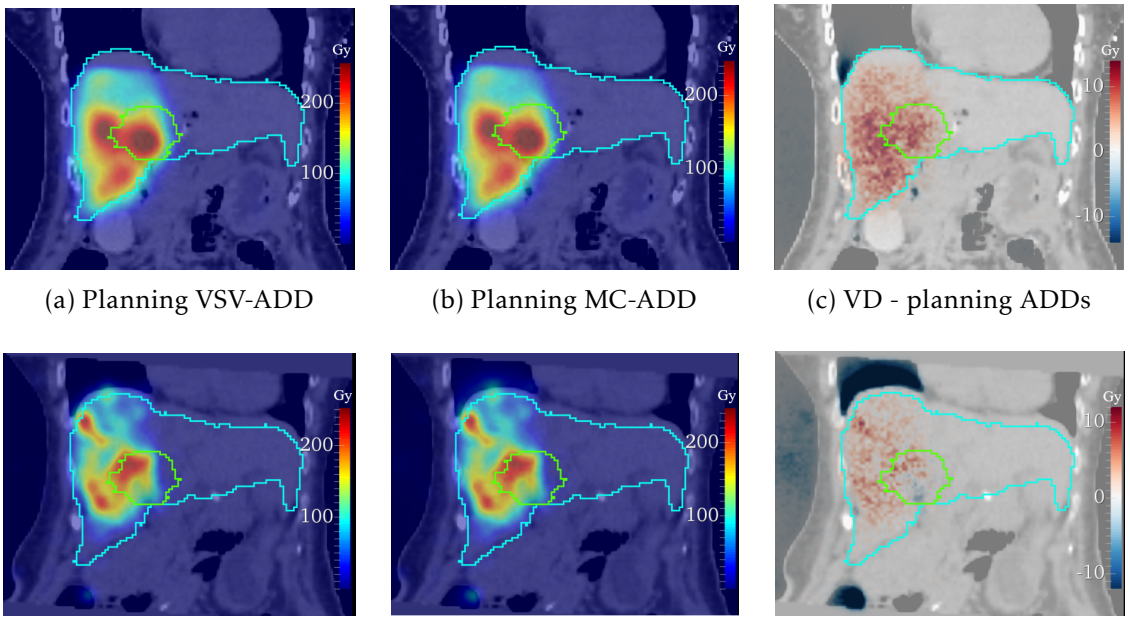

(a) Planning VSV-ADD (b) Planning MC-ADD (c) VD - planning ADDs

(d) Verification VSV-ADD (e) Verification MC-ADD (f) VD - verification ADDs

Figure 6.1: Coronal view of VSV- and MC-ADDs obtained for patient 1 treatment planning and verification and the voxelwise difference (VD) matching ADDs, in Gy. CT images are shown as background. NLV and PTV are outlined in blue and green, respectively.

1. **Comparison between matching MC-ADDs and VSV-ADDs:**

   a) **Within the WLV, including the NLV and PTV:** at low absorbed dose voxels (<100 Gy), the voxelwise difference between VSV- and MC-ADDs appears to be very low and random (< 1 Gy); while at high absorbed dose voxels (> 100 Gy), the voxelwise difference appears to be mostly low and positive (<10 Gy). Section 6.1.2.1 quantifies the voxelwise agreement and correlation between MC- and VSV-ADDs within the NLV and PTV. Comparing ADDs in a voxelwise scale might have a weak influence in the global level of VOIs, i.e., the relevant scale for RE optimization. Section 6.1.2.2 describe the global agreement and correlation between MC- and VSV-ADDs within the NLV and PTV.

   b) **Outside the WLV:** the voxelwise difference between VSV- and MC-ADDs is mostly low (<1 Gy), but it is negative and large (>10 Gy) within darker regions in CT images associated to lungs and air cavities. For example, at the liver interface with lungs in treatment verification: there is a larger spread of absorbed dose within the lungs for MC-ADD than in VSV-ADD (observe a small dose spread at the top-left outline of the NLV segmentation at Figures 6.1d and 6.1e). The absorbed dose spread is larger in treatment verification than in treatment planning because there is a higher absorbed dose at the liver interface with lungs. Section 6.1.3 compares MC- and VSV-ADD at the liver interface with surrounding tissues.

2. **Comparison between planning and verification ADDs:** there is a visible variation between planning and verification ADDs, which appears to be equivalent for MC and VSV dosimetry. Section 6.2 tests the voxelwise agreement and correlation between planning and verification ADDs obtained with both dosimetry methods to assess variations in treatment planning quality and its predictive power.

6.1 Comparison of VSV- and MC-ADDs

6.1.1 Duration of MC-GATE dosimetry simulations

Table 6.1 lists the number of simulated primary particles and duration of MC-GATE dosimetry simulations reported for each RE patient and treatment stage. MC-ADDs were simulated on average for 24.9 hours [min = 8.9; max = 47.2] to achieve the predefined statistical uncertainty threshold within the PTV. The following calibration step on *MATLAB*© took only a few seconds. On the other hand, VSV-ADDs were obtained directly on *MATLAB*© in just a few seconds.

Table 6.1: Number of simulated primary particles and duration of MC-GATE dosimetry simulation for each RE patient and treatment stage (P - planning; V - verification).

Patient	Stage	N_{PP} (10^6)	Time (h)
1	P	100	17.2
	V	100	19.4
2	P	250	47.2
	V	200	36.9
3	P	125	25.2
	V	150	22.8
4	P	100	18.7
	V	200	44.8
5	P	50	9.7
	V	50	8.9
6	P	110	20.1
	V	150	27.5

6.1.2 Comparison within the NLV and PTV

6.1.2.1 Voxelwise Agreement and Correlation

Figure 6.2 displays voxelwise BAPs of the absorbed dose in matching voxels in VSV- and MC-ADDs for Patient 1 treatment planning and verification within the NLV and PTV. For low absorbed dose voxels, a large and symmetric relative difference distribution is shown; while for high absorbed dose voxels, the relative difference converges to values similar to the median voxelwise relative difference and close to 0%.

Table 6.2 lists the median voxelwised ICC and median PCC between all VSV- and MC-ADDs within the NLV and PTV. Excellent agreement and correlation was found within both VOIs (ICC > 0.99; PCC > 0.99).

Table 6.2: Median voxelwised ICC and median PCC between VSV- and MC-ADDs within the NLV and PTV.

VOI	Median ICC	Median PCC
NLV	0.9992	0.9995
PTV	0.9994	0.9996

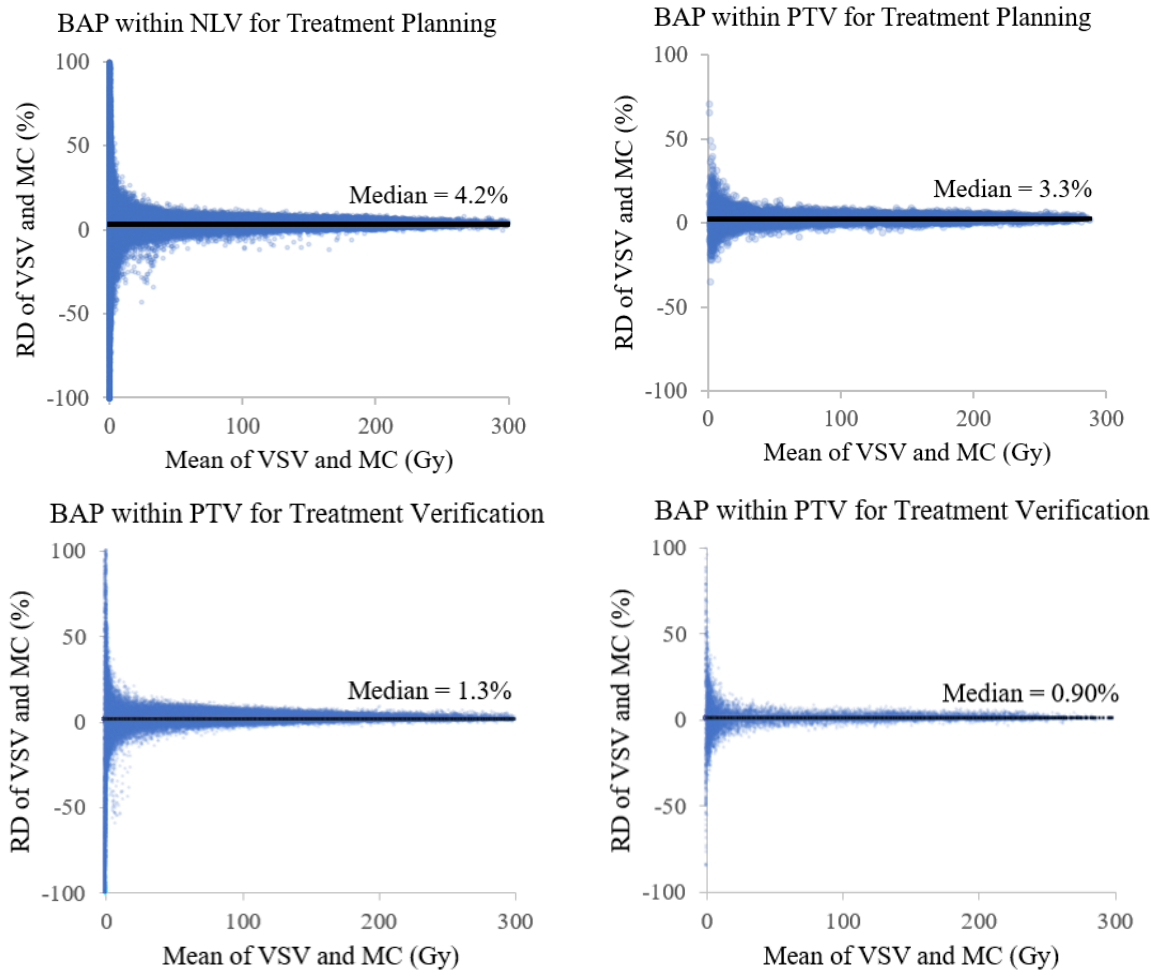

Figure 6.2: Voxelwise BAP of absorbed dose in matching voxels in VSV- and MC-ADDs for Patient 1 treatment planning and verification within the NLV and PTV.

6.1.2.2 Global Agreement and Correlation

Figure 6.3 plots cDVHs and dDVHs for patient 1 computed for VSV-ADDs and MC-ADDs within the NLV and PTV. Appendix E plots DVHs for the remaining patients. First of all and as expected in RE, DVHs display very non-uniform ADDs comparing to ADDs in EBRT:

1. cDVH show a steep decrease from absorbed dose values close to zero, instead of a plateau up to medium/ high absorbed dose values;

2. dDVH show a large spread of the volume throughout the absorbed dose spectrum, with a peak for absorbed dose close to zero, instead of a gaussian curve with a high mean absorbed dose.

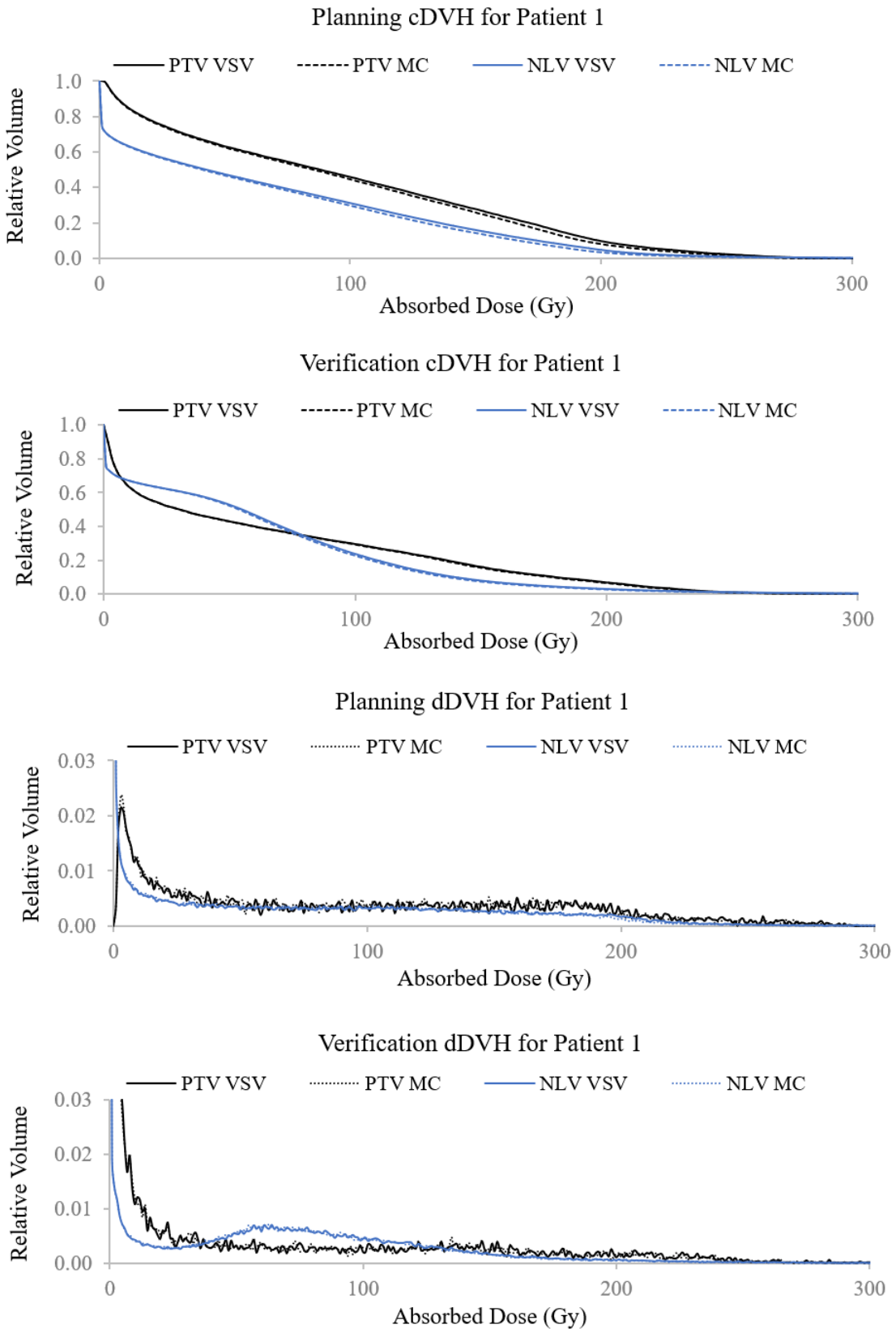

Figure 6.3: cDVH and dDVH for patient 1 computed for planning and verification VSV- and MC-ADDs within the NLV and PTV.

Table 6.3 lists the overall maximum absolute difference (D_{max}), median ICC, and median PCC between DVHs computed for all VSV- and MC-ADDs within the NLV and PTV. Excellent agreement and correlation between pairing DVHs was found (ICC > 0.99; PCC > 0.99). For cDVHs, D_{max} within the NLV and PTV was 2.2% and 2.4%, respectively. For dDVH, D_{max} within the NLV and PTV was 2.0% and 0.30%, respectively.

Table 6.3: Overall maximum absolute difference, median ICC, and median PCC between DVHs computed for all VSV- and MC-ADDs within the NLV and PTV.

VOI	DVH	D_{max} (%)	Median ICC	Median PCC
NLV	cumulative	2.2	0.9999	1.0000
	differential	2.0	0.9999	0.9999
PTV	cumulative	2.4	0.9999	1.0000
	differential	0.30	0.9971	0.9971

Figure 6.4 displays BAPs of the mean absorbed dose and EUBED between all VSV- and MC-ADDs within the NLV and the PTV. The scatter points in each BAP show positive mean relative differences smaller than 1%.

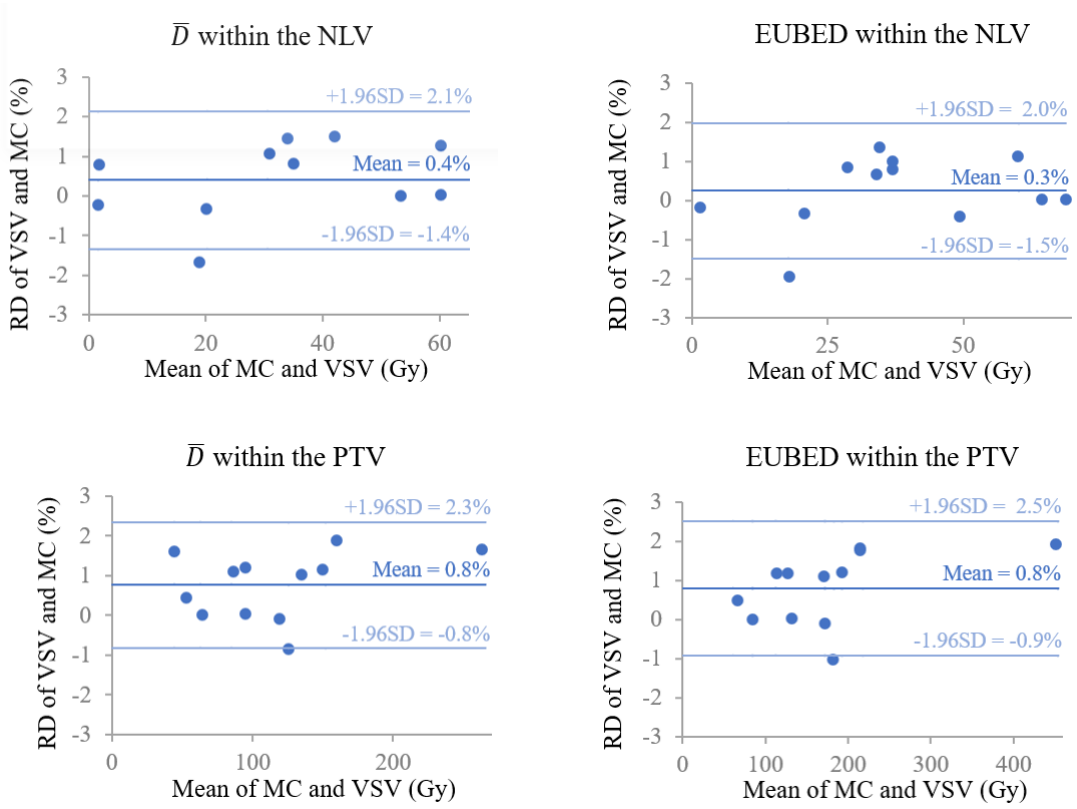

Figure 6.4: BAPs of the mean absorbed dose and EUBED between all VSV- and MC-ADDs within the NLV and PTV.

Table 6.4 lists the values of mean absorbed dose and EUBED computed for all VSV-ADDs and MC-ADDs. For most ADDs, the mean absorbed dose within the NLV does not exceed 60 Gy and it is lower than that within the PTV. For each patient, EUBED is similar to the mean absorbed dose within the NLV, while EUBED is higher than the mean absorbed dose within the PTV (median RD = +34 Gy). These results are explained by a higher radiosensitivity ($> \alpha$) in the tumor tissue than in the normal tissue, and suggest that the real therapeutic index of RE was better than expected for the patients included in this work.

Table 6.4: Mean absorbed dose and EUBED computed for all VSV- and MC-ADDs within the NLV and PTV.

			$\overline{D}$ (Gy)			EUBED (Gy)		
VOI	**Patient**	**Stage**	**VSV**	**MC**	***RD* (%)**	**VSV**	**MC**	***RD* (%)**
NLV	1	P	66.7	63.9	4.3	70.3	67.6	4.1
		V	60.9	59.6	2.2	65.2	63.8	2.2
	2	P	31.1	30.7	1.1	28.9	28.6	0.8
		V	35.1	34.8	0.8	34.2	34.0	0.7
	3	P	60.5	59.7	1.3	60.3	59.6	1.1
		V	53.3	53.3	0.0	49.2	49.4	-0.4
	4	P	18.7	19.1	-1.7	17.9	18.2	-2.0
		V	20.1	20.2	-0.3	20.6	20.7	-0.3
	5	P	1.8	1.8	0.8	1.8	1.8	0.8
		V	1.5	1.5	-0.2	1.5	1.5	-0.2
	6	P	34.3	33.8	1.5	34.8	34.3	1.4
		V	42.3	41.7	1.5	37.1	36.8	1.0
PTV	1	P	96.5	93.4	3.4	134.5	129.4	4.0
		V	64.7	64.0	1.1	85.4	84.4	1.2
	2	P	150.9	149.2	1.1	171.5	169.7	1.1
		V	135.2	133.8	1.0	193.4	191.2	1.2
	3	P	86.5	85.6	1.1	114.7	113.3	1.2
		V	95.6	94.4	1.2	128.1	126.6	1.2
	4	P	125.3	126.4	-0.9	181.1	183.0	-1.0
		V	118.9	119.0	-0.1	172.0	172.2	-0.1
	5	P	44.5	43.8	1.6	54.3	53.3	1.8
		V	52.9	52.7	0.4	67.0	66.7	0.5
	6	P	265.5	261.2	1.7	455.7	447.0	1.9
		V	161.5	158.5	1.9	216.4	212.6	1.8

Table 6.5 lists the relative difference, absolute relative difference, ICC, and PCC between the mean absorbed dose and EUBED computed for all VSV- and MC-ADDs within the PTV and NLV. Excellent agreement and correlation between the mean absorbed dose and EUBED was found (ICC > 0.99; PCC > 0.99). The median relative differences between VSV- and MC-ADDs within the PTV and the NLV were smaller than 1.1% and 0.7%, with IQRs smaller than 1.3% and 1.1%, respectively.

Table 6.5: Relative difference, absolute relative difference, ICC, and PCC between the mean absorbed dose and EUBED computed for VSV- and MC-ADDs within the NLV and PTV.

		RD (%)		$\overline{RD}$ (%)			
VOI	**Feauture**	**Median**	**IQR**	**Median**	**95th**	**ICC**	**PCC**
NLV	$\overline{D}$	0.4	1.2	0.8	1.6	0.9991	0.9996
	EUBED	0.4	1.1	0.7	1.6	0.9915	0.9914
PTV	$\overline{D}$	1.1	1.3	1.1	1.8	0.9994	0.9998
	EUBED	1.1	1.3	1.1	1.9	0.9995	0.9998

6.1.3 Comparison at the Liver Interface with Surrounding Tissues

Table 6.6 describes the relative difference between the mean absorbed dose computed for all VSV- and MC-ADDs within IN and OUT interface volumes. The median relative differences of the mean absorbed dose within IN and OUT volumes were 1.0% and -16%, respectively. These results indicates a higher variation between VSV- and MC-ADDs outside the WLV, with a significant underestimation of absorbed dose by VSV dosimetry.

Table 6.6: Distribution of the relative difference between mean absorbed dose computed in pairs of VSV- and MC-ADDs within the IN and OUT volumes.

VOI	RD (%)	
	Median	**IQR**
IN	1.0	1.2
OUT	-16	5.7

Table 6.7 describes the distribution of CT numbers, in HU, in all Patients' CT images within the IN and OUT volumes. The median of the mean CT number within IN volume in all CT images is higher than that within OUT volume, because the former includes mostly soft tissue and the latter includes a significant portion of lung tissue. The median of the standard deviation of CT number within IN volume is over 5 times smaller than that in OUT volume, indicating a higher tissue heterogeneity within the OUT volume[1].

[1] Note that the OUT volumes include multiple tissues: lung, bone, gallbladder, stomach, intestine, heart and spleen

Table 6.7: Medians of the mean and standard deviation of CT numbers, in HU, in all Patients' CT images within the IN and OUT volumes.

VOI	Mean HU	SD HU
IN	42.7	45.6
OUT	-92.2	265.6

Figure 6.5 plots the relative difference between the mean absorbed dose computed for all VSV- and MC-ADDs within the IN and OUT volumes against the mean HU in Patients' CT images within these volumes. This plot assesses the impact of tissue heterogeneity at the liver interface in the accuracy of VSV dosimetry. A good correlation between the relative difference of the mean absorbed dose and mean HU was found (R^2 = 0.84). Additionally, Figure 6.5 depicts lower mean HU within the OUT volume comparing to the IN volume, as expected due to the liver interface with lung tissues.

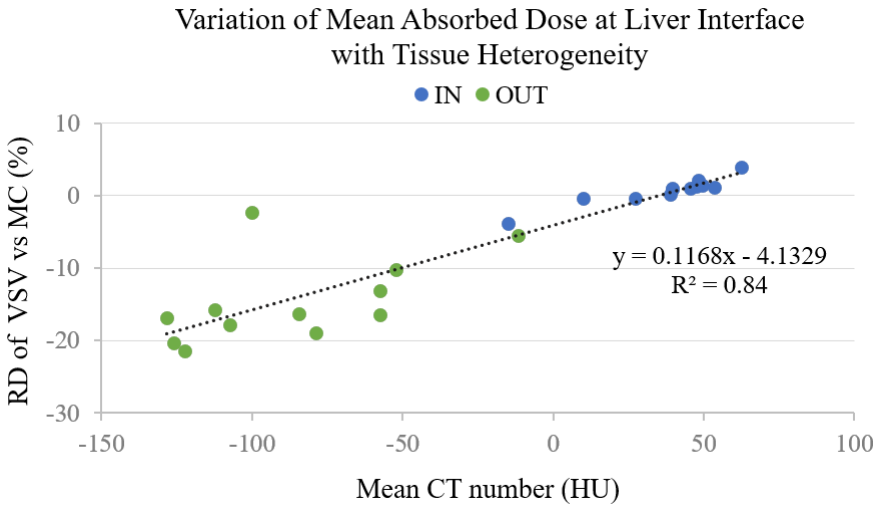

Figure 6.5: Relative difference between the mean absorbed dose in VSV- and MC-ADDs within the IN and OUT volumes against the mean HU within the same volumes.

To compare dosimetry results on a voxel level at the liver interface, a 1D profile was selected for Patient 2 crossing lung, normal liver and tumor tissue. Figure 6.6 shows a cross-sectional view of the PET/CT image for Patient 2 treatment verification and the selected 1D profile. CT image allows to visualize tissue heterogeneity at the liver interface. PET image reveals high activity in the interface of the liver and the surrounding tissues.

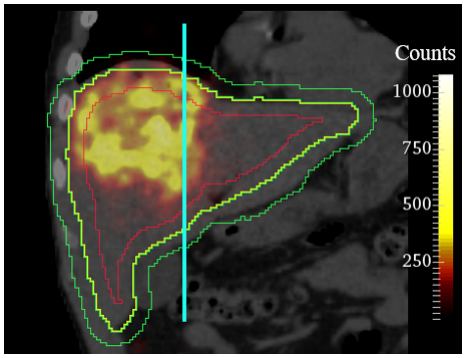

Figure 6.6: Cross-sectional view of the PET/CT image for Patient 2 treatment verification. PET image scale is displayed in counts. Outlines of IN and OUT volumes are shown in red and green, respectively. The selected 1D profile is shown in blue.

Figure 6.7 plots the CT numbers of Patient's 2 verification CT image and absorbed dose in VSV- and MC-ADDs for voxels within the selected 1D profile. A good agreement between VSV- and MC-ADDs is observed, except within voxels 1 to 17 where absorbed dose is higher in MC-ADDs than in VSV-ADDs with a maximum absolute deviation of 27.3 Gy. These voxels are associated to lung tissue and CT numbers below -500 HU.

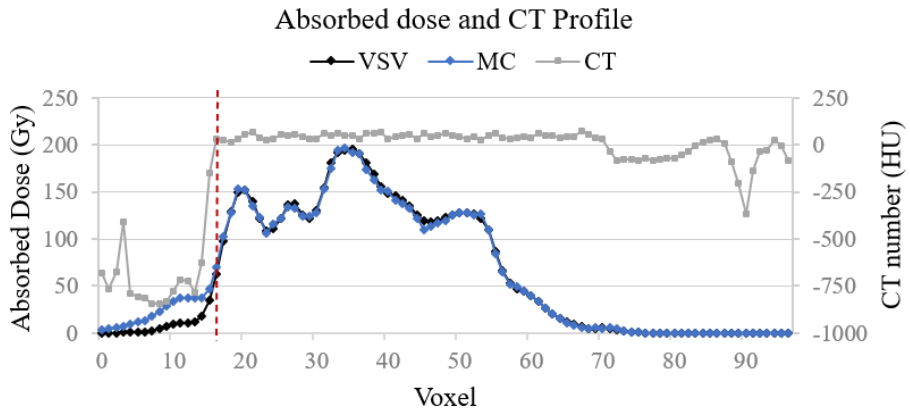

Figure 6.7: VSV-ADD, MC-ADD and CT profile selected for patient 2 treatment verification.

6.2 Comparison of Planning and Verification ADDs

6.2.1 Voxelwise Agreement and Correlation within the NLV and PTV

Table 6.8 lists the γ-index, ICC and PCC for the voxelwise comparison between planning and verification ADDs obtained with VSV and MC dosimetry methods within the NLV and PTV. The key observations are listed below.

Table 6.8: γ-index (test conditions: DD = 10 %; DTA = 10 mm), ICC and PCC of the voxelwised comparison between planning and verification VSV- and MC-ADDs within the NLV and PTV.

		γ-index PR (%)			ICC			PCC		
VOI	**Patient**	**VSV**	**MC**	**Diff**	**VSV**	**MC**	**Diff**	**VSV**	**MC**	**Diff**
NLV	1	88.8	89.2	-0.4	0.538	0.538	0.000	0.547	0.545	0.002
	2	97.2	97.2	0.0	0.296	0.297	0.001	0.299	0.299	0.000
	3	97.7	97.7	0.0	0.688	0.685	-0.003	0.696	0.693	0.003
	4	100.0	100.0	0.0	0.695	0.693	-0.001	0.768	0.765	0.003
	5	99.7	99.7	0.0	0.538	0.542	0.005	0.568	0.574	-0.006
	6	96.0	96.1	-0.1	0.659	0.658	-0.001	0.046	0.046	0.000
	Median	97.5	97.5	0.0	0.600	0.600	0.000	0.558	0.560	0.002
PTV	1	98.5	98.5	0.0	0.700	0.706	-0.006	0.766	0.765	0.001
	2	93.1	93.1	0.0	0.044	0.044	0.000	0.070	0.069	0.001
	3	97.7	97.8	-0.1	0.739	0.736	-0.003	0.743	0.740	0.003
	4	100.0	100.0	0.0	0.406	0.395	-0.011	0.506	0.496	0.010
	5	90.8	90.9	-0.1	0.533	0.530	-0.003	0.597	0.597	0.000
	6	85.3	85.7	-0.4	0.094	0.092	-0.002	-0.002	-0.002	0.000
	Median	95.4	95.5	0.1	0.470	0.463	0.007	0.552	0.547	0.005

- **For both dosimetry methods:** the median γ-index PR was higher than 90% within both VOIs, considering the 10%/10mm test condition; the median ICC within the NLV and PTV were higher than or equal to 0.600 and 0.463, respectively; and the median PCC within the NLV and PTV were higher than or equal to 0.558 and 0.547. These results indicate that, despite showing poor or fair voxelwise agreement and correlation, treatment planning quality quantified by γ-index is good. This is true especially taking into account the specified 10%/10mm combined test criterion and the spatial resolution of SPECT (no better than 6-8 mm) and PET (around 5 mm) systems.

- **For all patients:** the absolute difference between the γ-index, ICC and PCC on the voxelwised comparison between planning and verification ADDs obtained with VSV and MC dosimetry methods were below 0.4, 0.01, and 0.01 respectively. These results indicate similar agreement and correlation between planning and verification ADDs obtained with the two dosimetry methods.

6.2.2 Global Agreement and Correlation within the NLV and PTV

Table 6.9 lists ICC and PCC between mean absorbed doses computed in planning and verification ADDs obtained with each dosimetry method within the NLV and PTV. For both dosimetry methods, excellent correlation was found within both VOIs (PCC

> 0.90), excellent agreement was found within the NLV (ICC > 0.97), and moderate agreement was found within the PTV (ICC > 0.73). Overall, better global agreement and correlation was found between planning and verification ADDs in comparison to the voxelwise agreement and correlation.

Table 6.9: ICC and PCC between mean absorbed dose in planning and verification ADDs within the NLV and PTV obtained with VSV and MC dosimetry methods.

	ICC			PCC		
VOI	**VSV**	**MC**	**Diff**	**VSV**	**MC**	**Diff**
NLV	0.974	0.977	0.003	0.976	0.978	-0.002
PTV	0.738	0.739	0.001	0.905	0.907	-0.002

Figure 6.8 plots mean absorbed dose in planning ADDs against that in verification ADDs within the NLV and PTV and for both dosimetry methods. Equivalent correlation was found for both dosimetry methods within the same VOI. Correlation between planning and verification ADDs was better within the NLV (R^2 = 0.95 in VSV-ADDs; R^2 = 0.96 in MC-ADDs) than within the PTV (R^2 = 0.82 in VSV- and MC-ADDs). In addition, the mean absorbed dose within the PTV was higher in verification than in planning ADDs, while within the NLV it was similar in verification and planning ADDs.

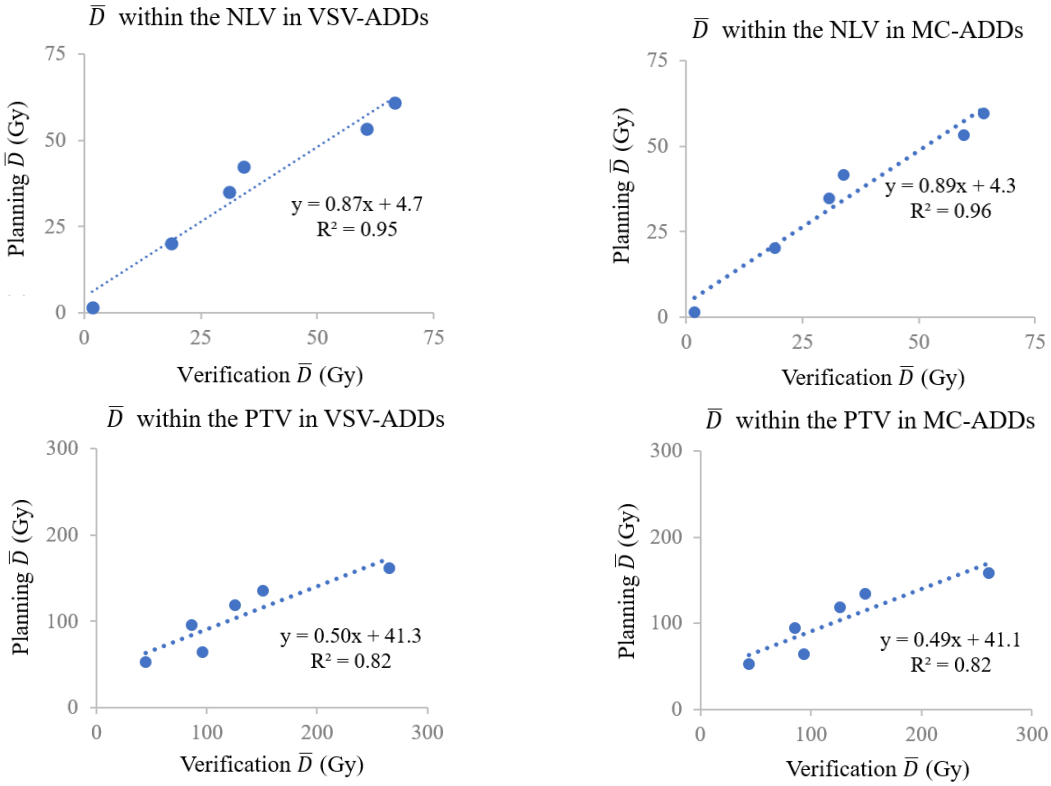

Figure 6.8: Mean absorbed dose in planning ADDs against that in verification ADDs obtained with VSV and MC dosimetry methods within NLV and PTV.

Chapter 7

Discussion

7.1 Stoichiometric Calibration of HU to Tissue Parameters

7.1.1 Converting HU to Mass Density

The continuous poly-line calibration of HU to mass density was obtained with a good median accuracy of 0.004 g/cm^3, considering standard ICRP tissues. These results are equivalent to the results obtained in my reference study presented by Schneider *et al.* [99].

The standard liver tissue lies in the calibration poly-line in alignment with *Muscle/General* RT, which represents all soft tissues. Moreover, the mass density of *Muscle/General* RT is similar to that of the uniform soft tissue assumed in VSV dosimetry ($RD = -0.9\%$). Such results indicated early on in this work that a similar mass density within patient's NLV and PTV to that of the *Muscle/General* RT would only yield small differences between VSV- and MC-ADDs due to tissue's mass density heterogeneity.

7.1.2 Converting Mass Density to Chemical Composition

The calibration of HU to chemical composition resulted in 19 bins of constant chemical composition and yielded maximum absolute differences of less than 4% for every element comparing to standard ICRP tissues, excluding carbon (Δ=37.01%) and oxygen (Δ=35.95%). The impact of intra-variations between element weights of carbon and oxygen on dosimetry results is expected to be negligible because the electron density of these elements is similar [99]. These results are equivalent to the results obtained in my reference study presented by Schneider *et al.* [99].

Comparing the chemical composition of the uniform soft tissue assumed in VSV dosimetry to that of *Muscle/ General* bin, the element-wise absolute differences are smaller than 1%, except again for carbon (Δ=8.07%) and oxygen (Δ=7.33%). Comparing the chemical composition of the *Muscle/ General* RT with the adjacent RTs (*Adipose/Marrow* and *Miscellaneous* RTs), the relative difference of each elemental weight is smaller than

2% for all elements, except for carbon and oxygen. Such results indicated early on in this work that the calibration of mass density within the NLV and PTV mostly in the range of *Muscle/ General* bin would only yield small variations between VSV- and MC-ADDs due to tissue's chemical composition heterogeneity.

7.2 Tissue heterogeneity within the NLV and PTV

7.2.1 Mass Density Heterogeneity

Mass density variations within the NLV and PTV showed to be rather small (Figure 5.4). First, the small ranges of mean mass density within patients' NLV and PTV ($\rho_{NLV}\ \epsilon\ [1.017; 1.074]$; $\rho_{PTV}\ \epsilon\ [1.028; 1.069]$) indicate a high level of *inter-personal* liver and tumor density homogeneity. Second, the small maximum IQRs of mass density within each patient' NLV and PTV (maximum IQR_{NLV} = 0.018 g/cm^3 ; maximum IQR_{NLV} = 0.016 g/cm^3) indicate a high level of *intra-personal* liver and tumor density homogeneity. Such ranges are aligned with reference values: (1) a reference study indicated a range of [1.017; 1.077] g/cm^3 for liver mass density in patients with a variety of pathologies [74], and (2) a reference study recognized liver tumours as iso-density masses [75].

Overall, the relative differences between the homogeneous mass density defined for the simulation of the VSV kernel (ρ = 1.04 g/cm^3) and the mean mass density obtained after the HU calibration within all patient's NLV and the PTV (ρ_{NLV} = 1.051 g/cm^3; ρ_{PTV} = 1.046 g/cm^3) are -1.0% and -0.6%, respectively. These results indicate that the homogeneous tissue mass density defined for VSV dosimetry is a good approximation of the liver and tumour tissues, and variations between VSV-ADDs and MC-ADDs due to tissue's mass density heterogeneity should be negligible.

7.2.2 Chemical Composition Heterogeneity

Most voxels within the NLV and PTV are assigned to the *Muscle/General* RT according to the calibration poly-line of HU to mass density, as the median percentages of voxels assigned to the *Muscle/General* RT are 83.3% and 94.3%, respectively (Tables 5.4 and 5.4). These results indicate that the homogeneous chemical composition defined in VSV dosimetry is a good approximation of the real liver and tumor tissues, and variations between VSV- and MC-ADDS due to tissue's chemical composition heterogeneity should be negligible.

7.3 Comparison of VSV- and MC-ADDs

This section discusses the results obtained on the comparison of ADDs. First, the feasibility of MC-GATE dosimetry in RE clinical practice is discussed, according to the duration of MC-GATE simulations. Second, the agreement and correlation of VSV- and MC-ADDs are analysed to assess the accuracy of VSV dosimetry compared to MC-GATE dosimetry. Third, the agreement and correlation of planning and verification ADDs obtained with each dosimetry method are discusses to assess the treatment planning quality of VSV dosimetry compared to MC-GATE dosimetry. Finally, the relevance of introducing fully personalized MC-GATE dosimetry in the clinical practice for RE optimization is discussed.

7.3.1 Feasibility of MC Dosimetry in Clinical Practice

7.3.1.1 Variables Influencing the Duration of MC-GATE Simulations

VSV dosimetry was performed in a just few seconds, while MC-GATE dosimetry took on average an entire day using the same laptop (Table 6.1). The available computational power (Table 4.5) limited the speed of MC-GATE simulations. A higher computational power could have lowered the duration of simulations to a few hours or even a few minutes, benefiting the feasibility of MC-GATE dosimetry in RE clinical practice schedule.

In addition to a rather long average duration, MC-ADD simulations required from 50×10^6 to 250×10^6 primary particles to achieve the desired mean statistical uncertainty within each patient's PTV (Table 6.1). Such wide range of primary particles is related to three variables changing between patients or even between treatment stages:

1. **PTV size:** a larger PTV includes more voxels and thus a higher total number of primary particles is necessary to generate the same number of primary particles per voxel, assuming a constant activity distribution. As a result, to achieve the same mean statistical uncertainty within the PTV, a higher number of simulated primary particles is required for larger PTVs. For example, Patient 2 has the largest PTV and the longest simulation times.

2. **Non-uniform activity distribution:** a higher ratio of total activity within the PTV (A_{PTV}) to the total activity within the box volume (A_{box}) yielded lower simulation times because more primary particles were generated within the PTV for the same number of simulated primary particles. For example, $A_{PTV}/A_{box} = 0.75$ in the ADD with the lowest simulation time (Patient 5 treatment verification), whereas

A_{PTV}/A_{box} = 0.66 in the ADD with the highest simulation time (Patient 2 treatment planning).

3. **Activity in the FMs:** a high activity in FMs yielded higher simulation times if FMs were not cropped from the original SPECT or PET images (i.e. if they are present within the box volume) because activity in FMs decreased A_{PTV}/A_{box}. For example, in the ADD with the second longest simulation time (Patient 4 treatment verification), voxels associated to FMs have activity values 100 times higher than voxels within the PTV.

In RE dosimetry stages, the PTV size and the non-uniform activity distribution cannot be changed. Only the activity in FMs could have been optimized in this work to decrease the required number of primary particles for each ADD simulation and, hence, the average simulation time. FMs are actually removed from patient's skin after the imaging process, which takes less than an hour. Scaling activity within FMs in a linear fashion with activity within the RWLV does not represent the real activity distribution overtime, as MSs are permanently trapped within tissues[1]. Therefore, to reduce the duration of MC-GATE dosimetry simulations in future work, voxels associated to FMs in SPECT or PET images could be segmented and assigned to null values.

7.3.1.2 MC-GATE Dosimetry in RE Clinical Practice Schedule

An example of an RE clinical schedule employing VSV dosimetry followed at CCU-FC was described in section 3.3.6. To fit MC-GATE dosimetry in such clinical schedule, MC-GATE dosimetry simulation should be completed by the end of day 3 of week 1. However, the input of MC-GATE dosimetry (i.e., processed SPECT/CT images) is only ready at the end of day 2 of week 1. Thus, the time window to perform MC-GATE dosimetry is around 24 hours.

MC-GATE dosimetry simulations of patient-specific ADDs took on average 24.9 hours [min = 8.9 h; max = 47.2 h] and can be left running overnight from day 2 to day 3 (Table 6.1). The following calibration step on MATLAB can be performed in a few minutes. Thus, MC-GATE dosimetry is feasible for some - but not all - RE patients using a low computational power. Most NM clinics, including CCU-CF, dispose of powerful computers that could boost the speed of MC-GATE dosimetry simulations. For that reason, MC-GATE dosimetry was considered feasible in RE clinical practice schedule.

[1] The activity in FMs, even if scaled as if they were permanent, has a week or null impact in ADDs within the NLV or PTV for two reasons: first, FM are applied on patients' skin surface, i.e. a few cm away from the VOIs; second, the range of ^{90}Y beta particles in tissues is only around 11 mm and secondary Bremsstrahlung photons may be neglected.

7.3.2 Accuracy of VSV Dosimetry within NLV and PTV

7.3.2.1 Voxelwise Agreement and Correlation

Based on the voxelwise BAPs of absorbed dose in matching voxels in VSV- and MC-ADDs (Figure 6.2), the behaviour of the voxelwise relative difference between VSV- and MC-ADDs as a function of the mean value is explained below:

1. **For low absorbed dose voxels**, the relative difference was found to be large and symmetric, revealing the random nature of MC simulations. GATE does not generate a statistically significant amount of primary particles at voxels with low activity in a *voxelized source*. As a result, the output absorbed dose in low activity voxels has a random deviation (noise) from the true value. The poor dosimetry accuracy in low absorbed dose voxels only weakly impacts the global dosimetry accuracy within the NLV and PTV, especially because the deviations are random.

2. **For high absorbed dose voxels**, the relative difference converged to values similar to the median voxelwise relative difference and close to 0%. These small median relative difference are related to the small tissue heterogeneity considered for MC-ADDs compared to the homogeneous soft tissue assumed for VSV-ADDs. For example, the voxelwise median relative differences between VSV- and MC-ADDs in Patient 1 treatment planning were 4.2% and 3.3% within the NLV and PTV, respectively. Simultaneously, the relative differences between the homogeneous mass density assumed in VSV dosimetry ($\rho = 1.04$ g/cm^3) and median mass densities calibrated in MC dosimetry ($\rho_{NLV} = 1.089$ g/cm^3; $\rho_{PTV} = 1.069$ g/cm^3) were -4.5% and -2.7% within the NLV and PTV, respectively. This suggests that the lower median mass density assumed in VSV-ADDs explain the higher absorbed dose in VSV-ADDs [2], according to Equation 2.7.

Overall, the voxelwise agreement and correlation between VSV- and MC-ADDs within the NLV and PTV was excellent (ICC and PCC > 0.99 for all features within both VOIs, see Table 6.2). These results indicated that VSV dosimetry is accurate within the NLV and PTV on the voxelwise level.

[2] Note that this inverse relationship is not observed in a linear fashion because other variables influence the voxelwise median relative difference of absorbed dose between VSV-ADDs and MC-ADDs, such as the chemical composition of tissues, outliers in the heterogeneity distribution and ADDs itself. Outliers in heterogeneity distribution are associated to voxels with low HU within the NLV that are calibrated to lower mass density values in MC dosimetry. As a result, absorbed dose is higher in MC-ADD than in VSV-ADD, according to Equation 2.7. Low HU voxels are mostly found close to the interface of the liver with the surrounding tissues and correspond to voxels already located totally or partially outside the real liver but that were selected by the NM physician as within the WLV. These outliers can strongly influence the median relative difference of absorbed dose if they are in close proximity with high activity voxels, because the absolute deviations in absorbed dose between VSV- and MC-ADDs are greater.

7.3.2.2 Global Agreement and Correlation

Excellent agreement and correlation was found between DVHs, mean absorbed dose and EUBED computed for VSV- and MC-ADDs within the NLV and PTV (ICC and PCC > 0.99 for all features within both VOIs, see Tables 6.2, 6.3, 6.5). Equivalent agreement and correlation between mean absorbed dose and EUBED computed for VSV- and MC-ADDs was found. These results indicate that VSV dosimetry is accurate on a global level of VOIs.

Slightly higher mean absorbed doses and EUBEDs were found in VSV-ADDs. The median relative difference between the mean absorbed dose and EUBED computed for VSV- and MC-ADDs within the NLV and PTV were 0.4% and 1.1%, respectively (Table 6.5). Again, the higher mean absorbed dose and EUBED computed for VSV-ADD are related to the small tissue heterogeneity considered within the NLV and PTV for MC-ADDs compared to the homogeneous soft tissue assumed for VSV-ADDs. Here, the relative differences between the homogeneous mass density assumed in VSV-ADDs (ρ = 1.04 g/cm^3) and the mean mass densities calibrated in MC-ADDs (ρ_{NLV} = 1.051 g/cm^3; ρ_{PTV} = 1.046 g/cm^3) were -1.0% and -0.6% within the NLV and PTV, respectively. Again, according to Equation 2.7, a lower mass density assumed in VSV dosimetry explains the higher mean absorbed dose in VSV-ADDs.

7.3.3 Accuracy of VSV Dosimetry at Liver Interface with Surrounding Tissues

At the liver interface with surrounding tissues, VSV- and MC-ADDs were compared and tissue heterogeneity was quantified (Tables 6.6 and 6.7):

1. **Within the IN volume:** a small and positive median relative difference between the mean absorbed dose computed for VSV- and MC-ADDs (1.0%) reinforces the excellent agreement within the WLV, even at liver interface voxels. This is explained by the short range of ^{90}Y beta particles mostly located within the WLV. These results indicate that tissue heterogeneity outside the WLV can only weakly impact ADDs within WLV.

2. **Within the OUT volume:** a large negative median relative difference between the mean absorbed dose computed for VSV- and MC-ADDs (-16%) shows poor agreement immediately outside the WLV. This is explained by a significant tissue heterogeneity outside the WLV. Within the OUT volume, the mean CT number is 5 times lower than within the IN volume because it includes a large portion of lung tissue. Thus, low CT numbers are calibrated to lower mass density for MC-GATE

dosimetry, explaining the higher mean absorbed dose in MC-ADDs according to Equation 2.7.

A good correlation between the relative difference of the mean absorbed dose computed for VSV- and MC-ADDs and the mean CT number within the IN and OUT volumes ($R^2 = 0.84$ in Figure 6.5) suggests once again that variations between VSV- and MC-ADDs are associated to tissue heterogeneity. Moreover, it is evident that all patients have a similar mean CT number within the IN volume, while there is a wider spread of the mean CT number within the OUT volume.

The 1D profile of VSV- and MC-ADDs in Figure 6.7 showed an excellent agreement between the ADDs except at voxels associated to lung tissue. Actually, absorbed dose in voxels 17 to 1 decreased continuously but at a slower rate in MC-ADDs than in VSV-ADDs. The higher absorbed doses at lung voxels for MC-ADDs comparing to VSV-ADDs is explained by the lower mass density of lung tissues calibrated in MC dosimetry compared to the homogeneous mass density of soft tissues assumed in VSV dosimetry. These results suggest that VSV dosimetry is *not* accurate in lung voxels at liver-lung interface, in alignment with Auditorie *et al.* investigations [93].

Despite an evident deviation between 1D profiles of VSV- and MC-ADDs at lung voxels, no absorbed dose interface behaviour was observed at the liver-lung interface, i.e. there was not a clear build-up or discontinuity of absorbed dose at lung voxels close to the liver interface. As proven in controlled conditions in Appendix C, the absence of a liver interface behaviour in RE is due to the null or very low amount of ^{90}Y – MS outside the WLV, and the short range of ^{90}Y beta particles in tissues.

7.3.4 Quality of Treatment Planning with VSV Dosimetry

Poor and fair voxelwise agreement and correlation was found within the NLV and PTV for both dosimetry methods (Table 6.8). Such results are likely related to the poor spatial resolution of SPECT (no better than 6 to 8 mm) and PET (5mm) systems, which is larger than the voxel size employed in dosimetry calculation (2.21 mm). A good treatment planning quality was quantified by the γ-index using the 10%/10 mm combined test criteria. Moreover, good to excellent agreement and correlation was reached between the mean absorbed dose in planning and verification ADDs within the NLV and PTV (Table 6.9). These results indicate that the predictive power of planning ^{99m}Tc – MAA SPECT images for the verification ^{90}Y – MS PET images is only fair on the voxelwise level, but it is good on a global level of the NLV and PTV.

More importantly, equivalent agreement and correlation was found between planning and verification ADDs obtained with both dosimetry methods (Tables 6.8 and 6.9).

These results suggest that treatment planning quality with VSV dosimetry is as good as that with MC-GATE dosimetry.

7.3.5 Relevance of MC Dosimetry in the Clinical Practice

On one hand, the results presented in this work proved (1) an excellent VSV dosimetry accuracy within the homogeneous NLV and PTV compared to the gold standard MC-GATE dosimetry, and (2) an equivalent treatment planning quality with both dosimetry methods. The excellent agreement and correlation between MC-GATE and VSV dosimetry methods suggests that both dosimetry methods would yield an equivalent optimum activity of ^{90}Y – MS in RE optimization, which is the end goal of RE dosimetry. Therefore, introducing MC-GATE dosimetry in the clinical practice is not relevant to prescribe the optimum activity of ^{90}Y – MS based only on absorbed doses within the NLV and PTV.

On the other hand, this work showed a poor agreement between VSV- and MC-ADDs at the liver interface with surrounding tissues. In particular, higher absorbed dose values were found for MC-ADDs in lung voxels at the liver interface. Therefore, introducing MC-GATE dosimetry in the clinical practice is relevant to understand possible toxic side-effects in lungs and other heterogeneous organs-at-risk, contributing to increase RE patients' overall survival.

Chapter 8

Conclusion

Current dosimetry guidelines for RE optimization are noncompliant with EURATOM directives requiring personalized dosimetry within target and non-target VOIs. The research presented in this work aimed to (1) assess the *accuracy* of VSV dosimetry - an advanced semi-personalized method that does not tissue heterogeneity - compared to gold standard MC dosimetry, and (2) evaluate the *relevance* and *feasibility* of introducing MC dosimetry in clinical practice to optimize RE. This final chapter gathers key findings of this research and highlights opportunities for future work.

8.1 Key Findings

This work contributed to the NM community by providing *open-source* GATE scripts to perform MC dosimetry for RE optimization. A major effort was made to tailor MC-GATE dosimetry simulations to RE. Particularly, configuration of physics set-up was relevant to increase the speed of simulations without compromising dosimetry accuracy. Most MC simulations fitted within the 24 hours window available in the clinical schedule for VSV dosimetry, despite the low computational power employed. Hence, MC-GATE dosimetry was considered *feasible* in clinical practice schedule of VSV dosimetry.

Within the rather homogeneous NLV and PTV, the comparison of VSV- and MC-ADDs showed excellent agreement and correlation between the two dosimetry methods at the voxel and macroscopic levels. These results validated the excellent *accuracy* of VSV dosimetry to optimize the activity of ^{90}Y – MSs considering only absorbed doses within the NLV and PTV. Moreover, equivalent agreement and correlation was found within these VOIs between planning and verification obtained with each dosimetry method, assuring that treatment planning quality of VSV dosimetry is equivalent to that of MC dosimetry.

Within the heterogeneous liver interface with surrounding tissues, a significant underestimation of absorbed dose with VSV dosimetry was found at lung voxels. These results indicated that VSV dosimetry lacks accuracy at the liver-lung interface due to a lower mass density of lungs compared to soft tissues. Dosimetry accuracy in lungs is paramount to investigate possible toxic side-effects, ensure treatment safety and increase

patients' overall survival. Therefore, MC dosimetry was considered *relevant* to optimize the activity of ^{90}Y – MSs considering the absorbed dose in lungs.

All in all:

While VSV was found accurate within the NLV and PTV, MC-GATE dosimetry was considered feasible in the clinical practice schedule and relevant in lungs to avoid toxic side-effects, ensure treatment safety and increase patients' overall survival.

8.2 Suggestions for Future Work

Further work is necessary to investigate the relevance of MC dosimetry in RE based on retrospective clinical data. Arising from the research conducted in this work, some suggestion for future work are described below:

- **Computational power:** only a personal laptop was available due to COVID-19 restrictions, limiting the speed of MC-GATE dosimetry simulations. Three solutions can be employed in future work: (1) the use of a more powerful (and expensive) computer, (2) the use of cluster-based parallel computing, and (3) the use of a cloud environment, i.e., a set of computing resources offered through internet as a pay-per-usage service [110], [111].
- **Clinical dataset size:** this study inclues data from six RE patients. Future work should include a larger clinical dataset with a wider range of RE patients, i.e. with difference distributions of ^{90}Y – MS and tissue heterogeneity.
- **Image cropping:** images in the clinical dataset include only a short portion of lung base at lung-liver interface. This work revealed significant variations between VSV- and MC-ADDs it lung voxels close to the liver-lung interface, but the impact of such variations within the whole lungs volume could not be quantified. Future work could include the comparison between the mean absorbed dose within the lungs volume computed in VSV- and MC-ADDs to better understand toxic side-effects in RE patients.
- **Dosimetry voxel size:** VSV- and MC-ADDs were computed with a single voxel size. Future work could investigate the use of different voxel sizes in dosimetry calculations, which might impact the relative accuracy of VSV- AND MC-ADDs and the simulation time of MC-ADDs.
- **Interface of PTV with NLV:** small tissue heterogeneity at the interface of PTV with NLV might reduce the accuracy of VSV dosimetry compared to MC dosimetry.

Future work could compare VSV- and MC-ADDs to assess the accuracy of VSV dosimetry at this interface.

- **Dosimetry automatizing:** for each RE patient, one MATLAB script was developed to obtain VSV- and MC-ADDs and one GATE script was developed to simulate the uncalibrated ADDs. Most of scripts' lines were common to all patients, except for the definition of personalized dosimetry input variables. Thus, after developing the first patient's scripts, only the input images, segmentation and numeric values (LSF, R, AA) were manually changed to produce other patients' scripts. These manual changes have a high probability of error. Future work could include the development of a user-friendly application that automatically computes ADDs after uploading personalized dosimetry input variables.

8.3 Roadmap for Personalized Dosimetry in Radioembolization

While RE emerges as an innovative, safe and efficient therapy for unresectable liver tumors, a lot of research is still required to comply with EURATOM directives for personalized dosimetry. Only MC simulations are capable to fully consider patient-specific tissue heterogeneity in RE dosimetry, but they require high computation power. MC dosimetry is already widely used in EBRT treatment planning and RE should follow the same path, designing similar workstations with high computational power for NM. Figure 8.1 suggests a roadmap for future work to implement MC dosimetry in RE clinical practice, which is described below in more detail.

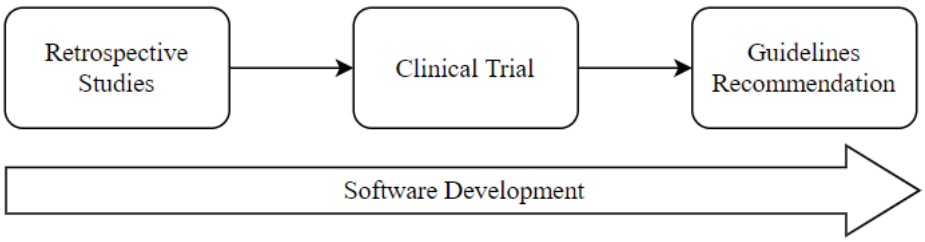

Figure 8.1: Suggested roadmap to implement MC dosimetry in RE clinical practice.

Larger *retrospective studies* should validate the results of this work and further investigate radiobiology measures in target and non-target VOIs (NLV, lungs, and other surrounding organs) for RE optimization. Such studies could justify launching a *clinical trial* to compare patients' overall survival employing the current dosimetry method, VSV dosimetry and MC dosimetry. If the clinical trial shows promising outcomes, clear *guidelines* should be created to (1) standardize MC dosimetry across all institutions, (2) set benchmarks for dosimetry accuracy, such as the physics cuts and statistical uncertainty, and (3) indicate how to optimize RE based on MC-ADDs and radiobiology measures.

Simultaneously to the work suggested above, MC dosimetry in RE represents a great opportunity for *software development*. As mentioned before, writing scripts for MC dosimetry becomes rather repetitive and prone to error between patients. For this reason, NM facilities would highly value a user-friendly interface to perform RE treatment planning and verification based on MC dosimetry. Ideally, such interface would allow to upload patients' relevant clinical data, automatically start a MC dosimetry simulation, and return the optimum activity of ^{90}Y – MSs based on the output MC-ADDs and radiobiology measurements within target and non-target VOIs.

Bibliography

[1] H. Sung *et al.*, "Global Cancer Statistics 2020: GLOBOCAN Estimates of Incidence and Mortality Worldwide for 36 Cancers in 185 Countries", *CA: A Cancer Journal for Clinicians*, vol. 71, no. 3, pp. 209–249, May 2021. DOI: 10.3322/caac.21660.

[2] F. Giammarile *et al.*, "EANM procedure guideline for the treatment of liver cancer and liver metastases with intra-arterial radioactive compounds", *Eur. J. of Nucl. Med. Mol. Imaging*, vol. 38, no. 7, pp. 1393–1406, Jul. 2011. DOI: 10.1007/s00259-011-1812-2.

[3] B. Sangro, M. Iñ arrairaegui, and J. I. Bilbao, "Radioembolization for hepatocellular carcinoma", *J. Hepatol.*, vol. 56, no. 2, pp. 464–473, Feb. 2012. DOI: 10.1016/j.jhep.2011.07.012.

[4] Le Conseil de l'union européenne, "Directive 2013/59/Euratom du Cons", *J. Off. I'Union Eur.*, vol. L13, no. 2, pp. 1–73, Jan. 2014.

[5] Decreto-Lei no 108/2018 de 3 dezembro, "Estabelece o regime jurídico da proteção radiológica, transpondo a diretiva 2013/59/euratom", *Diário da República*, 2018.

[6] M. Konijnenberg *et al.*, "EANM position paper on article 56 of the Council Directive 2013/59/Euratom (basic safety standards) for nuclear medicine therapy", *Eur. J. Nucl. Med. Mol. Imaging*, vol. 48, no. 1, pp. 67–72, Jan. 2021. DOI: 10.1007/s00259-020-05038-9.

[7] Boston Scientific, "Therasphere - Package Insert", Tech. Rep., 2020.

[8] E. Garin *et al.*, "Personalised versus standard dosimetry approach of selective internal radiation therapy in patients with locally advanced hepatocellular carcinoma (DOSISPHERE-01): a randomised, multicentre, open-label phase 2 trial", *The Lancet Gastroenterol. & Hepatol.*, vol. 6, no. 1, pp. 17–29, Jan. 2021. DOI: 10.1016/S2468-1253(20)30290-9.

[9] A. Dieudonné *et al.*, "Clinical feasibility of fast 3-dimensional dosimetry of the liver for treatment planning of hepatocellular carcinoma with 90Y-microspheres.", *J. Nucl. Med.*, vol. 52, no. 12, pp. 1930–7, Dec. 2011. DOI: 10.2967/jnumed.111.095232.

[10] R. Bastiaannet *et al.*, "The physics of radioembolization", *EJNMMI Phys.*, vol. 5, pp. 5–22, Nov. 2018. DOI: 10.1186/s40658-018-0221-z.

[11] F. B. Payolla, A. C. Massabni, and C. Orvig, "Radiopharmaceuticals for diagnosis in nuclear medicine: a short review", *Eclética Química J.*, vol. 44, no. 3, pp. 11–19, Jul. 2019. DOI: 10.268https://doi.org/10.26850/1678-4618eqj.v44.3.2019.p11-19.

[12] J. Magill and J. Galy, "Types of Radioactive Decay", in *Radiactivity Radionuclides Radiation*, Berlin: Springer, 2005, ch. 4, pp. 59–86.

[13] E. Podgorsak, A. Kesner, and P. Soni, "Basic Physics for Nuclear Medicine", in *Nuclear Medicine Physics - A Handbook for Teachers and Students*, D. L. Bailey *et al.*, Eds., Vienna: International Atomic Energy Agency, 2014, ch. 1, pp. 1–48.

[14] Brookhaven National Laboratory, *Nndc.bnl.gov*, 2019. [Online]. Available: https://www.nndc.bnl.gov/nudat2/getdecayscheme.jsp?nucleus=99TC&dsid=99tc%20it%20decay%20(6.0072%20h)&unc=nds (visited on 01/31/2021).

[15] ——, *Nndc.bnl.gov*, 2019. [Online]. Available: https://www.nndc.bnl.gov/nudat2/getdecayscheme.jsp?nucleus=90ZR&dsid=90y%20bM%20decay%20(64.05%20h)&unc=nds (visited on 01/31/2021).

[16] K. F. Eckerman *et al.*, *RADAR*, 2003. [Online]. Available: https://www.doseinfo-radar.com/RADARDecay.html (visited on 06/05/2021).

[17] D. Dance and G. C. Alm, "Interactions of Photons with Matter", in *Handbook of Radiotherapy Physics*, P. Mayles, A. Nahum, and J. Rosenwald, Eds., Boca Raton, FL: CRC Press, 2007, ch. 4, pp. 75–88.

[18] International Atomic Energy Agency, *Diagnostic Radiology Physics*. Vienna, 2014.

[19] H. Zaidi and B. Hasegawa, "Determination of the Attenuation Map in Emission Tomography", *J. of Nucl. Med.*, vol. 44, no. 2, pp. 291–315, Feb. 2003. [Online]. Available: https://jnm.snmjournals.org/content/44/2/291.

[20] M. F. L'Annunziata, "Beta Radiation", in *Radioactivity - Introduction and History*, M. F. L'Annunziata, Ed., 1st ed., Amsterdam: Elsevier Science B.V., 2007, pp. 119–140.

[21] M. J. Berger *et al.*, *ESTAR, PSTAR, and ASTAR: Computer Programs for Calculating Stopping-Power and Range Tables for Electrons, Protons, and Helium Ions (version 1.2.3)*. National Institute of Standards and Technology, 2005.

[22] R. Drzymala *et al.*, "Dose-volume histograms", *Int. J. of Radiat. Oncol.*, vol. 21, no. 1, pp. 71–78, May 1991. DOI: 10.1016/0360-3016(91)90168-4.

[23] National Research Council (US) and Institute of Medicine (US) Committee on State of the Science of Nuclear Medicine, "Nuclear Medicine Imaging in Diagnosis and Treatment", in *Advancing Nuclear Medicine Through Innovation*, Washington, D.C.: National Academies Press, 2007.

[24] H. A. Jacene *et al.*, "Advantages of Hybrid SPECT/CT vs SPECT Alone", *Open Med. Imaging J.*, vol. 2, no. 1, pp. 67–79, 2008. DOI: 10.2174/1874347100802010067.

[25] B. F. Hutton, "SPECT Imaging: Basics and New Trends", in *Handbook of Particle Detection and Imaging*, C. Grupen and I. Buvat, Eds. Berlin, Heidelberg: Springer Berlin Heidelberg, 2012, pp. 917–933.

[26] L. Livieratos, *Basic Principles of SPECT and PET Imaging*, I. Fogelman, G. Gnanasegaran, and H. van der Wall, Eds., Berlin, Heidelberg, 2012.

[27] P. Sprawls, *Physical principles of medical imaging*, English, 2nd ed. Madison, Wis.: Medical Physics Pub., 1995.

[28] M. A. King, T. Pan, and P. H. Pretorius, *Attenuation/Scatter/Resolution Correction: Physics aspects*, B. L. Zaret and G. A. Beller, Eds., Ames, 2010.

[29] M. Noori-Asl and A. Sadremomtaz, "Analytical image reconstruction methods in emission tomography", *J. of Biomed. Sci. and Eng.*, vol. 06, pp. 100–107, Jan. 2013. DOI: 10.4236/jbise.2013.61013.

[30] P. P. Bruyant, "Analytic and Iterative Reconstruction Algorithms in SPECT", *J. of Nucl. Med.*, vol. 43, no. 10, pp. 1343–1358, Oct. 2002. [Online]. Available: https://jnm.snmjournals.org/content/43/10/1343.long.

[31] G. Currie, J. Hewis, and S. Bushong, "Tomographic Reconstruction: A Nonmathematical Overview", *J. Med. Imaging and Radiat. Sci.*, vol. 46, no. 4, pp. 403–412, Dec. 2015. DOI: 10.1016/j.jmir.2015.07.007.

[32] T. Yokei, H. Shinohara, and H. Onishi, "Performance evaluation of OSEM reconstruction algorithm incorporating three-dimensional distance-dependent resolution compensation for brain SPECT: A simulation study", *Ann. of Nucl. Med.*, vol. 16, no. 1, pp. 11–18, 2002. DOI: 10.1007/BF02995286.

[33] S. C. Vaz *et al.*, "Nuclear medicine and molecular imaging advances in the 21st century", *Bri. J. of Radiol.*, vol. 93, no. 1110, p. 20 200 095, May 2020. DOI: 10.1259/bjr.20200095.

[34] S. Basu *et al.*, "Fundamentals of pet and pet/ct imaging", *Ann. N. Y. Acad. Sci.*, vol. 1228, no. 1, pp. 1–18, Jun. 2011. DOI: https://doi.org/10.1111/j.1749-6632.2011.06077.x.

[35] M. Lodge and E. Frey, "Nuclear Medicine Imaging Devices", in *Nuclear Medicine Physics*, Vienna: International Atomic Energy Agency, 2014, pp. 312–294.

[36] W. W. Moses, "Fundamental Limits of Spatial Resolution in PET", eng, *Nucl. Instruments Methods Phys. Res. Sect. A, Accel., Spectrometers, Detect. Assoc. Equip.*, vol. 648, S236–S240, Aug. 2011. DOI: 10.1016/j.nima.2010.11.092.

[37] E. Lin and A. Alessio, "What are the basic concepts of temporal, contrast, and spatial resolution in cardiac CT?", eng, *J. Cardiovasc. Comput. Tomogr.*, vol. 3, no. 6, pp. 403–408, Jul. 2009. DOI: 10.1016/j.jcct.2009.07.003.

[38] K. Blackham and L. Vidal, "Computed tomography", in *Encyclopedia of the Neurological Sciences (Second Edition)*, M. J. Aminoff and R. B. Daroff, Eds., Second Edition, Oxford: Academic Press, 2014, pp. 848–853.

[39] B. Vanderstraeten *et al.*, "Conversion of CT numbers into tissue parameters for Monte Carlo dose calculations: a multi-centre study", *Phys. Med. Biol.*, vol. 52, no. 3, pp. 539–562, Feb. 2007.

[40] S. St. James *et al.*, "Current Status of Radiopharmaceutical Therapy", *Int. J. Radiat. Oncol.*, vol. 109, no. 4, pp. 891–901, Mar. 2021. DOI: 10.1016/j.ijrobp.2020.08.035.

[41] M. Cremonesi *et al.*, "Radioembolisation with 90Y-microspheres: dosimetric and radiobiological investigation for multi-cycle treatment", *Eur. J. Nucl. Med. Mol. Imaging*, vol. 35, no. 11, pp. 2088–2096, Nov. 2008. DOI: 10.1007/s00259-008-0857-3.

[42] S. Banerjee, M. R. Ambikalmajan Pillai, and N. Ramamoorthy, "Evolution of tc-99m in diagnostic radiopharmaceuticals", *Semin. Nucl. Med.*, vol. 31, no. 4, pp. 260–277, Oct. 2001, Radiochemistry update. DOI: https://doi.org/10.1053/snuc.2001.26205.

[43] L. M. Kulik *et al.*, "Safety and efficacy of 90Y radiotherapy for hepatocellular carcinoma with and without portal vein thrombosis", *Hepatol.*, vol. 47, no. 1, pp. 71–81, Nov. 2007. DOI: 10.1002/hep.21980.

[44] M. A. Westcott *et al.*, "The development, commercialization, and clinical context of yttrium-90 radiolabeled resin and glass microspheres", *Adv.Radiat. Oncol.*, vol. 1, no. 4, pp. 351–364, Oct. 2016. DOI: 10.1016/j.adro.2016.08.003.

[45] M. Cremonesi *et al.*, "Radioembolization of Hepatic Lesions from a Radiobiology and Dosimetric Perspective", *Front. Oncol.*, vol. 4, p. 210, Aug. 2014. DOI: 10.3389/fonc.2014.00210.

[46] A. Aerts *et al.*, "Eanm position paper on the role of radiobiology in nuclear medicine", *Eur. J. Nucl. Med. Mol. Imaging*, vol. 48, pp. 3365–3377, Apr. 2021. DOI: 10.1007/s00259-021-05345-9.

[47] N. E. Bolus, "Basic Review of Radiation Biology and Terminology", *J. Nucl. Med. Technol.*, vol. 45, no. 4, pp. 259–264, Dec. 2017. DOI: 10.2967/jnmt.117.195230.

[48] J.-P. Pouget *et al.*, "Introduction to Radiobiology of Targeted Radionuclide Therapy", *Front. Med.*, vol. 2, no. MAR, p. 12, Mar. 2015, ISSN: 2296-858X. DOI: 10.3389/fmed.2015.00012.

[49] S. J. McMahon, "The linear quadratic model: usage, interpretation and challenges", *Phys. Med. Bio.*, no. 1, 01TR01, 2018. DOI: 10.1088/1361-6560/aaf26a.

[50] A. H. Elgazzar and N. Kazem, "Biological Effects of Ionizing Radiation", in *The Pathophysiologic Basis of Nuclear Medicine*, A. H. Elgazzar, Ed. Berlin, Heidelberg: Springer, 2006, pp. 540–548.

[51] N. Sharda *et al.*, "Radiation Resistance", in *Encyclopedia of Cancer (Second Edition)*, J. R. Bertino, Ed., Second Edi, New York: Academic Press, 2002, pp. 1–11.

[52] C. D. Willey, E. S.-H. Yang, and J. A. Bonner, "Interaction of Chemotherapy and Radiation", in *Clin. Radiat. Oncol.* L. L. Gunderson and J. E. Tepper, Eds., Amesterdam: Elsevier, 2016, pp. 63–79.

[53] L. Sibulesky, "Normal liver anatomy", *Clin. Liver Dis.*, vol. 2, no. S1, S1–S3, Mar. 2013. DOI: 10.1002/cld.124.

[54] J. Ozougwu, "Physiology of the liver", *Inter. J. Res. Pharm. Biosci.*, vol. 4, no. 8, pp. 13–24, Oct. 2017. [Online]. Available: https://www.researchgate.net/publication/320452275_Physiology_of_the_liver.

[55] Editors of Encyclopaedia Britannica, *Abdominal cavity*, 2017. [Online]. Available: https://www.britannica.com/science/abdominal-cavity.

[56] S. R. Abdel-Misih and M. Bloomston, "Liver Anatomy", *Surg. Clin. North Am.*, vol. 90, no. 4, pp. 643–653, Aug. 2010. DOI: 10.1016/j.suc.2010.04.017.

[57] UpToDate, *Functional Segments of the Liver*, 2011. [Online]. Available: https://somepomed.org/articulos/contents/mobipreview.htm?24/28/25033 (visited on 07/05/2021).

[58] P. Majno *et al.*, "Anatomy of the liver: An outline with three levels of complexity - A further step towards tailored territorial liver resections", *J. Hepatol.*, vol. 60, no. 3, pp. 654–662, Mar. 2014. DOI: 10.1016/j.jhep.2013.10.026.

[59] C. Couinaud, *Le foie; études anatomiques et chirurgicales*. French. Paris: Masson, 1957.

[60] International Agency for Reasearch on Cancer and Wold Health Organization, *Cancer Today: Data visualization tools for exploring the global cancer burden in 2020*, 2020. [Online]. Available: https://gco.iarc.fr/today (visited on 06/15/2021).

[61] A. Ananthakrishnan, V. Gogineni, and K. Saeian, "Epidemiology of Primary and Secondary Liver Cancers", *Sem. Interv. Radiol.*, vol. 23, no. 1, pp. 047–063, Mar. 2006. DOI: 10.1055/s-2006-939841.

[62] C. P. Chen, "Role of Radiotherapy in the Treatment of Hepatocellular Carcinoma", *J. Clin. Transl. Hepatol.*, vol. 7, no. 2, pp. 183–190, Jun. 2019. DOI: 10.14218/JCTH.2018.00060.

[63] P. R. Galle *et al.*, "EASL Clinical Practice Guidelines: Management of hepatocellular carcinoma", *J. Hepatol.*, vol. 69, no. 1, pp. 182–236, Jul. 2018. DOI: 10.1016/j.jhep.2018.03.019.

[64] CRA Medical Imaging, *Radioembolization Procedure*, 2020. [Online]. Available: https://www.craimaging.com/radioembolization-procedure/ (visited on 06/24/2021).

[65] A. Kennedy *et al.*, "Recommendations for radioembolization of hepatic malignancies using yttrium-90 microsphere brachytherapy: a consensus panel report from the radioembolization brachytherapy oncology consortium.", *Int. J. Radiat. Oncol.*, vol. 68, no. 1, pp. 13–23, May 2007. DOI: 10.1016/j.ijrobp.2006.11.060.

[66] P. Ferreira *et al.*, "Patient-specific gamma-index analysis to evaluate 99m Tc-MAA as a predictor for 90 Y glass microspheres liver radioembolisation dosimetry", *Comput. Methods Biomech. and Biomed. Eng. Imaging Vis.*, vol. 7, no. 5-6, pp. 583–589, Nov. 2019. DOI: 10.1080/21681163.2018.1501768.

[67] L. Demino *et al.*, "Comparison of the 90 y-labelled glass microspheres liver radioembolisation dosimetry with the estimated dosimetry obtained from pre-treatment 99m tc-maa spect images reconstructed with and without attenuation correction", *Comput. Methods in Biomech. and Biomed. Eng. Imaging & Vis.*, vol. 7, no. 5-6, pp. 651–659, Nov. 2019. DOI: 10.1080/21681163.2018.1542348.

[68] E. Garin *et al.*, "Clinical impact of 99mTc-MAA SPECT/CT-based dosimetry in the radioembolization of liver malignancies with 90Y-loaded microspheres", *Eur. J. Nucl. Med. Mol. Imaging*, vol. 43, no. 3, pp. 559–575, Mar. 2016. DOI: 10.1007/s00259-015-3157-8.

[69] K. H. Narsinh *et al.*, "Hepatopulmonary Shunting: A Prognostic Indicator of Survival in Patients with Metastatic Colorectal Adenocarcinoma Treated with 90 Y Radioembolization", *Radiol.*, vol. 282, no. 1, pp. 281–288, Jan. 2017. DOI: 10.1148/radiol.2016152100.

[70] D. Liu *et al.*, "The Limitations of Theoretical Dose Modeling for Yttrium-90 Radioembolization", *J. Vasc. Interv. Radiol.*, vol. 25, no. 7, pp. 1146–1147, Jul. 2014. DOI: 10.1016/j.jvir.2014.03.025.

[71] M. Lam, R. Salem, and E. Garin, "Abstract No. LB02 A global study of advanced dosimetry in the treatment of hepatocellular carcinoma with Yttrium-90 glass microspheres: analyses from the TARGET study", in *Journal of Vascular and Interventional Radiology*, vol. 32, 2021, S42. DOI: 10.1016/j.jvir.2021.03.096.

[72] N. Lanconelli, *Voxel dosimetry in Nuclear Medicine*, 2004. [Online]. Available: https://www.medphys.it/res_svoxel.htm (visited on 06/12/2021).

[73] N. Lanconelli *et al.*, "A free database of radionuclide voxel S values for the dosimetry of nonuniform activity distributions", *Physics in Medicine and Biology*, vol. 57, no. 2, pp. 517–533, Jan. 2012. DOI: 10.1088/0031-9155/57/2/517.

[74] B. A. Overmoyer, C. E. McLaren, and G. M. Brittenham, "Uniformity of liver density and nonheme (storage) iron distribution.", *Arch. Pathol. Lab. Med.*, vol. 111, no. 6, pp. 549–54, Jun. 1987. [Online]. Available: http://www.ncbi.nlm.nih.gov/pubmed/3579513.

[75] S. Hirota *et al.*, "Hyperdensity liver tumor on plain CT", *Nihon Igaku Hoshasen Gakkai zasshi. Nippon acta radiologica*, vol. 44, no. 12, pp. 1508–12, Dec. 1984. [Online]. Available: http://www.ncbi.nlm.nih.gov/pubmed/6099541.

[76] D. Plachouris *et al.*, "Clinical Evaluation of a Three-Dimensional Internal Dosimetry Technique for Liver Radioembolization with 90 Y Microspheres Using Dose Voxel Kernels", *Cancer Biother. Radiopharm.*, cbr.2020.4554, Mar. 2021. DOI: 10.1089/cbr.2020.4554.

[77] M. S. Lee *et al.*, "Whole-Body Voxel-Based Personalized Dosimetry: The Multiple Voxel S-Value Approach for Heterogeneous Media with Nonuniform Activity Distributions", *J. Nucl. Med.*, vol. 59, no. 7, pp. 1133–1139, Jul. 2018. DOI: 10.2967/jnumed.117.201095.

[78] G. Loudos *et al.*, "A radionuclide dosimetry toolkit based on material-specific Monte Carlo dose kernels", *Nucl. Med. Commun.*, vol. 30, no. 7, pp. 504–512, Jul. 2009. DOI: 10.1097/MNM.0b013e3283299a11.

[79] R. L. Harrison, C. Granja, and C. Leroy, "Introduction to Monte Carlo Simulation", in *AIP Conference*, 2010, pp. 17–21. DOI: 10.1063/1.3295638.

[80] S. Raychaudhuri, "Introduction to Monte Carlo simulation", in *Winter Simulation Conference*, IEEE, Dec. 2008, pp. 91–100. DOI: 10.1109/WSC.2008.4736059.

[81] International Atomic Energy Agency, "Medical Imaging", in *Diagnostic Radiology Physics*, M. Analoui, J. D. Bronzino, and D. R. Peterson, Eds., Vienna, Austria: CRC Press, Nov. 2012, ch. 2, pp. 11–32. DOI: 10.1201/b12939.

[82] E. Amato *et al.*, "Full monte carlo internal dosimetry in nuclear medicine by means of GAMOS", *J.Phys. Conf. Ser.*, vol. 1561, p. 012 002, Jun. 2020. DOI: 10.1088/1742-6596/1561/1/012002.

[83] M. Stabin *et al.*, "Radiation dosimetry in nuclear medicine", *Appl. Radiat. Isot.*, vol. 50, no. 1, pp. 73–87, Jan. 1999. DOI: 10.1016/S0969-8043(98)00023-2.

[84] S. Jan *et al.*, "GATE: a simulation toolkit for PET and SPECT", *Physics in Medicine and Biology*, vol. 49, no. 19, pp. 4543–4561, Oct. 2004. DOI: 10.1088/0031-9155/49/19/007.

[85] CERN, *Overview*, 2021. [Online]. Available: https://geant4.web.cern.ch/node/1.

[86] A. Milano *et al.*, "In Silico Validation of MCID Platform for Monte Carlo-Based Voxel Dosimetry Applied to 90Y-Radioembolization of Liver Malignancies", *Appl. Sci.*, vol. 11, no. 4, p. 1939, Feb. 2021. DOI: 10.3390/app11041939.

[87] E. E. Furhang *et al.*, "Implementation of a Monte Carlo dosimetry method for patient-specific internal emitter therapy", *Med. Phys.*, vol. 24, no. 7, pp. 1163–1172, Jul. 1997. DOI: 10.1118/1.598018.

[88] H. Yoriyaz, M. G. Stabin, and A. dos Santos, "Monte Carlo MCNP-4B-based absorbed dose distribution estimates for patient-specific dosimetry.", *J. Nucl Med.*, vol. 42, no. 4, pp. 662–9, Apr. 2001. [Online]. Available: http://www.ncbi.nlm.nih.gov/pubmed/11337557.

[89] S. Marcatili *et al.*, "Development and validation of RAYDOSE: a Geant4-based application for molecular radiotherapy", *Phys. Med. Biol.*, vol. 58, no. 8, pp. 2491–2508, Apr. 2013. DOI: 10.1088/0031-9155/58/8/2491.

[90] A. E. Besemer *et al.*, "Development and Validation of RAPID: A Patient-Specific Monte Carlo Three-Dimensional Internal Dosimetry Platform", *Cancer Biother. Radiopharm.*, vol. 33, no. 4, pp. 155–165, May 2018. DOI: 10.1089/cbr.2018.2451.

[91] J. Grimes, C. Uribe, and A. Celler, "JADA: A graphical user interface for comprehensive internal dose assessment in nuclear medicine", *Medical Physics*, vol. 40, no. 7, p. 072 501, Jun. 2013. DOI: 10.1118/1.4810963.

[92] N. A. A. Hashikin *et al.*, "Systematic investigation on the validity of partition model dosimetry for 90 Y radioembolization using Monte Carlo simulation", *Phys. Med. Biol.*, vol. 62, no. 18, pp. 7342–7356, Aug. 2017. DOI: 10.1088/1361-6560/aa7e5b.

[93] L. Auditore *et al.*, "Internal dosimetry for TARE therapies by means of GAMOS Monte Carlo simulations", *Phys. Med.*, vol. 64, pp. 245–251, Aug. 2019. DOI: 10.1016/j.ejmp.2019.07.024.

[94] S. M. Srinivas *et al.*, "Determination of Radiation Absorbed Dose to Primary Liver Tumors and Normal Liver Tissue Using Post-Radioembolization 90Y PET", *Front. Oncol.*, vol. 4, Oct. 2014. DOI: 10.3389/fonc.2014.00255.

[95] C. Chiesa *et al.*, "Radioembolization of hepatocarcinoma with 90Y glass microspheres: development of an individualized treatment planning strategy based on dosimetry and radiobiology", *Eur. J. Nucl. Med. Mol. Imaging*, vol. 42, no. 11, pp. 1718–1738, Oct. 2015. DOI: 10.1007/s00259-015-3068-8.

[96] E. Garin *et al.*, "Dosimetry Based on 99m Tc-Macroaggregated Albumin SPECT/CT Accurately Predicts Tumor Response and Survival in Hepatocellular Carcinoma Patients Treated with 90 Y-Loaded Glass Microspheres: Preliminary Results", *J. Nucl. Med.*, vol. 53, no. 2, pp. 255–263, Feb. 2012. DOI: 10.2967/jnumed.111.094235.

[97] P. Ferreira *et al.*, "Optimization of activity and absorbed doses calculation to target/tumor and normal liver volumes in patients submitted to yttrium-90 radioembolization with glass microspheres", *Phys. Med.*, vol. 32, p. 200, Sep. 2016. DOI: 10.1016/j.ejmp.2016.07.679.

[98] P. Ferreira *et al.*, "Gamma-index and dose-volume histograms (based on voxel dosimetry) to evaluate the predictive power of 99m Tc-MAA SPECT maps in comparison with post-radioembolization 90 Y PET maps", in *2017 IEEE 5th Portuguese Meeting on Bioengineering (ENBENG)*, IEEE, 2017, pp. 1–4. DOI: 10.1109/ENBENG.2017.7889428.

[99] W. Schneider, T. Bortfeld, and W. Schlegel, "Correlation between CT numbers and tissue parameters needed for Monte Carlo simulations of clinical dose distributions", *Phys. Med. Biol.*, vol. 45, no. 2, pp. 459–478, Feb. 2000. DOI: 10.1088/0031-9155/45/2/314.

[100] R. A. Rutherford, B. R. Pullan, and I. Isherwood, "Measurement of effective atomic number and electron density using an EMI scanner", *Neuroradiology*, vol. 11, no. 1, pp. 15–21, 1976. DOI: 10.1007/BF00327253.

[101] U. Schneider, E. Pedroni, and A. Lomax, "The calibration of CT Hounsfield units for radiotherapy treatment planning", *Phys. Med. Biol.*, vol. 41, no. 1, pp. 111–124, Jan. 1996. DOI: 10.1088/0031-9155/41/1/009.

[102] N. Kanematsu, T. Inaniwa, and M. Nakao, "Modeling of body tissues for Monte Carlo simulation of radiotherapy treatments planned with conventional x-ray CT systems", *Phys. Med. Biol.*, vol. 61, no. 13, pp. 5037–5050, Jul. 2016. DOI: 10.1088/0031-9155/61/13/5037.

[103] ICRP, "Adult Reference Computational Phantoms", *ICRP Publication 110. Ann. ICRP*, vol. 39, no. 2, 2009.

[104] H. B. Robert *et al.*, "Lung Density Changes With Growth and Inflation", *Chest*, vol. 148, no. 4, pp. 995–1002, Oct. 2015. DOI: 10.1378/chest.15-0264.

[105] M. Cristy and K. F. Eckerman, *Specific Absorbed Fractions of Energy at Various Ages from Internal Photons Sources*. Oak Ridge, Tennesse, 1987.

[106] P. Papadimitroulas *et al.*, "A dose point kernel database using GATE Monte Carlo simulation toolkit for nuclear medicine applications: Comparison with other Monte Carlo codes", *Med. Phys.*, vol. 39, no. 8, pp. 5238–5247, Aug. 2012. DOI: 10.1118/1.4737096.

[107] D. van der Merwe *et al.*, "Accuracy requirements and uncertainties in radiotherapy: a report of the International Atomic Energy Agency", *Acta Oncol.*, vol. 56, no. 1, pp. 1–6, Jan. 2017. DOI: 10.1080/0284186X.2016.1246801.

[108] D. Giavarina, "Understanding Bland Altman analysis", *Bioch. Med.*, vol. 25, no. 2, pp. 141–151, Jun. 2015. DOI: 10.11613/BM.2015.015.

[109] H. Li *et al.*, "Toward a better understanding of the gamma index: Investigation of parameters with a surface-based distance methoda)", *Med. Phys.*, vol. 38, no. 12, pp. 6730–6741, Nov. 2011. DOI: 10.1118/1.3659707.

[110] H. Miras *et al.*, "CloudMC: a cloud computing application for Monte Carlo simulation.", *Phys. Medicine Biol.*, no. 8, N125–33, Apr. 2013. DOI: 10.1088/0031-9155/58/8/N125.

[111] H. Miras *et al.*, "Monte Carlo verification of radiotherapy treatments with CloudMC", *Radiat. Oncol.*, vol. 13, no. 1, p. 99, Dec. 2018. DOI: 10.1186/s13014-018-1051-9.

[112] D. R. White *et al.*, "Report 44", *J. Int. Comm. Radiat. Units Meas.*, vol. os23, no. 1, NP–NP, Jan. 1989. DOI: 10.1093/jicru/os23.1.Report44.

[113] I. J. Chetty *et al.*, "Reporting and analyzing statistical uncertainties in Monte Carlo–based treatment planning", *Int. J. Radiat. Oncol.*, vol. 65, no. 4, pp. 1249–1259, Jul. 2006. DOI: 10.1016/j.ijrobp.2006.03.039.

Appendix A

Minimum Kinetic Energy Cut

A.1 Introduction

The set-up of physics in MC-GATE simulations can be customized with special cuts. Wider cuts increase the speed of MC-GATE simulations, and hence benefit the feasibility of MC-GATE dosimetry in RE clinical practice. This short investigation explores the use of a special cut for the simulation of ^{90}Y radiation in RE dosimetry: the *minimum kinetic energy* of a particle. This cut stops a particle that has less kinetic energy than the predefined *minimum kinetic energy* and locally deposits its energy. As a result, the particle's track is shortened and the simulation time decreases.

The *minimum kinetic energy* cut must be set carefully as it impacts dosimetry accuracy. Two scenarios are possible:

1. **Ideal scenario:** If the cut was undefined, a particle with less energy than the *minimum kinetic energy* would deposit its energy within the same voxel in the ADD where it is actually stopped by the cut. The same is true for secondary particles that could be generated. In other words, the track-length of a particle with *minimum kinetic energy* is shorter than the voxel size of ADDs. This scenario ensures dosimetry accuracy.
2. **Undesired scenario:** If the cut was undefined, a particle with less energy than the *minimum kinetic energy* could leave the voxel in the ADD where it is actually stopped by the cut and deposit its energy elsewhere, or it could produce secondary particles with sufficient energy to escape the voxel where the primary particle is stopped and equally deposit its energy elsewhere. In other words, the track-length of a particle with *minimum kinetic energy* is longer than the voxel size of ADDs. This scenario jeopardizes dosimetry accuracy.

This investigation aims to define the highest energy for the *minimum kinetic energy* cut that ensures dosimetry accuracy while achieving the lowest simulation time possible.

A.2 Methodology

In RE, ^{90}Y emits electrons with kinetic energy up to around 2280 keV. A small amount of these electrons produces more penetrating secondary photons. Thus, the track-lengths of both electrons and photons are relevant to set the *minimum kinetic energy* cut. In this investigation, the track-length of mono-energetic electrons and photons, ranging from 10 to 2280 keV, was estimated using the *Track-length Actor* returned by MC-GATE simulations.

In RE optimization, the accuracy of ADDs is most relevant within the PTV and NLV because most ^{90}Y – MSs are entrapped within these VOIs and the range of ^{90}Y radiation is rather short in soft tissues. Nevertheless, ADDs are also relevant at the liver interface with surrounding tissues, including lungs and bones, to assess possible toxic side-effects at organs-at-risk. In this investigation, mean track-lengths $\overline{L}$ were estimated for three standard materials: inflated lung, soft tissue and cortical bone. Table A.1 describes the mass density and chemical composition of each material.

Table A.1: Mass density and chemical composition of inflated lung [112], soft tissue [105] and cortical bone [112].

	Percent by weight (%)		
Element	**Infalted Lung**	**Soft tissue**	**Cortical bone**
H	10.3	10.454	4.72340
C	10.5	22.663	14.4330
N	3.1	2.490	4.1990
O	74.9	63.525	44.6096
Na	0.2	0.112	-
Mg	-	0.013	0.2200
Si	-	0.030	-
P	0.2	0.134	10.4970
S	0.3	0.204	3.1500
Cl	0.3	0.133	-
K	0.3	0.208	-
Ca	-	0.024	20.9930
Fe	-	0.005	-
Zn	-	0.003	0.01
Rb	-	0.001	-
Zr	-	0.001	-
Mass density (g/cm^3)	0.26	1.04	1.85

A.3 Results

Tables A.2 and A.3 display the mean track-length of mono-energetic electrons and photons in the three standard materials. Figure A.1 plots these results and compares them with the voxel size of ADDs in this work (2.21 mm).

Table A.2: Mean track-length of monoenergetic electrons in inflated lung, soft tissue and cortical bone.

	Electrons $\overline{L}$ (mm)		
Energy (keV)	**Inflated Lung**	**Soft tissue**	**Cortical Bone**
10	9.7×10^{-3}	2.4×10^{-3}	0.0×10^{-3}
20	3.3×10^{-2}	8.2×10^{-3}	5.1×10^{-3}
50	1.7×10^{-1}	4.1×10^{-2}	2.6×10^{-2}
100	5.6×10^{-1}	1.4×10^{-1}	8.6×10^{-2}
150	1.1×10^{0}	2.7×10^{-1}	1.7×10^{-1}
200	1.7×10^{0}	4.4×10^{-1}	2.7×10^{-1}
250	2.5×10^{0}	6.2×10^{-1}	3.9×10^{-1}
300	3.3×10^{0}	8.2×10^{-1}	5.1×10^{-1}
400	5.0×10^{0}	1.2×10^{0}	7.8×10^{0}
500	6.8×10^{0}	1.7×10^{0}	1.1×10^{0}
750	1.2×10^{0}	2.9×10^{0}	1.8×10^{0}
1000	1.7×10^{1}	4.2×10^{0}	2.6×10^{0}
2280	4.3×10^{1}	1.1×10^{1}	6.7×10^{0}

Table A.3: Mean track-length of monoenergetic photons in inflated lung, soft tissue and cortical bone.

	Photons $\overline{L}$ (mm)		
Energy (keV)	**Inflated Lung**	**Soft tissue**	**Cortical Bone**
10	7.6×10^{0}	2.1×10^{0}	2.0×10^{-1}
20	6.5×10^{1}	1.8×10^{1}	1.5×10^{0}
50	6.9×10^{2}	1.8×10^{2}	2.2×10^{1}
100	1.6×10^{3}	4.2×10^{2}	9.5×10^{1}
150	2.1×10^{3}	5.5×10^{2}	1.6×10^{2}
200	2.4×10^{3}	6.2×10^{2}	2.0×10^{2}
250	2.6×10^{3}	6.8×10^{2}	2.3×10^{2}
300	2.8×10^{3}	7.2×10^{2}	2.5×10^{2}
400	3.0×10^{3}	7.8×10^{2}	2.9×10^{2}
500	3.2×10^{3}	8.2×10^{2}	3.2×10^{2}
750	3.5×10^{3}	9.0×10^{2}	3.6×10^{2}
1000	3.8×10^{3}	9.6×10^{2}	4.0×10^{2}
2280	4.4×10^{3}	1.1×10^{3}	4.9×10^{2}

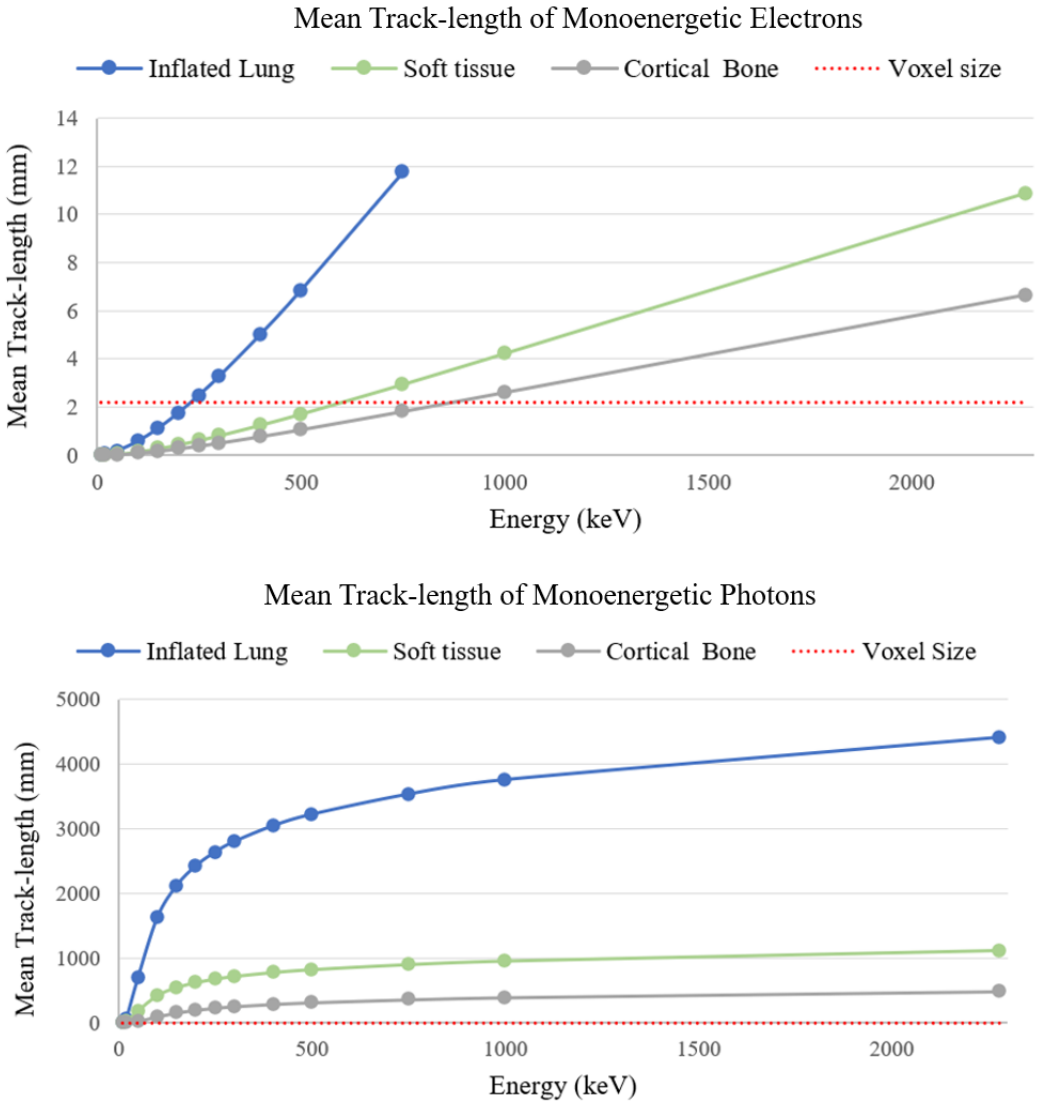

Figure A.1: Mean track-length of mono-energetic electrons and photons in inflated lung, soft tissue and cortical bone.

Overall, the mean track-length increases with the particle's kinetic energy and is significantly shorter for electrons than for photons. Comparing the mean track-length of electrons and photons in each standard material, the following observations were drawn:

- **In inflated lung:**
  - Electrons up to 200 keV have a shorter mean track-length than the voxel size;
  - Photons from 10 keV have longer mean track-length than the voxel size.
- **In soft tissue:**
  - Electrons up to 500 keV have a shorter mean track-length than the voxel size;

  - Photons up to 10 keV have a shorter mean track-length than the voxel size.

- **In cortical bone:**
  - Electrons up to 750 keV have a shorter mean track-length than the voxel size;
  - Photons up to 20 keV have a shorter mean track-length than the voxel size.

A.4 Discussion

The *minimum kinetic energy* cut was set considering the mean track-length of mono-energetic particles for the configured standard materials:

- **For electrons:** *minimum kinetic energy* = 20 keV. Electrons up to 50 keV have a mean track-length shorter than the voxel size of ADDs in all standard materials. However, these electrons can produce secondary photons with much longer mean track-length. Because of that, the *minimum kinetic energy* must be shorter than 50 keV. Electrons up to 20 keV produce mostly X-rays after ionization, and X-rays have energies below 4 keV for organic atoms. Therefore, a *minimum kinetic energy* cut of 20 keV for electrons ensures dosimetry accuracy within the PTV, NLV and heterogeneous organs-at-risk.
- **For photons:** *minimum kinetic energy* = 10 keV. In soft tissue and compact bone, photons up to 10 keV have a smaller mean track-length than the voxel size of ADDs. In inflated lungs, 10 keV photons have a greater mean track-length than the voxel size of ADDs. Nevertheless, only a small amount of electrons emitted by ^{90}Y produce secondary photons, i.e., radiation stopping-power is much smaller than the collision stopping-power as described in chapter 2. Therefore, a *minimum kinetic energy* cut of 10 keV for photons would benefit the speed of MC-GATE simulations, ensuring dosimetry accuracy within the NLV and PTV and without significantly jeopardizing dosimetry accuracy in lung tissues.

Appendix **B**

Uncertainty of MC-GATE dosimetry

B.1 Introduction

MC-GATE dosimetry calculations are stochastic and have an inherent statistical uncertainty in the calculation of ADDs. In Chapter 4, GATE's calculation of the statistical uncertainty SU_{k} in a voxel k was explained. According to Equation 4.17, the statistical uncertainty in a voxel decreases with increasing absorbed dose, D, and total number of simulated primary particles, N_{PP}. Therefore, there is a trade-off between obtaining low statistical uncertainty and what is feasible in RE clinical schedule because simulating more primary particles takes more time.

IAEA recommends that the mean statistical uncertainty, $\overline{SU}$, within the target volume should be less than 2% for MC dosimetry in EBRT treatment plans [107], but guidelines for MC dosimetry in RE are undefined to date. A key difference between EBRT and RE potentially jeopardizes the applicability of this recommendation in RE: while EBRT achieves a uniform ADD within the target volume, RE yields rather non-uniform ADD. In RE scope, this short investigation aims to:

1. Explore a threshold for the mean statistical uncertainty within the PTV below which the obtained ADDs are sufficiently accurate while keeping the simulation time as low as possible;
2. Set the number of primary particles - related to the pre-defined mean statistical uncertainty threshold - for all RE patients' MC-GATE dosimetry simulations.

B.2 Methodology

This investigation follows a methodology proposed by Chetty *et al.* [113]. The group studied the effect of statistical uncertainty in DVH for lung cancer patients treated with EBRT by simulating ADDs with different number of primary particles: 1.0×10^{7}, 1.5×10^{8}, 5.0×10^{8}, and 1.5×10^{9}. For this purpose, the group plotted DVH and uncertainty volume histograms (UVH). Figures B.1 and B.2 present the cumulative and differential DVH

and UVH computed for the gross tumor volume[1] and normal lung tissue, respectively. DVHs converged at $N_{PP} = 1.5 \times 10^7$ for the gross tumor volume, corresponding to a mean statistical uncertainty of less than 2%. DVH also converged at $N_{PP} = 1.5 \times 10^7$ for the normal liver volume, but with much wider UVH.

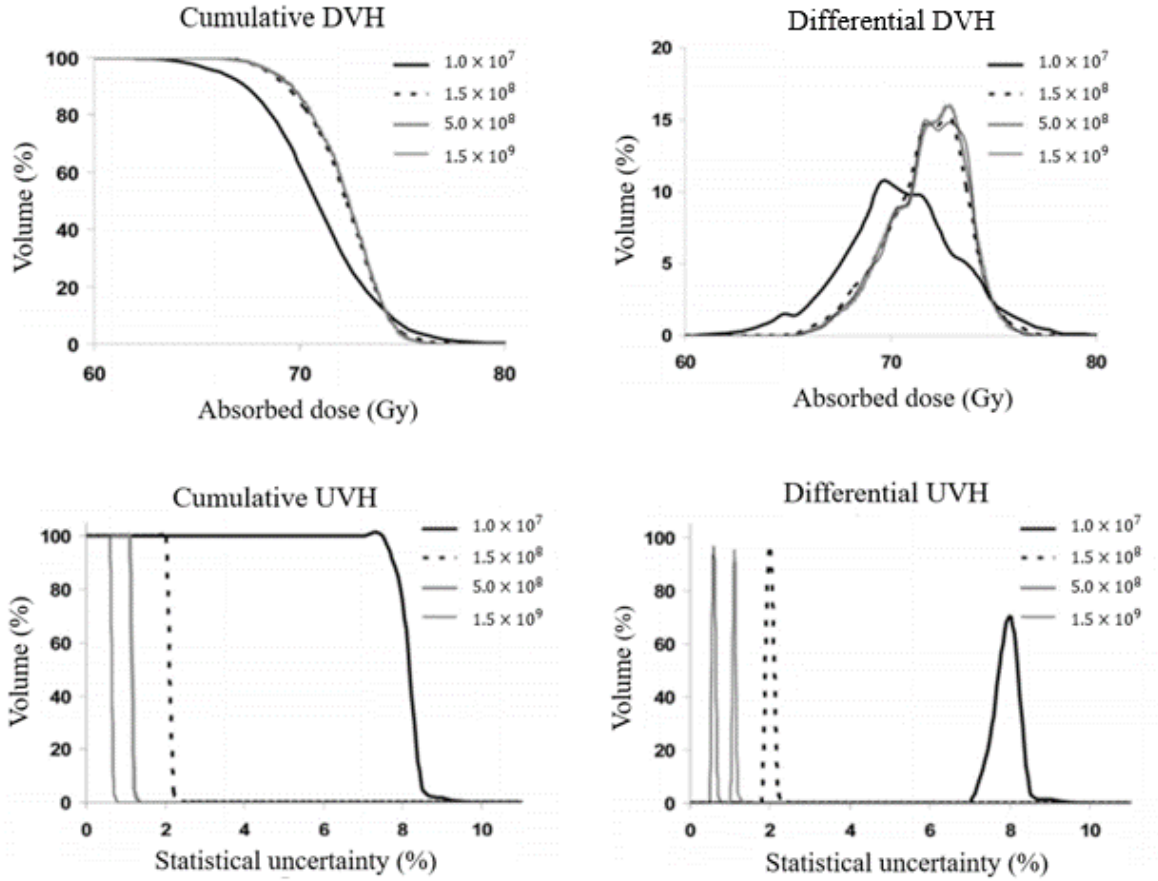

Figure B.1: DVH and UVH computed for the gross tumor volume in a lung cancer patient treated with EBRT. Curves are shown for MC treatment plans simulated with 1.0×10^7, 1.5×10^8, 5.0×10^8, and 1.5×10^9 primary particles. Adapted from: [113]

[1] The gross tumor volume corresponds to what can be seen, palpated or imaged.

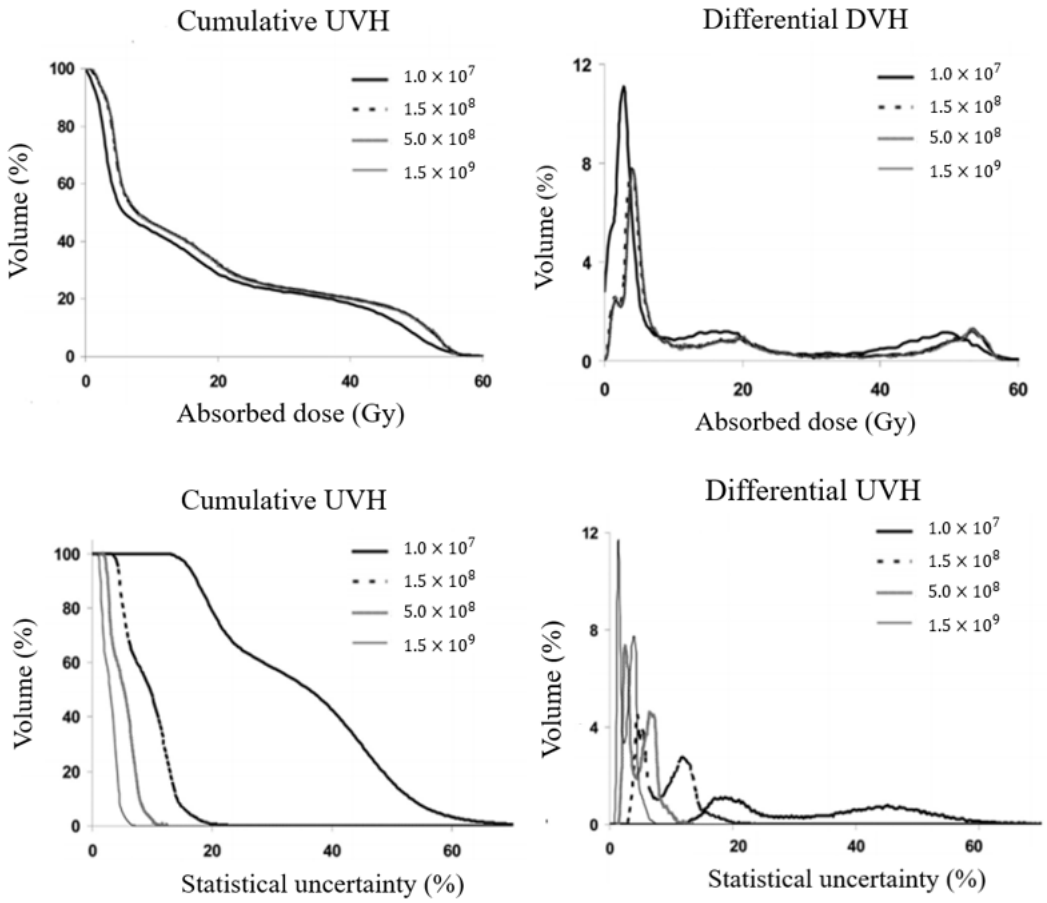

Figure B.2: DVH and UVH within the NLV in a lung cancer patient treated with EBRT. Curves are shown for MC treatment plans simulated with 1.0×10^7, 1.5×10^8, 5.0×10^8, and 1.5×10^9 primary particles. Adapted from: [113]

In this investigation, EBRT histograms in Figures B.1 and B.2 were compared to their RE equivalents. For this purpose, four MC-GATE dosimetry simulations were performed for patient 1 treatment planning[2] with different number of primary particles: 1.0×10^7, 5.0×10^7, 1.5×10^8, and 2.5×10^8. ADDs and statistical uncertainty distributions were retrieved from MC-GATE simulations and ADDs were calibrated. Afterwards, the following measurements were obtained within the PTV and the NLV for each simulation:

1. Mean absorbed dose $\overline{D}$ and mean statistical uncertainty $\overline{SU}$, the latter according to:

$$\overline{SU} = \sqrt{\frac{1}{n}\sum_{k=1}^{n} S_k^2}, \tag{B.1}$$

   where n is the number of voxels in each VOI;
2. DVH with a bin width of 1 Gy and UVH with a bin width of 1%;

[2]This patient was selected randomly from this study's dataset.

3. Dose uncertainty histogram (DUH) with a bin width of 10 Gy from 0 to 50 Gy and a bin width of 50 Gy from 50 to 300 Gy. DUH plot the arithmetic statistical uncertainty within a VOI for voxels with an absorbed dose in a certain range.

B.3 Results

MC-GATE simulations of ADDs with 1.0×10^7, 5.0×10^7, 1.5×10^8, and 2.5×10^8. primary particles took 2, 7, 27, and 45 hours, respectively. Figure B.3 displays a cross-sectional view of the ADD simulated with 2.5×10^8 primary particles on top of the CT image of patient 1 in treatment planning.

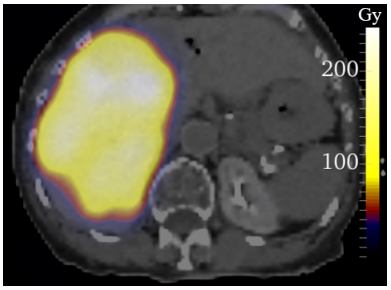

Figure B.3: Cross-sectional view of the ADD, in Gy, simulated with 2.5×10^8 primary particles on top of the CT image of patient 1 in treatment planning.

Figure B.4 displays the statistical uncertainty distributions returned by simulations with different number of primary particles on top of the same cross-sectional view of patient's 1 CT image, displayed in Figure B.3. Within each statistical uncertainty distribution, voxels with higher absorbed dose showed smaller uncertainty. In general, a higher number of simulated primary particles yielded lower uncertainty. For N_{PP} = 1.0E7, uncertainty was maximum for many voxels with low absorbed dose, indicating that few or no collision with energy lose occurred in those voxels during the simulation. Even for $N_{PP} = 2.5 \times 10^8$ primary particles there were voxels with $SU > 0.50$.

B.3.1 Uncertainty within the PTV

Table B.1 lists mean absorbed dose and mean statistical uncertainty within the PTV calculated for the ADDs simulated with different number of primary particles. Mean absorbed dose values only deviate up to 0.04 Gy from the values obtained with $N_{PP} = 2.5 \times 10^8$, indicating convergence of ADDs from the smallest number of simulated primary particles. Nevertheless, the mean statistical uncertainty within the PTV for $N_{PP} = 1.5 \times 10^8$ primary particles is over 3% and not below 2% as in the Chatty *et al.* study.

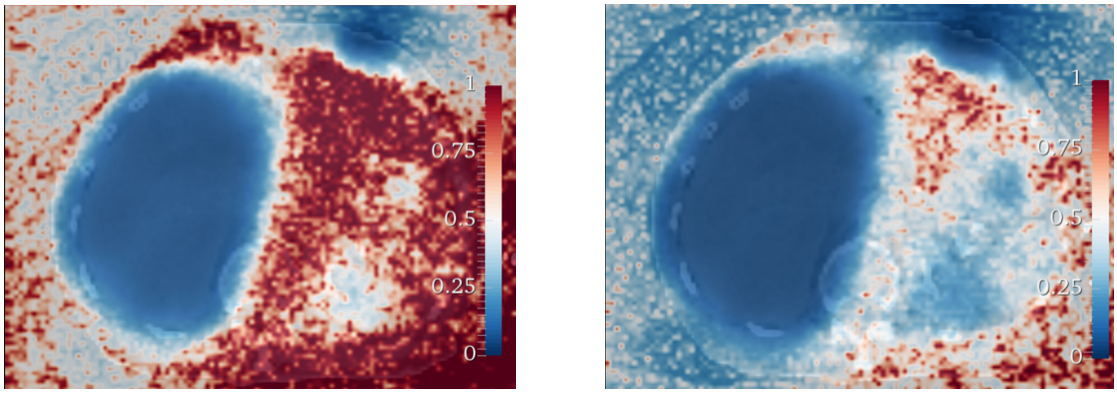

(a) $N_{PP} = 1.0 \times 10^7$ (b) $N_{PP} = 5.0 \times 10^7$

(c) $N_{PP} = 1.5 \times 10^8$ (d) $N_{PP} = 2.5 \times 10^8$

Figure B.4: Cross-sectional view of statistical uncertainty distribution returned by simulations with different number of primary particles on top of the CT image view in Figure B.3.

Table B.1: Mean absorbed dose and mean statistical uncertainty within the PTV obtained for distributions simulated with different number of primary particles.

$\mathbf{N_{PP}}$	**PTV**	
	$\overline{\mathbf{D}}$ **(Gy)**	$\overline{\mathbf{SU}}$ (%)
1.0×10^7	93.43	13%
5.0×10^7	93.44	5.8%
1.5×10^8	93.38	3.3%
2.5×10^8	93.40	2.6%

Figures B.5 shows DVH and UVH, in cumulative and differential formats, computed within the PTV for distributions simulated with different number of primary particles. Convergence of the DVH happens for all number of primary particles because they are indiscernible. In the study conducted by Chatty *et al.* convergence only appeared for distributions simulated with over 1.5×10^8 primary particles.

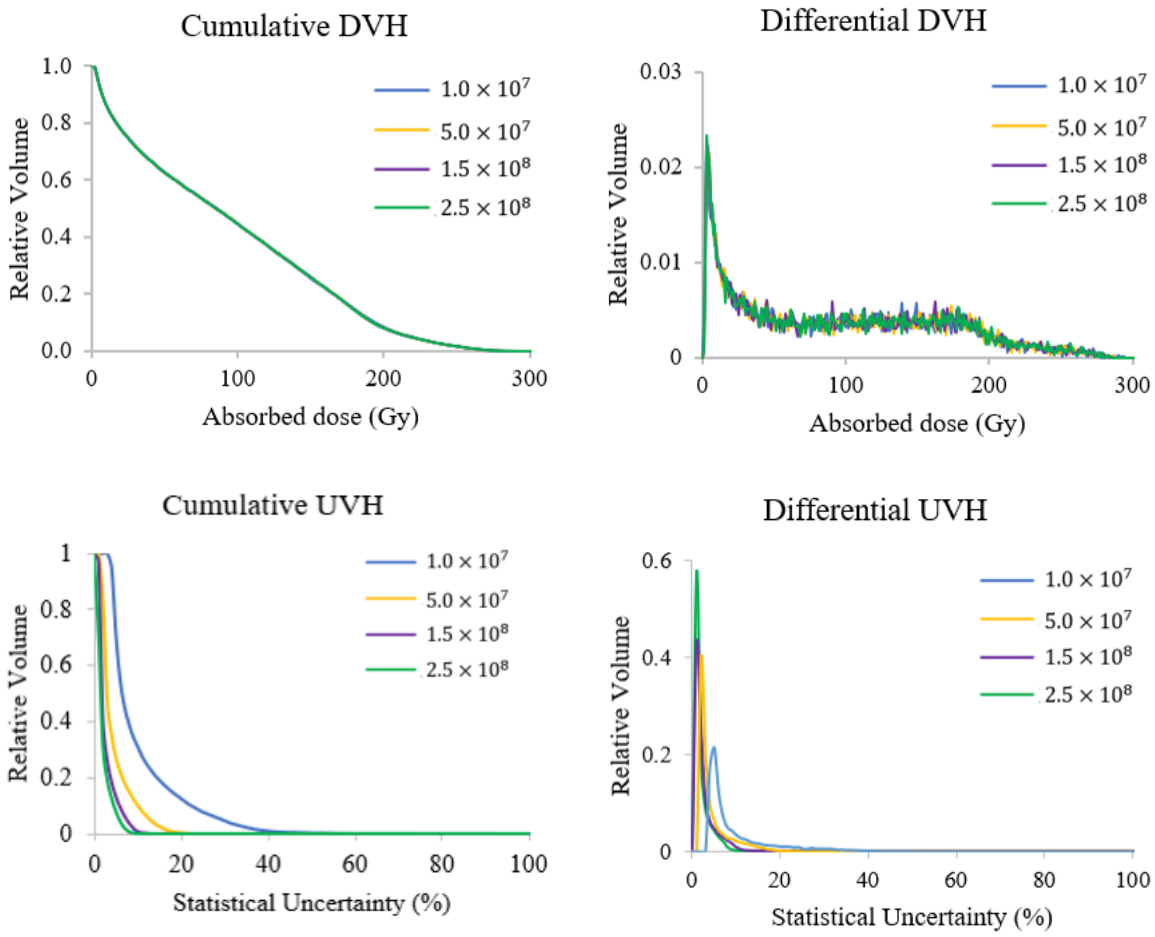

Figure B.5: DVH and UVH within the PTV for RE patient 1. Curves are shown for MC-GATE dosimetry simulations with 1.0×10^7, 5.0×10^7, 1.5×10^8, and 2.5×10^8 primary particles.

Comparing cumulative and differential DVH and UVH obtained for EBRT and RE at the target volume (Figures B.1 and B.5), key differences were observed:

a) **In cumulative DVH:** the plateau present in EBRT cumulative DVH does not exist in RE, indicating that ADD is highly non-uniform in RE;

b) **In differential DVH:** the peak in EBRT differential DVH is located close to the mean absorbed dose, whereas in RE there is a peak at low absorbed doses and a noisy plateau for high absorbed doses, indicating again a non-uniform ADD in RE;

c) **In cumulative UVH:** the plateau present in EBRT cumulative UVH does not exist in RE, indicating that statistical uncertainty distribution is not uniform in RE, as well;

d) **In differential UVH:** the statistical uncertainty distribution in EBRT is roughly gaussian whereas in RE it has an extensive right tail.

These key differences suggest that, to obtain the same mean statistical uncertainty within the target volume, the peak of differential UVH must occur at significantly lower uncertainty values in RE than in EBRT. A very high number of simulated primary particles is requited to shift the UVH peak to lower uncertainty values, but has little effect on the accuracy DVH as DVHs converge for a lower number of primary particles. Therefore, meeting the mean statistical uncertainty threshold within the PTV recommended for MC dosimetry in EBRT might not be necessary in RE.

B.3.2 Uncertainty within the NLV

Table B.2 lists mean absorbed dose and mean statistical uncertainty within the NLV calculated for ADDs simulated with different number of primary particles. All distributions return the same mean absorbed dose, indicating convergence from the smallest number of primary particles. As expected, values of the mean statistical uncertainty are larger for the NLV than for the PTV because the absorbed dose is smaller.

Table B.2: Mean absorbed dose and mean statistical uncertainty within the NLV obtained for distributions simulated with different number of simulated primary particles.

N_{PP}	NLV	
	$\overline{D}$(Gy)	$\overline{SU}$ (%)
1.0×10^7	63.91	47%
5.0×10^7	63.91	30%
1.5×10^8	63.91	19%
2.5×10^8	63.91	15%

Figure B.6 shows DVH and UVH, in cumulative and differential formats, computed within the NLV for distributions simulated with different number of primary particles. Convergence of the DVH happens again for all distributions because they are indiscernible. Comparing DVH and UVH obtained for EBRT and RE at normal tissues (Figures B.2 and B.6), there is a bigger similarity between equivalent histograms than at the target volume because the ADD is non-uniform for both EBRT and RE.

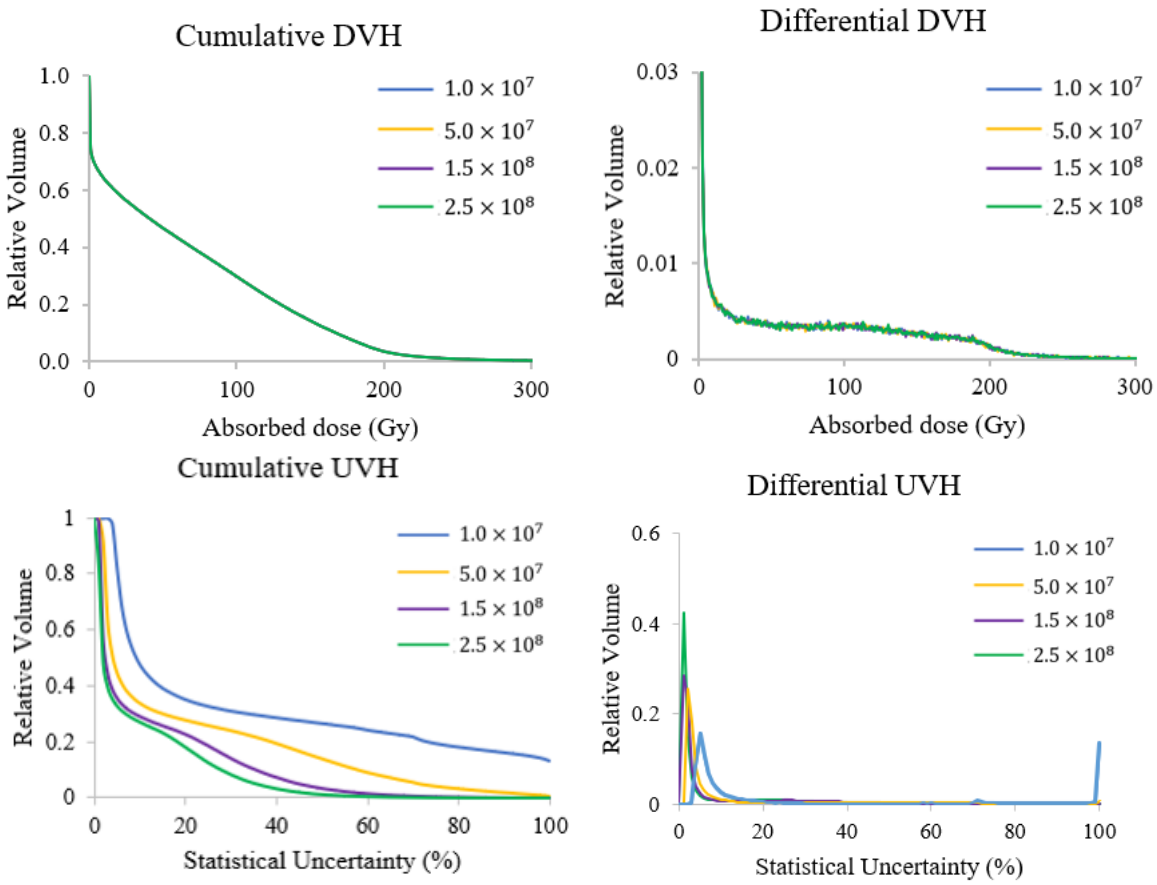

Figure B.6: DVH and UVH within NLV for RE patient 1. Curves are shown for MC-GATE dosimetry simulations with 1.0×10^7, 5.0×10^7, 1.5×10^8, and 2.5×10^8 primary particles.

B.3.3 Dose - Uncertainty Relationship

Figures B.7 and B.8 plot piled DUH for the distributions simulated with different number of primary particles within the PTV and the NLV, respectively. From these plots, several observations are made:

1. For a given number of primary particles, the statistical uncertainty is significantly higher for lower absorbed dose voxels;
2. For a given absorbed dose bin, the statistical uncertainty is smaller for a higher number of simulated primary particles;
3. For absorbed dose bins above 50 Gy:
   a) The mean statistical uncertainty within the PTV and NLV match for the same number of simulated primary particles,
   b) The mean statistical uncertainty in distributions simulated with 1.5×10^8 primary particles or more is smaller than the recommended 2%.

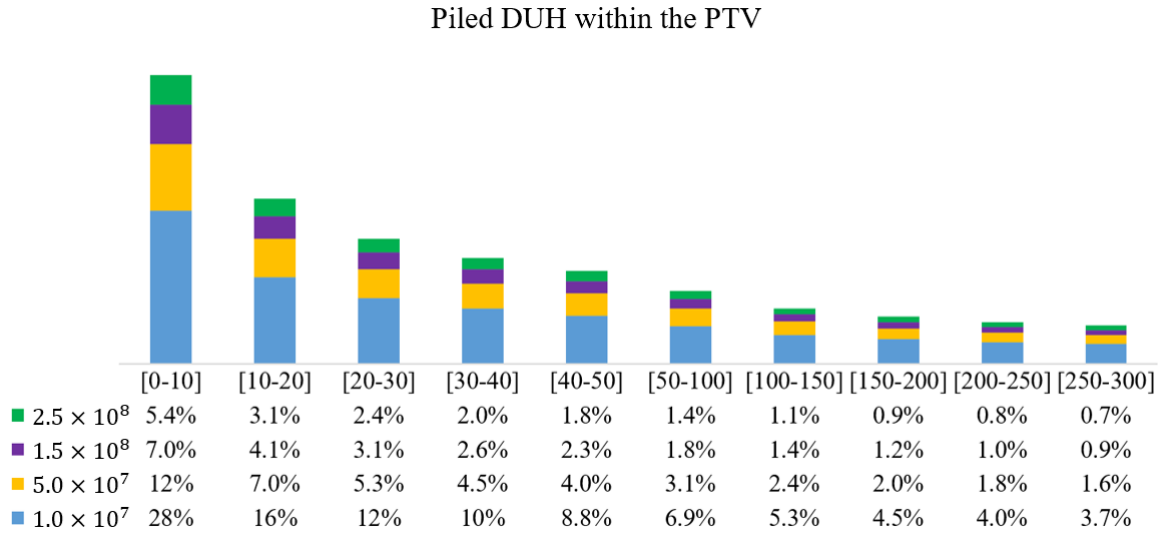

Figure B.7: Piled DUH within the PTV for distributions simulated with 1.0×10^7, 5.0×10^7, 1.5×10^8, and 2.5×10^8 primary particles.

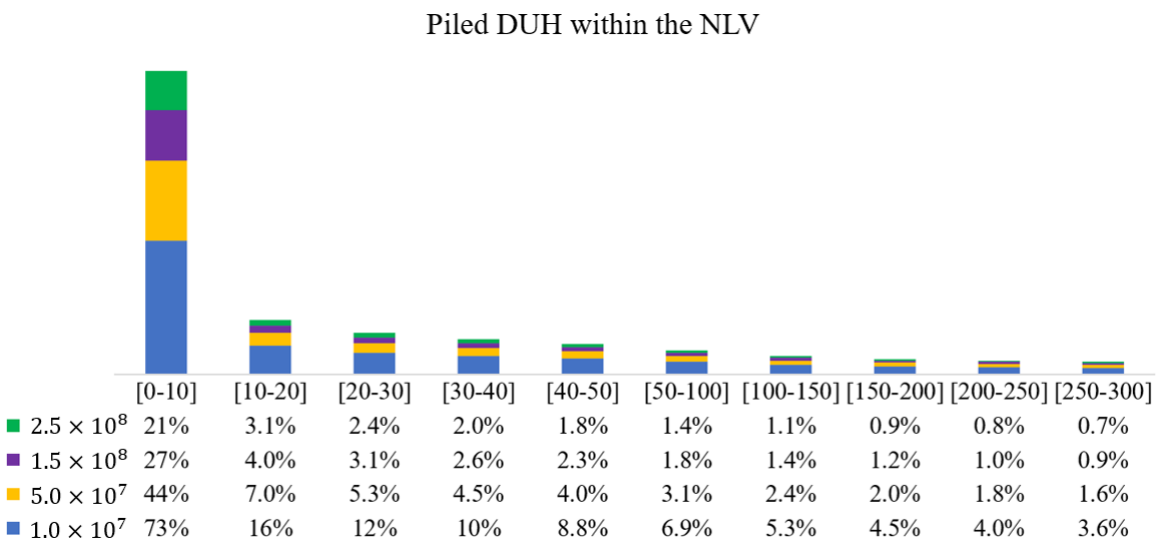

Figure B.8: Piled DUH within the NLV for distributions simulated with 1.0×10^7, 5.0×10^7, 1.5×10^8, and 2.5×10^8 primary particles.

B.4 Discussion

The mean absorbed dose within the PTV and the NLV converged rapidly in MC dosimetry for RE patient 1, i.e., with only 10E6 simulated primary particles. However, IAEA reccommends that mean statistical uncertainty within the PTV should be < 2%. This threshold was not fulfilled even by simulating 2.5×10^8 primary particles because ADDs in RE are highly non-uniform. Considering only the voxels with absorbed doses

higher than 50 Gy, this requirement is fulfilled when simulating 1.5×10^8 primary particles for RE patient 1. However, this study might not be sufficient to draw this conclusion for other RE patients because there is a great inter-patient variability of ADDs. For different RE patients, the number of voxels in each absorbed dose bin in DUHs is expected to vary, but the mean statistical uncertainty in each absorbed dose bin should similar to that of patient 1.

RE guidelines recommend a mean absorbed dose within the PTV above 80 Gy. Thus, without further investigations and to comply with IAEI recommendation, the following conclusions were drawn:

1. **Threshold for mean statistical uncertainty:** GATE dosimetry simulations with a $\overline{SU} < 2\%$ in voxels with $D_k > 80$ Gy, $\overline{SU}_{D_k>80}$, are sufficiently accurate;
2. **Set-up of the number of primary particles:**
   a) Initially, ADDs should be simulated with a reasonably small number of primary particles (e.g. $N_{\mathrm{PP}} = 2.5 \times 10^6$);
   b) If $\overline{SU}_{D_k>80Gy}$ is smaller than 2%, a second simulation should be started with a different seed.
   c) Then, the first and second simulation's output ADDs should be added, and the final statistical uncertainty distribution computed through Equation 4.17.
   d) Finally, the mean statistical uncertainty threshold should be checked again, repeating steps *b)* and *c)*, if needed.

It is relevant to mention that uncertainty of ADDs computed for EBRT patients depends not only in the uncertainty of MC simulations, but also in errors related to the reproducibility of patient positioning inter- and intra-fractions, and external beam deviations. At the end of this error chain, uncertainty of EBRT dosimetry is usually around 5%. These variables do not play a role in RE dosimetry uncertainty because the radiation source is delivered internally and in one fraction. Therefore, it might be acceptable to allow a higher threshold for $\overline{SU}_{D_k>80Gy}$ within the PTV for RE dosimetry.

Appendix C

Interface Study

C.1 Introduction

The key difference between VSV and MC dosimetry methods is that only the latter considers tissue heterogeneity. Therefore, MC dosimetry is most useful in RE scope to investigate ADDs at the liver interface with surrounding tissues, i.e., where tissue heterogeneity is most significant. In particular, the liver-lung interface behavior of the absorbed dose might be relevant to understand possible side-effects in lungs - a low density organ-at-risk.

This short study seeks to investigate the interface behavior of the absorbed dose for a uniform ^{90}Y activity distribution based on MC-GATE dosimetry in comparison to VSV dosimetry. At the end of this study, a prediction of the interface behavior was made for non-uniform ^{90}Y – MS activity distribution in RE patients.

C.2 Methodology

Two MC-GATE configurations were employed to investigate the interface behavior of the absorbed dose. Set-up of each configuration for the *voxelized geometry* and *source* is described below:

1. **Voxelized geometry:** a single voxelized geometry was built using MATLAB for both configurations through a digital CT image, as illustrated in Figure C.1a. Three uniform cubes of different materials were defined, including *lung* RT (-620 HU), *muscle/general* RT (42 HU), and *mineral bone* RT (1603 HU). The edge of each cube was 30 voxels long, with a resolution of 2.21 mm. Surrounding the cubes, a parallelepiped made of *muscle/general* RT was defined to allow for backscattering.

2. **Voxelized source:** two voxelized sources were build using MATLAB through digital SPECT images, as illustrated in Figures C.1b and C.1c. First, a global uniform ^{90}Y activity distribution was defined in the whole geometry. Second, a uniform ^{90}Y

activity distribution was defined only in the center cube, made of *muscle/general* RT, with a null activity in the remaining geometry.

(a) Digital CT image representing the voxelized geometry

(b) Digital SPECT image representing the voxelized source with global uniform activity

(c) Digital SPECT image representing the voxelized source with center uniform activity

Figure C.1: Cross-sectional view of digital CT and SPECT images built to represent voxelized geometry and sources in MC-GATE dosimetry simulations for the interface study.

MC-GATE dosimetry simulations were stopped after generating 100E6 primary particles and returned uncalibrated ADDs and uncalibrated energy distributions EDs. The uncalibrated ADDs were calibrated to a total activity of 1 GBq. VSV dosimetry was performed for comparison based on the digital SPECT images. All computations were performed using MATLAB.

To investigate the interface behavior of the absorbed dose, 1D profiles were selected from the ADDs and EDs obtained with MC-GATE dosimetry and from the ADDs obtained with VSV dosimetry. The profiles were selected at the center of the geometry, crossing the relevant interfaces, using 3D Slicer.

C.3 Results and Discussion

Figure C.2 plots the 1D profiles computed for the global uniform ^{90}Y activity configuration. Comparing the deposited energy and absorbed dose estimated by MC-GATE dosimetry, energy is similar for all center voxels in the three RT cubes, while dose is higher for *lung* RT and lower for *mineral bone*. This result is explained by variation in voxels' mass density, according to equation 2.7. At interface voxels, the oscillation observed

in energy profiles[1] turns into a build-up of dose due to, again, variations in mass density. Comparing the absorbed dose estimated by VSV and MC-GATE dosimetry methods, VSV is accurate in the *muscle/general* RT cube, while it underestimated dose in the *muscle/general* RT cube and overestimated in *mineral bone* RT cube. This results are explained by the negligence of tissue heterogeneity by VSV dosimetry.

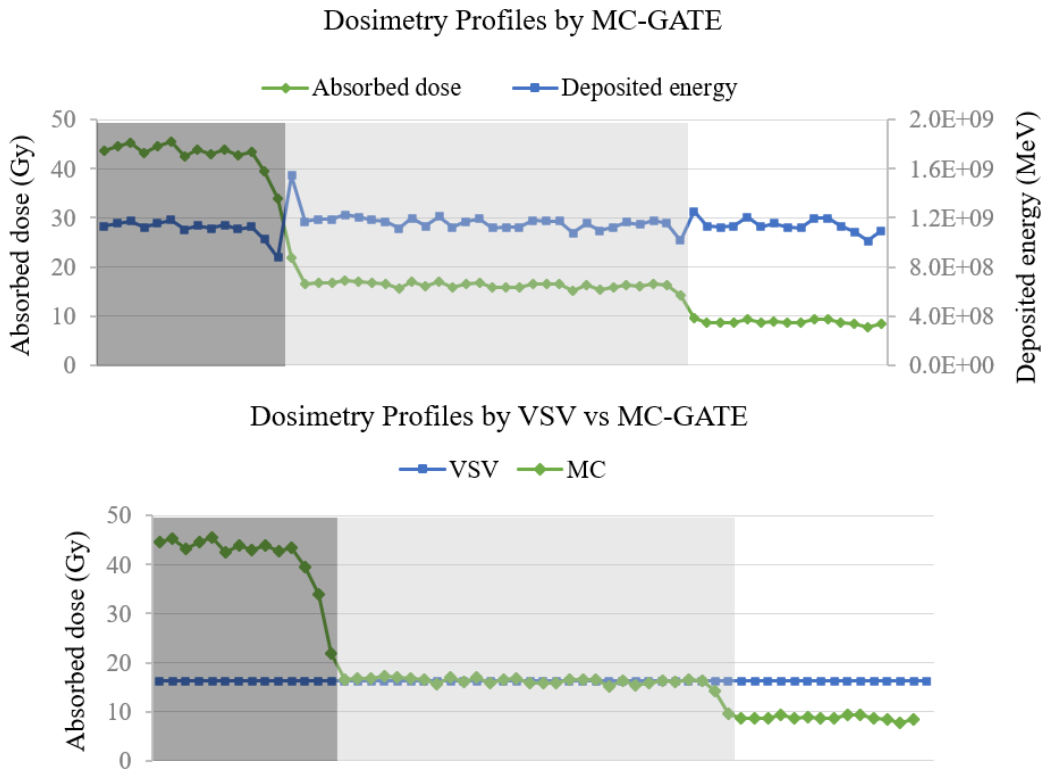

Figure C.2: Dosimetry profiles for the global uniform ^{90}Y activity. The dark grey, light grey and weight regions are associated to *lung* RT, *muscle/general* RT, and *mineral bone* RT

Figure C.2 plots the 1D profiles for the center uniform ^{90}Y activity configuration. Comparing the deposited energy and absorbed dose profiles estimated by MC-GATE dosimetry, both quantities decreased continuously from interface voxels in in *muscle/general* RT cube to voxels in the adjacent cubes. This build down happens because the range of ^{90}Y radiation in *muscle/general* RT is short and ^{90}Y activity outside the *muscle/general* RT cube was null. Nevertheless, a slower build down was observed in the *lung* RT cube comparing to that in the *mineral bone* RT cube because the range of ^{90}Y radiation is longer in lower density mediums. Comparing the absorbed dose profiles estimated by VSV and MC-GATE dosimetry methods, VSV is accurate in the *muscle/general* RT cube, but it underestimated dose in *lung* RT voxels at the interface of *lung* RT with *muscle/general* RT.

[1] The deposited energy is lower in voxels with the lower CT number comparing to center voxels, and it is higher in voxels with higher CT number comparing to center voxels.

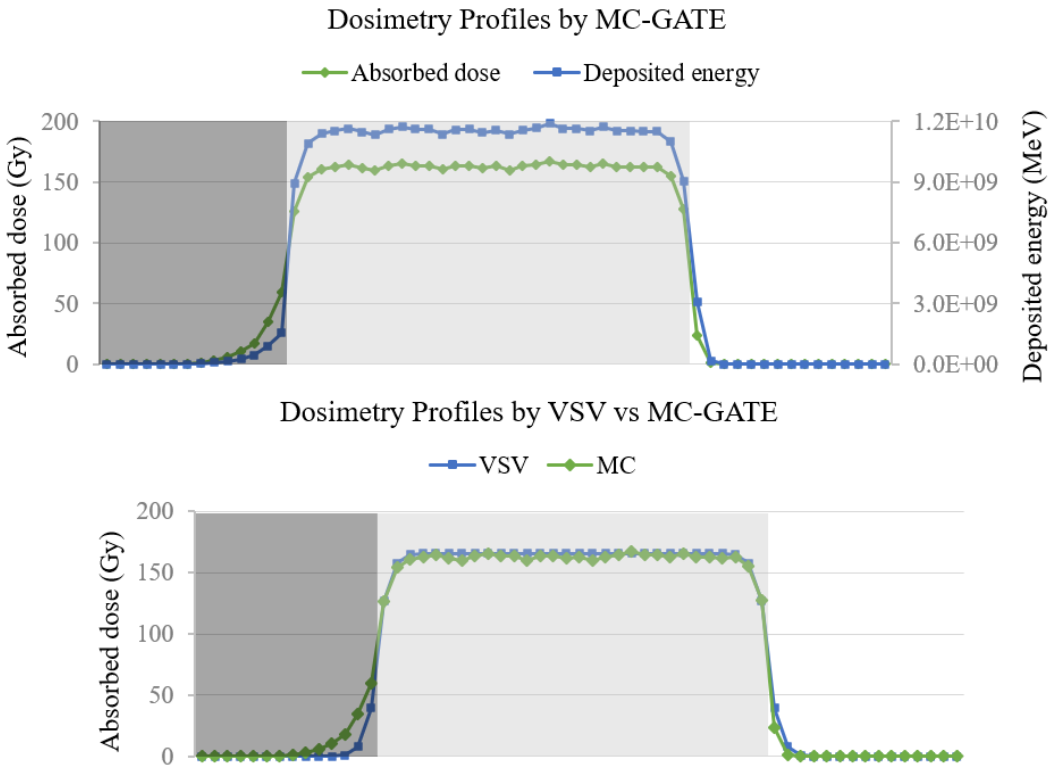

Figure C.3: Dosimetry profiles for the center uniform ^{90}Y activity. The dark grey, light grey and weight regions are associated to *lung* RT, *muscle/general* RT, and *mineral bone* RT

The configuration with a center uniform activity distribution resembles better the non-uniform activity distribution in RE patients as most ^{90}Y – MS are within the WLV - a soft tissue. Overall, the results of this configuration predict that MC-GATE dosimetry is relevant to investigate possible side-effects of RE in lungs, as VSV dosimetry likely underestimates the absorbed dose at the liver-lung interface.

Appendix D

VSV Kernel

VSV Octant				S-Values (mGy/MBq/s)		
i	j	k	d (mm)	Simulated	Reference	*RD* (%)
0	0	0	0.00	3.02×10^{0}	3.00×10^{0}	0.8
0	0	1	2.21	5.66×10^{-1}	5.70×10^{-1}	-0.7
0	1	0	2.21	5.66×10^{-1}	5.70×10^{-1}	-0.7
1	0	0	2.21	5.66×10^{-1}	5.70×10^{-1}	-0.7
0	1	1	3.13	2.24×10^{-1}	2.26×10^{-1}	-0.8
1	0	1	3.13	2.24×10^{-1}	2.26×10^{-1}	-0.8
1	1	0	3.13	2.24×10^{-1}	2.26×10^{-1}	-0.9
1	1	1	3.83	1.19×10^{-1}	1.20×10^{-1}	-1.0
0	0	2	4.42	6.96×10^{-2}	7.00×10^{-2}	-0.6
0	2	0	4.42	6.97×10^{-2}	7.00×10^{-2}	-0.4
2	0	0	4.42	6.96×10^{-2}	7.00×10^{-2}	-0.6
0	1	2	4.94	4.56×10^{-2}	4.58×10^{-2}	-0.5
0	2	1	4.94	4.56×10^{-2}	4.58×10^{-2}	-0.4
1	0	2	4.94	4.56×10^{-2}	4.58×10^{-2}	-0.5
1	2	0	4.94	4.57×10^{-2}	4.58×10^{-2}	-0.2
2	0	1	4.94	4.56×10^{-2}	4.58×10^{-2}	-0.4
2	1	0	4.94	4.57×10^{-2}	4.58×10^{-2}	-0.2
1	1	2	5.41	3.07×10^{-2}	3.08×10^{-2}	-0.3
1	2	1	5.41	3.07×10^{-2}	3.08×10^{-2}	-0.3
2	1	1	5.41	3.07×10^{-2}	3.08×10^{-2}	-0.3
0	2	2	6.25	1.46×10^{-2}	1.46×10^{-2}	-0.1
2	0	2	6.25	1.46×10^{-2}	1.46×10^{-2}	-0.1
2	2	0	6.25	1.46×10^{-2}	1.46×10^{-2}	-0.1
0	0	3	6.63	1.00×10^{-2}	1.01×10^{-2}	-0.6
0	3	0	6.63	1.01×10^{-2}	1.01×10^{-2}	-0.2
3	0	0	6.63	1.01×10^{-2}	1.01×10^{-2}	-0.4
1	2	2	6.63	1.02×10^{-2}	1.02×10^{-2}	-0.1
2	1	2	6.63	1.01×10^{-2}	1.02×10^{-2}	-1.1
2	2	1	6.63	1.01×10^{-2}	1.02×10^{-2}	-0.5
0	1	3	6.99	6.98×10^{-3}	7.10×10^{-3}	-1.7
0	3	1	6.99	7.04×10^{-3}	7.10×10^{-3}	-0.9
1	0	3	6.99	7.08×10^{-3}	7.10×10^{-3}	-0.3
1	3	0	6.99	7.03×10^{-3}	7.10×10^{-3}	-1.1
3	0	1	6.99	7.02×10^{-3}	7.10×10^{-3}	-1.1
3	1	0	6.99	7.06×10^{-3}	7.10×10^{-3}	-0.5
1	1	3	7.33	4.90×10^{-3}	4.98×10^{-3}	-1.6
1	3	1	7.33	4.90×10^{-3}	4.98×10^{-3}	-1.5
3	1	1	7.33	4.93×10^{-3}	4.98×10^{-3}	-1.1
2	2	2	7.66	3.44×10^{-3}	3.50×10^{-3}	-1.9

0	2	3	7.97	2.38×10^{-3}	2.41×10^{-3}	-1.4
0	3	2	7.97	2.36×10^{-3}	2.41×10^{-3}	-1.9
2	0	3	7.97	2.37×10^{-3}	2.41×10^{-3}	-1.7
2	3	0	7.97	2.36×10^{-3}	2.41×10^{-3}	-2.0
3	0	2	7.97	2.37×10^{-3}	2.41×10^{-3}	-1.7
3	2	0	7.97	2.36×10^{-3}	2.41×10^{-3}	-1.9
1	2	3	8.27	1.63×10^{-3}	1.66×10^{-3}	-2.0
1	3	2	8.27	1.63×10^{-3}	1.66×10^{-3}	-1.8
2	1	3	8.27	1.62×10^{-3}	1.66×10^{-3}	-2.4
2	3	1	8.27	1.64×10^{-3}	1.66×10^{-3}	-1.3
3	1	2	8.27	1.61×10^{-3}	1.66×10^{-3}	-2.7
3	2	1	8.27	1.62×10^{-3}	1.66×10^{-3}	-2.6
0	0	4	8.84	7.22×10^{-4}	7.52×10^{-4}	-4.0
0	4	0	8.84	7.21×10^{-4}	7.52×10^{-4}	-4.1
4	0	0	8.84	7.23×10^{-4}	7.52×10^{-4}	-3.9
2	2	3	9.11	5.05×10^{-4}	5.19×10^{-4}	-2.8
2	3	2	9.11	5.02×10^{-4}	5.19×10^{-4}	-3.4
3	2	2	9.11	5.01×10^{-4}	5.19×10^{-4}	-3.4
0	1	4	9.11	4.91×10^{-4}	5.05×10^{-4}	-2.8
0	4	1	9.11	4.92×10^{-4}	5.05×10^{-4}	-2.7
1	0	4	9.11	4.93×10^{-4}	5.05×10^{-4}	-2.4
1	4	0	9.11	4.91×10^{-4}	5.05×10^{-4}	-2.8
4	0	1	9.11	4.97×10^{-4}	5.05×10^{-4}	-1.5
4	1	0	9.11	4.92×10^{-4}	5.05×10^{-4}	-2.5
0	3	3	9.38	3.35×10^{-4}	3.42×10^{-4}	-2.2
1	1	4	9.38	3.21×10^{-4}	3.35×10^{-4}	-4.2
1	4	1	9.38	3.29×10^{-4}	3.35×10^{-4}	-1.8
3	0	3	9.38	3.35×10^{-4}	3.42×10^{-4}	-2.1
3	3	0	9.38	3.34×10^{-4}	3.42×10^{-4}	-2.5
4	1	1	9.38	3.30×10^{-4}	3.35×10^{-4}	-1.4
1	3	3	9.63	2.22×10^{-4}	2.25×10^{-4}	-1.3
3	1	3	9.63	2.16×10^{-4}	2.25×10^{-4}	-4.0
3	3	1	9.63	2.17×10^{-4}	2.25×10^{-4}	-3.6
0	2	4	9.88	1.37×10^{-4}	1.42×10^{-4}	-3.5
0	4	2	9.88	1.38×10^{-4}	1.42×10^{-4}	-2.8
2	0	4	9.88	1.35×10^{-4}	1.42×10^{-4}	-4.7
2	4	0	9.88	1.38×10^{-4}	1.42×10^{-4}	-2.7
4	0	2	9.88	1.35×10^{-4}	1.42×10^{-4}	-4.6
4	2	0	9.88	1.42×10^{-4}	1.42×10^{-4}	-0.2
1	2	4	10.13	9.01×10^{-5}	9.13×10^{-5}	-1.3
1	4	2	10.13	8.90×10^{-5}	9.13×10^{-5}	-2.5
2	1	4	10.13	9.33×10^{-5}	9.13×10^{-5}	2.2
2	4	1	10.13	8.92×10^{-5}	9.13×10^{-5}	-2.3
4	1	2	10.13	9.13×10^{-5}	9.13×10^{-5}	0.0
4	2	1	10.13	8.90×10^{-5}	9.13×10^{-5}	-2.5
2	3	3	10.37	5.89×10^{-5}	5.99×10^{-5}	-1.6
3	2	3	10.37	6.20×10^{-5}	5.99×10^{-5}	3.5
3	3	2	10.37	5.65×10^{-5}	5.99×10^{-5}	-5.7
2	2	4	10.83	2.24×10^{-5}	2.30×10^{-5}	-2.7
2	4	2	10.83	2.35×10^{-5}	2.30×10^{-5}	2.0
4	2	2	10.83	2.11×10^{-5}	2.30×10^{-5}	-8.1

0	3	4	11.05	1.63×10^{-5}	1.42×10^{-5}	15
0	4	3	11.05	1.51×10^{-5}	1.42×10^{-5}	6.2
3	0	4	11.05	1.37×10^{-5}	1.42×10^{-5}	-3.2
3	4	0	11.05	1.50×10^{-5}	1.42×10^{-5}	5.9
4	0	3	11.05	1.45×10^{-5}	1.42×10^{-5}	2.5
4	3	0	11.05	1.48×10^{-5}	1.42×10^{-5}	4.6
0	0	5	11.05	1.31×10^{-5}	1.25×10^{-5}	5.1
0	5	0	11.05	1.26×10^{-5}	1.25×10^{-5}	0.8
5	0	0	11.05	1.31×10^{-5}	1.25×10^{-5}	5.1
1	3	4	11.27	9.46×10^{-6}	9.18×10^{-6}	3.1
1	4	3	11.27	9.26×10^{-6}	9.18×10^{-6}	0.9
4	1	3	11.27	9.31×10^{-6}	9.18×10^{-6}	1.4
4	3	1	11.27	9.39×10^{-6}	9.18×10^{-6}	2.3
0	1	5	11.27	8.39×10^{-6}	8.00×10^{-6}	4.9
0	5	1	11.27	8.28×10^{-6}	8.00×10^{-6}	3.6
1	0	5	11.27	8.06×10^{-6}	8.00×10^{-6}	0.7
1	5	0	11.27	8.83×10^{-6}	8.00×10^{-6}	10
3	1	4	11.27	9.39×10^{-6}	9.18×10^{-6}	2.3
3	4	1	11.27	9.91×10^{-6}	9.18×10^{-6}	7.9
5	0	1	11.27	8.34×10^{-6}	8.00×10^{-6}	4.2
5	1	0	11.27	8.75×10^{-6}	6.42×10^{-6}	6.1
1	1	5	11.48	5.33×10^{-6}	5.36×10^{-6}	-0.6
1	5	1	11.48	5.52×10^{-6}	5.36×10^{-6}	3.1
5	1	1	11.48	5.48×10^{-6}	5.36×10^{-6}	2.2
2	3	4	11.90	3.52×10^{-6}	3.20×10^{-6}	9.9
2	4	3	11.90	3.06×10^{-6}	3.20×10^{-6}	-4.3
0	2	5	11.90	3.03×10^{-6}	2.91×10^{-6}	4.0
0	5	2	11.90	3.16×10^{-6}	2.91×10^{-6}	8.5
2	0	5	11.90	2.51×10^{-6}	2.91×10^{-6}	-14
2	5	0	11.90	2.93×10^{-6}	2.91×10^{-6}	0.7
3	2	4	11.90	3.51×10^{-6}	3.20×10^{-6}	9.7
3	4	2	11.90	3.58×10^{-6}	3.20×10^{-6}	12
4	2	3	11.90	3.51×10^{-6}	3.20×10^{-6}	9.6
4	3	2	11.90	3.40×10^{-6}	3.20×10^{-6}	6.2
5	0	2	11.90	3.55×10^{-6}	2.91×10^{-6}	22
5	2	0	11.90	3.17×10^{-6}	2.91×10^{-6}	9.0
1	2	5	12.10	2.61×10^{-6}	2.39×10^{-6}	9.2
1	5	2	12.10	2.34×10^{-6}	2.39×10^{-6}	-2.0
2	1	5	12.10	2.73×10^{-6}	2.39×10^{-6}	14
2	5	1	12.10	2.66×10^{-6}	2.39×10^{-6}	11
5	1	2	12.10	2.73×10^{-6}	2.39×10^{-6}	14
5	2	1	12.10	2.46×10^{-6}	2.39×10^{-6}	2.7
0	4	4	12.50	2.17×10^{-6}	1.91×10^{-6}	14
4	0	4	12.50	1.93×10^{-6}	1.91×10^{-6}	0.9
4	4	0	12.50	2.08×10^{-6}	1.91×10^{-6}	8.7
1	4	4	12.70	1.77×10^{-6}	1.77×10^{-6}	0.1
4	1	4	12.70	1.87×10^{-6}	1.77×10^{-6}	5.5
4	4	1	12.70	1.81×10^{-6}	1.77×10^{-6}	2.5
2	2	5	12.70	1.94×10^{-6}	1.75×10^{-6}	11
2	5	2	12.70	1.93×10^{-6}	1.75×10^{-6}	10
5	2	2	12.70	1.98×10^{-6}	1.75×10^{-6}	13
0	3	5	12.89	1.64×10^{-6}	1.66×10^{-6}	-1.4

0	5	3	12.89	1.62×10^{-6}	1.66×10^{-6}	-2.4
3	0	5	12.89	1.73×10^{-6}	1.66×10^{-6}	4.4
3	3	4	12.89	1.65×10^{-6}	1.67×10^{-6}	-1.1
3	4	3	12.89	1.81×10^{-6}	1.67×10^{-6}	8.4
3	5	0	12.89	1.55×10^{-6}	1.66×10^{-6}	-6.8
4	3	3	12.89	1.78×10^{-6}	1.67×10^{-6}	6.5
5	0	3	12.89	1.52×10^{-6}	1.66×10^{-6}	-8.2
5	3	0	12.89	1.65×10^{-6}	1.66×10^{-6}	-0.3
1	3	5	13.07	1.61×10^{-6}	1.59×10^{-6}	1.1
1	5	3	13.07	1.44×10^{-6}	1.59×10^{-6}	-9.3
3	1	5	13.07	1.60×10^{-6}	1.59×10^{-6}	0.9
3	5	1	13.07	1.76×10^{-6}	1.59×10^{-6}	11
5	1	3	13.07	1.46×10^{-6}	1.59×10^{-6}	-7.9
5	3	1	13.07	1.51×10^{-6}	1.59×10^{-6}	-5.2
2	4	4	13.26	1.53×10^{-6}	1.53×10^{-6}	0.3
4	2	4	13.26	1.66×10^{-6}	1.53×10^{-6}	8.2
4	4	2	13.26	1.48×10^{-6}	1.53×10^{-6}	-3.5
2	3	5	13.62	1.57×10^{-6}	1.43×10^{-6}	9.7
2	5	3	13.62	1.47×10^{-6}	1.43×10^{-6}	3.1
3	2	5	13.62	1.44×10^{-6}	1.43×10^{-6}	1.0
3	5	2	13.62	1.43×10^{-6}	1.43×10^{-6}	-0.1
5	2	3	13.62	1.61×10^{-6}	1.43×10^{-6}	12
5	3	2	13.62	1.62×10^{-6}	1.43×10^{-6}	13
3	4	4	14.15	1.30×10^{-6}	1.30×10^{-6}	-0.3
4	3	4	14.15	1.18×10^{-6}	1.30×10^{-6}	-0.3
0	4	5	14.15	1.15×10^{-6}	1.30×10^{-6}	-12
0	5	4	14.15	1.15×10^{-6}	1.30×10^{-6}	-12
4	0	5	14.15	1.31×10^{-6}	1.30×10^{-6}	0.9
4	5	0	14.15	1.23×10^{-6}	1.30×10^{-6}	-5.3
5	0	4	14.15	1.18×10^{-6}	1.30×10^{-6}	-9.5
5	4	0	14.15	1.21×10^{-6}	1.30×10^{-6}	-6.6
1	4	5	14.32	1.02×10^{-6}	1.26×10^{-6}	-19
1	5	4	14.32	1.24×10^{-6}	1.26×10^{-6}	-1.3
4	1	5	14.32	1.31×10^{-6}	1.26×10^{-6}	4.2
4	5	1	14.32	1.12×10^{-6}	1.26×10^{-6}	-11
5	1	4	14.32	1.24×10^{-6}	1.26×10^{-6}	-1.5
5	4	1	14.32	1.26×10^{-6}	1.26×10^{-6}	0.3
3	3	5	14.49	1.35×10^{-6}	1.23×10^{-6}	10
3	5	3	14.49	1.35×10^{-6}	1.23×10^{-6}	9.5
5	3	3	14.49	1.22×10^{-6}	1.23×10^{-6}	-0.5
2	4	5	14.83	1.09×10^{-6}	1.16×10^{-6}	-6.4
2	5	4	14.83	1.05×10^{-6}	1.16×10^{-6}	-9.6
4	2	5	14.83	1.28×10^{-6}	1.16×10^{-6}	11
4	5	2	14.83	1.04×10^{-6}	1.16×10^{-6}	-10
5	2	4	14.83	1.03×10^{-6}	1.16×10^{-6}	-11
5	4	2	14.83	1.18×10^{-6}	1.16×10^{-6}	1.6
4	4	4	15.31	1.17×10^{-6}	1.07×10^{-6}	9.7
0	5	5	15.63	1.05×10^{-6}	1.02×10^{-6}	3.4
3	4	5	15.63	1.02×10^{-6}	1.03×10^{-6}	-0.6
3	5	4	15.63	8.96×10^{-7}	1.03×10^{-6}	-13
4	3	5	15.63	1.11×10^{-6}	1.03×10^{-6}	8.2
4	5	3	15.63	9.79×10^{-7}	1.03×10^{-6}	-4.9

5	0	5	15.63	1.02×10^{-6}	1.02×10^{-6}	-0.1
5	3	4	15.63	9.26×10^{-7}	1.03×10^{-6}	-10
5	4	3	15.63	9.38×10^{-7}	1.03×10^{-6}	-8.9
5	5	0	15.63	1.23×10^{-6}	1.02×10^{-6}	21
1	5	5	15.78	9.42×10^{-7}	9.96×10^{-7}	-5.5
5	1	5	15.78	1.02×10^{-6}	9.96×10^{-7}	2.4
5	5	1	15.78	1.03×10^{-6}	9.96×10^{-7}	3.5
2	5	5	16.24	1.05×10^{-6}	9.38×10^{-7}	12.0
5	2	5	16.24	8.28×10^{-7}	9.38×10^{-7}	-12
5	5	2	16.24	9.15×10^{-7}	9.38×10^{-7}	-2.5
4	4	5	16.69	8.24×10^{-7}	8.77×10^{-7}	-6.0
4	5	4	16.69	1.00×10^{-6}	8.77×10^{-7}	15
5	4	4	16.69	9.10×10^{-7}	8.77×10^{-7}	3.8
3	5	5	16.98	8.09×10^{-7}	8.48×10^{-7}	-4.6
5	3	5	16.98	9.22×10^{-7}	8.48×10^{-7}	8.8
5	5	3	16.98	1.04×10^{-6}	8.48×10^{-7}	23
4	5	5	17.95	7.35×10^{-7}	7.40×10^{-7}	-0.6
5	4	5	17.95	7.54×10^{-7}	7.40×10^{-7}	1.9
5	5	4	17.95	6.73×10^{-7}	7.40×10^{-7}	-9.0
5	5	5	19.14	4.67×10^{-7}	6.35×10^{-7}	-27

Appendix E

DVH

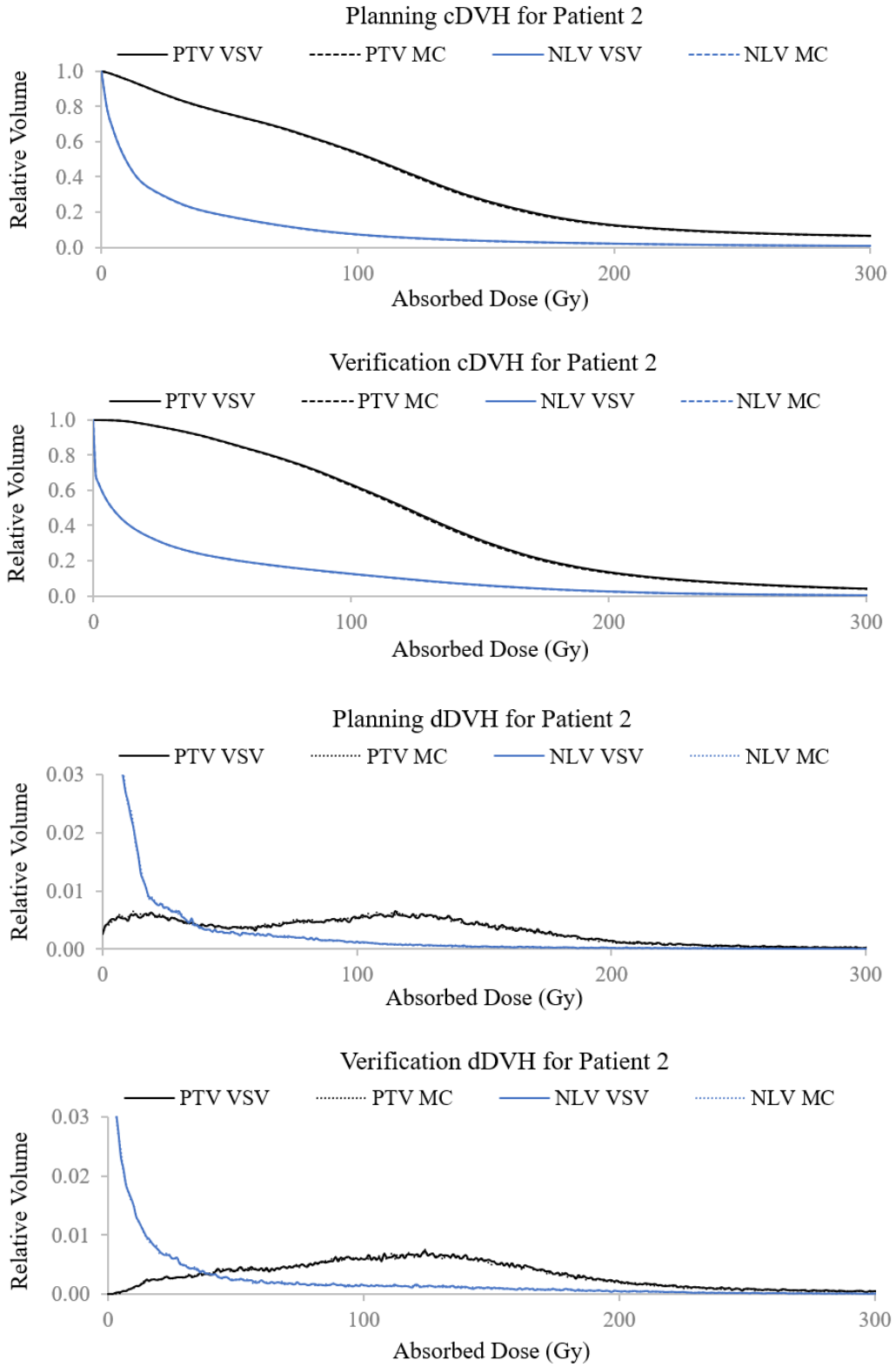

Figure E.1: Patient 2 cDVH and dDVH computed for planning and verification VSV- and MC-ADDs within the NLV and PTV.

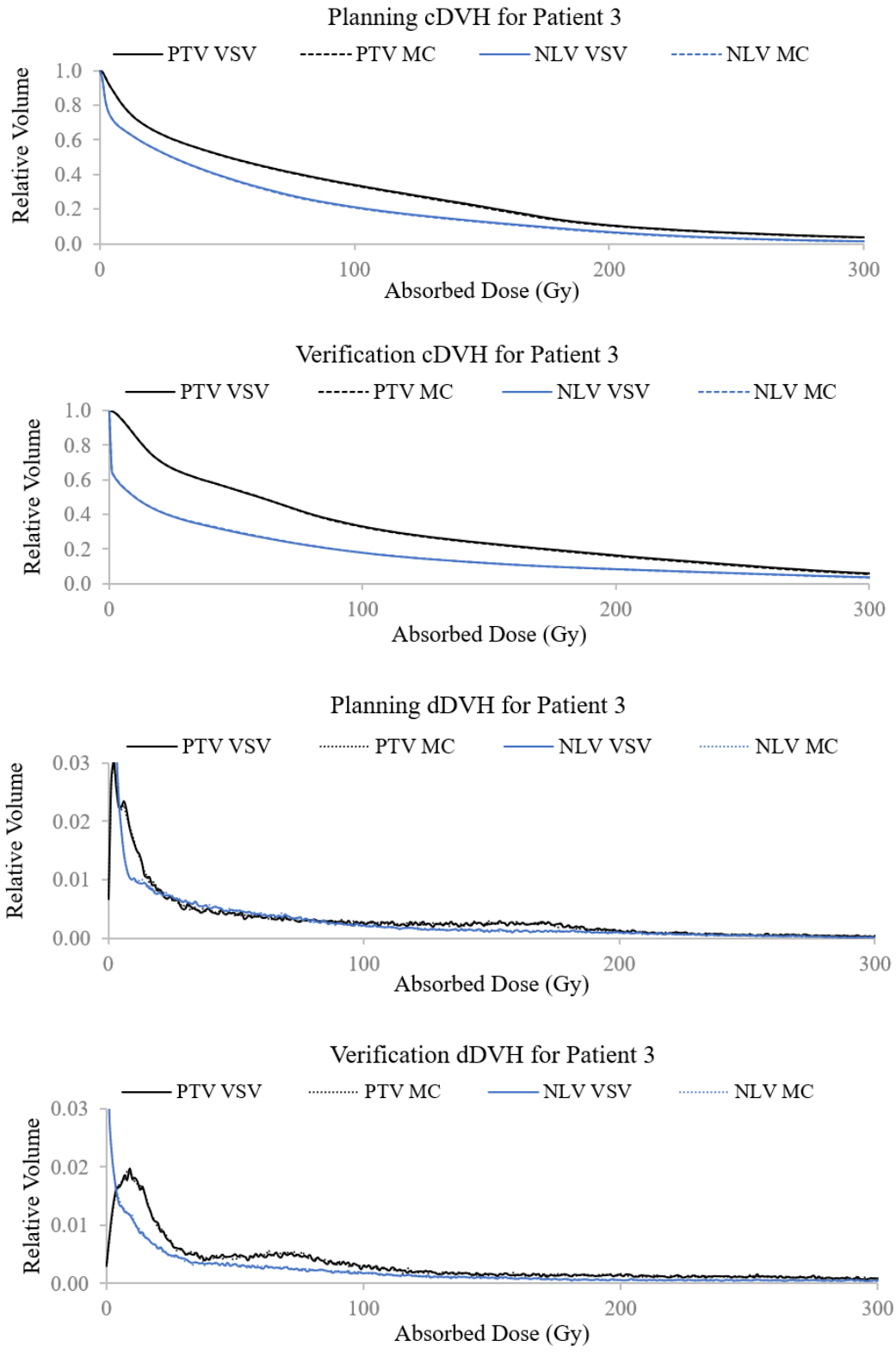

Figure E.2: Patient 3 cDVH and dDVH computed for planning and verification VSV- and MC-ADDs within the NLV and PTV.

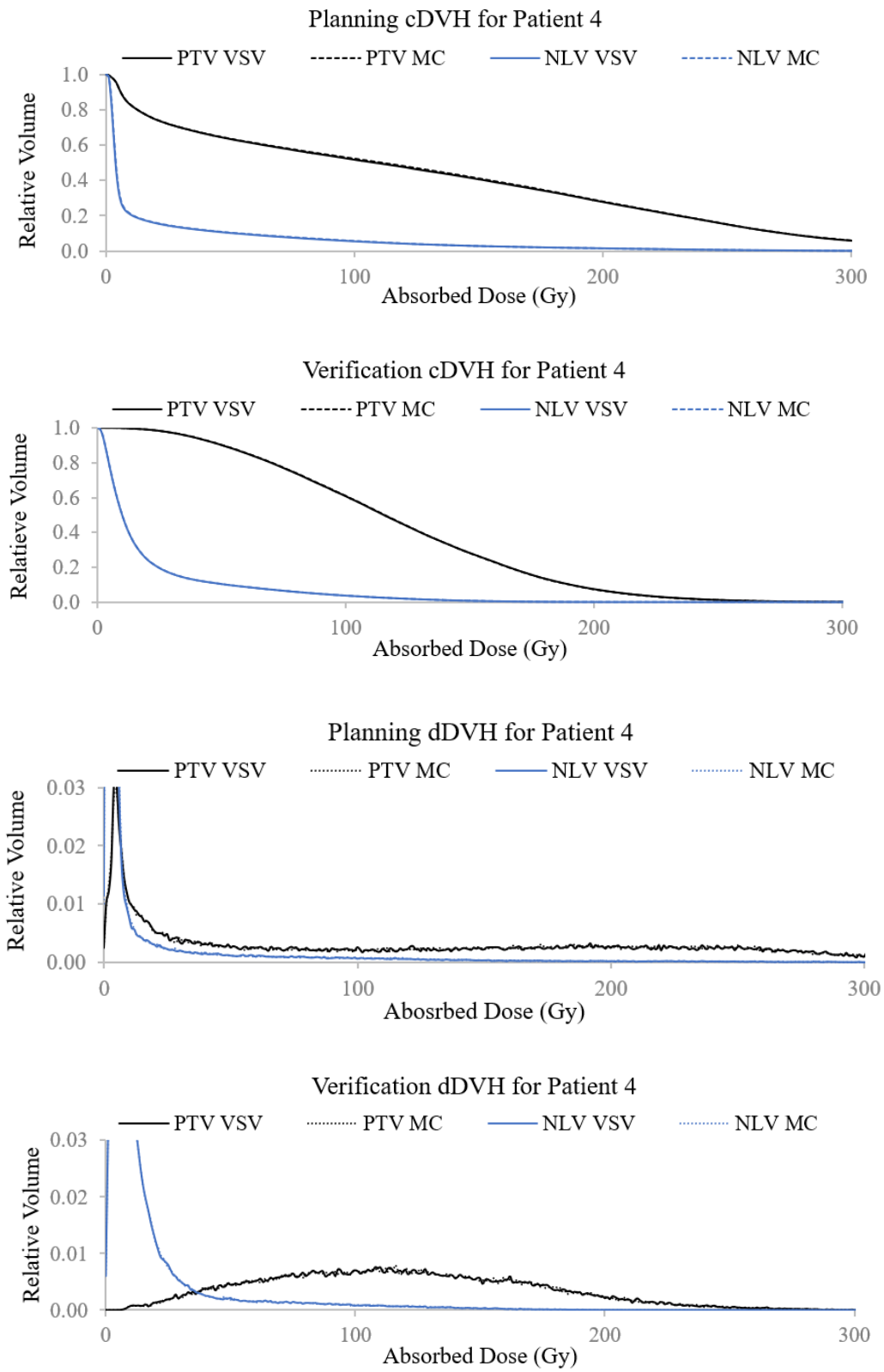

Figure E.3: Patient 4 cDVH and dDVH computed for planning and verification VSV- and MC-ADDs within the NLV and PTV.

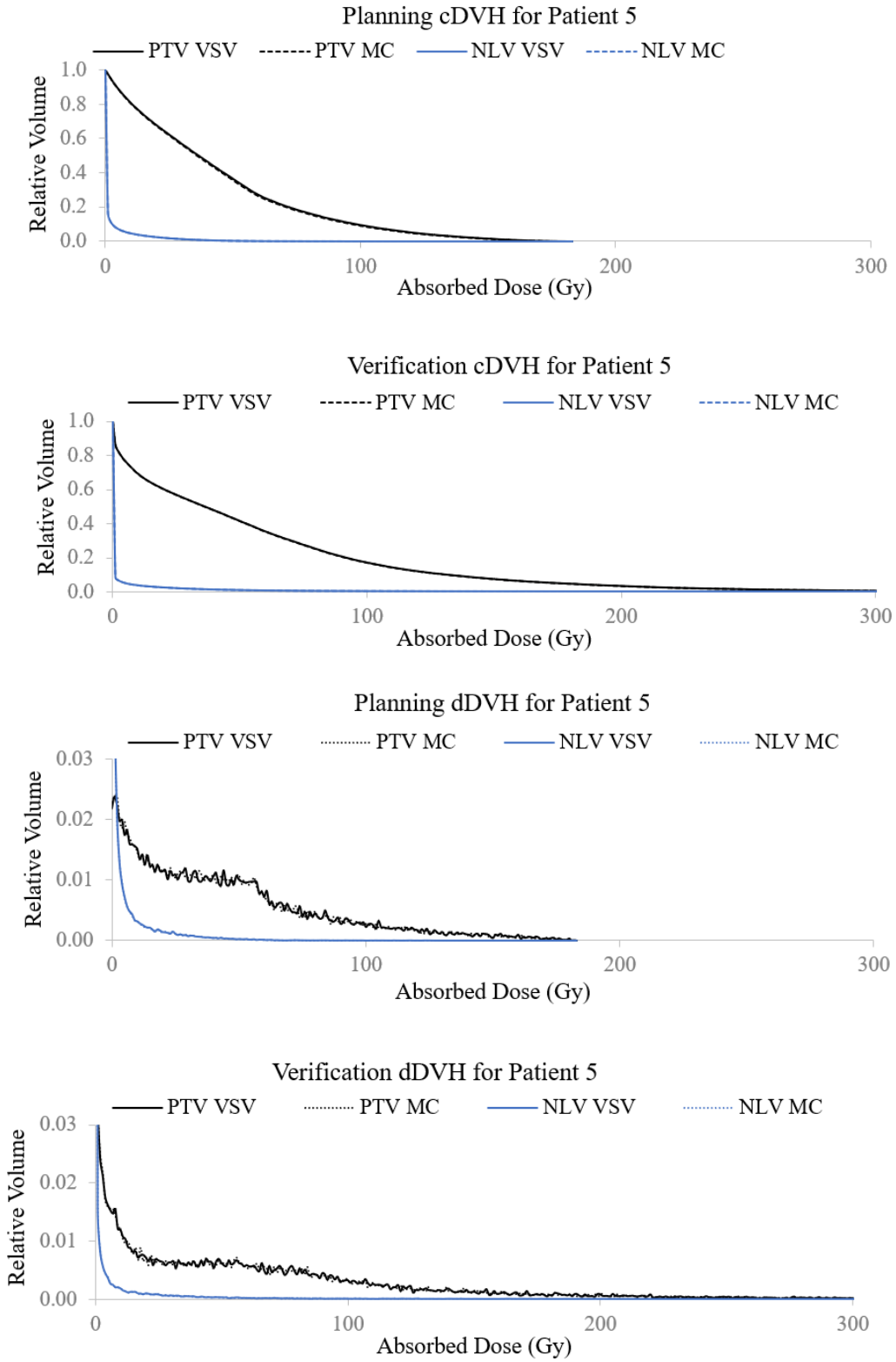

Figure E.4: Patient 5 cDVH and dDVH computed for planning and verification VSV- and MC-ADDs within the NLV and PTV.

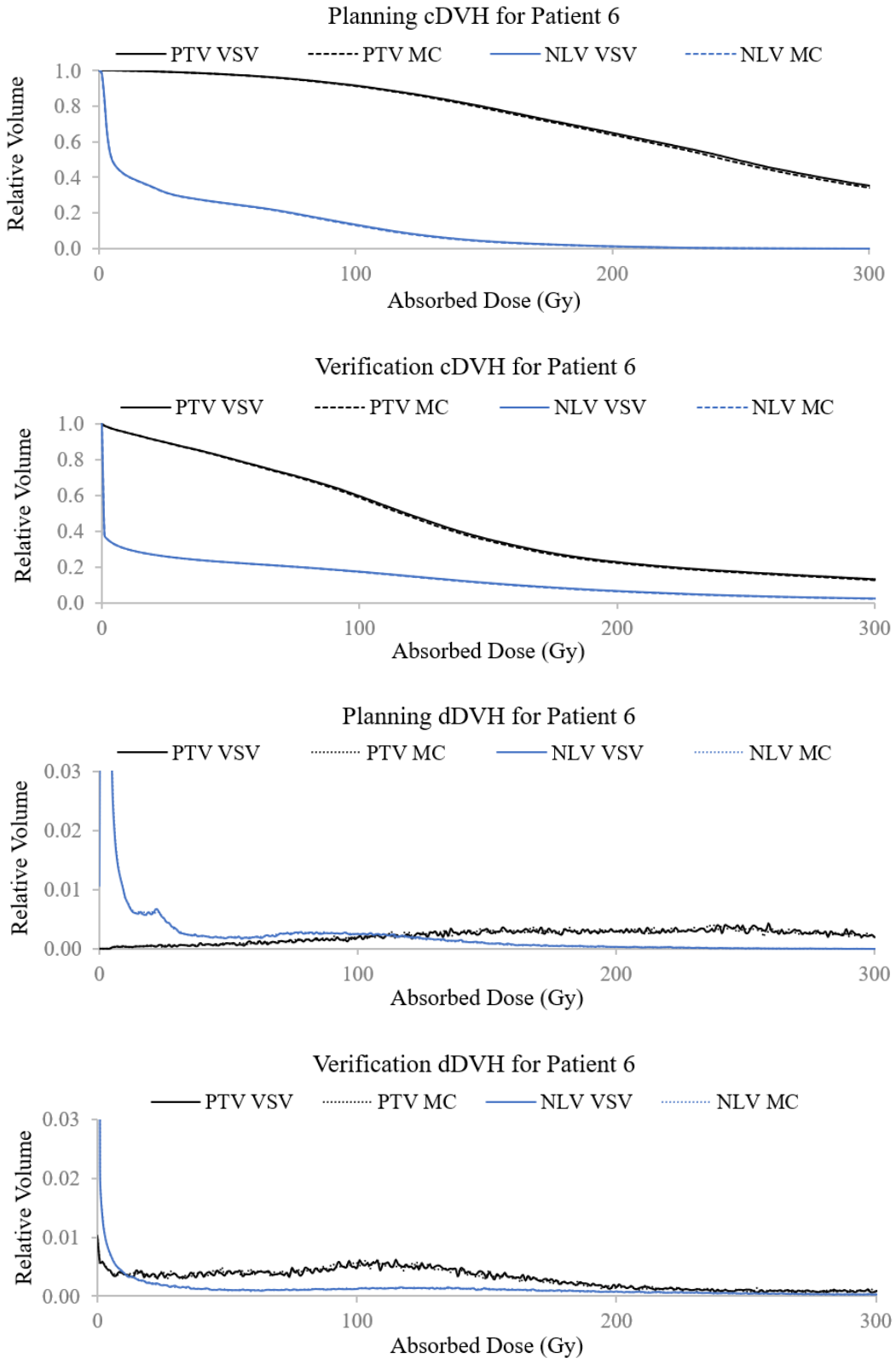

Figure E.5: Patient 6 cDVH and dDVH computed for planning and verification VSV- and MC-ADDs within the NLV and PTV.